The Dissertation Committee for Jisun Kim
certifies that this is the approved version of the following dissertation:

Study of Quantum Thin Films: Phase Relationship, Surface Reactivity, and Coherent Coupling

Committee:

Chih-Kang Shih, Supervisor

Alegandro de Lozanne

Maxim Tsoi

Gregory A Fiete

James R Chelikowsky

Study of Quantum Thin Films: Phase Relationship, Surface Reactivity, and Coherent Coupling

by

Jisun Kim, B.S.

DISSERTATION

Presented to the Faculty of the Graduate School of

The University of Texas at Austin

in Partial Fulfillment

of the Requirements

for the Degree of

DOCTOR OF PHILOSOPHY

THE UNIVERSITY OF TEXAS AT AUSTIN

August 2011

Dedicated to

my mom, dad, brother

and

the Heavenly Father.

Acknowledgments

I would like to acknowlege my parents, Myounggyoon Kim and Sunkey Pek, for all their love and support through all my life. You always have faith in me and encourage me no matter what. This faith and encouragement made me explore a new route fearlessly, and led me to graduate education away from my home country. Without you, I could not have finished this dissertation. I also want to express my deep love to my brother, Yonggu; we have shared our little childhood secrets together, grown up together, and now encourage each other to follow our own dreams. You will be always my "little brother" no matter how old we get, but also will be my life-long friend.

I would like to give my special thanks to my supervisor, Dr. Shih, with all respect for his advice and guidance through my Ph.D. journey. There was a time when I was struggling hard to figure out what I want or should do in order to move forward and eventually be an independent researcher. I was almost lost, but he kept pushing me forward with straightforward and constructive lessons until I found my way.

I want to express my deep love and appreciation to my dear friend Hae Ryung Chang for her love and prayer, which enlightened me so I could find the way out of the troubled, almost lost period in my Ph.D. journey. I also thank Jee Hyun and Youme, who have supported and encouraged me throughout. I

thank Soohyun for keeping in tight touch and always being there for me, even though we are so far apart that we could not see each other for several years. I want to express my love to all my friends, especially Seul, with whom I have shared many fun and happy moments together, and my bible study friends, especially Naika and Mieca, for great encouragement and support.

Special thanks to Dr. Alexander Khajetoorians and Dr. Shengyong Qin for all the help and training which have allowed me to develop essential skills and to achieve my research goals. Thanks to my labmate and good friend Charlotte Sanders for sharing those days at work with good laughter, even when it felt the work would never be finished. I appreciate the support and fellowship from all the other labmates with whom I spent most of the time during my graduate life: Chris Mann, Dr. Chendong Zhang, Dr. Jungdae Kim, Miri Choi, Hyoungdo Nam, Yuxuan Chen, Huan Li, John Robertson, and Amber Johnson.

I greatly appreciate all the time and energy my committee put into reviewing my dissertation. I also thank all my collaborators, especially Dr. Zhenyu Zhang and Dr. Wenguang Zhu.

To all the physics staff – especially to the whole machine shop, electronics shop, store room and cryo shop – I give my full respect, and my appreciation for their dedication to our work. I thank them for all the discussions regarding experimental designs and set-ups which have allowed me to proceed with my research more efficiently and effectively. I would like to express special thanks to Jack, Allan, and Annie.

Most of all, I am forevermore thankful to my heavenly father, my God who promised me the completion of my Ph.D. program, strengthened me to finish the dissertation, and finally let me achieve my doctorate. My love goes to You as Your love goes to me, always.

Jisun Kim

Study of Quantum Thin Films: Phase Relationship, Surface Reactivity, and Coherent Coupling

Publication No. _____

Jisun Kim, Ph.D.
The University of Texas at Austin, 2011

Supervisor: Chih-Kang Shih

When an electronic system is confined in one or more dimensions to a length scale comparable to the de Broglie wavelength, quantum confinement occurs. In metallic quantum thin films grown on semiconductor substrates, such confinement occurs between the vacuum-solid and the solid-solid interfaces, which results in the formation of distinctive quantum well states (QWS). Due to this confinement, many physical phenomena occurring in the thin metal system are totally different from the bulk system, which makes the study of quantum thin films interesting and important. In this thesis, quantum thin film studies, mainly based on the Pb/Si(111) system, were performed utilizing low-temperature scanning tunneling microscopy/spectroscopy (STM/STS) with a focus on three main aspects: phase relationship, surface reactivity, and coherent coupling. The Pb/Si(111) system is chosen due to its unique phase matching between the Fermi wavelength and the lattice spacing along [111], leading to a bi-layer quantum oscillation in many physical properties, including

the surface energy and the work function. Surprisingly, STM/STS measurement revealed that quantum oscillations of work function and surface energy have identical phase, in contrast to a theoretically predicted 1/4 wavelength phase shift in the phase relationship. Here, a new solution to this puzzle is provided. Furthermore, it is found out that the oxidation rate of Pb/Si(111) system is greatly enhanced in the presence of atomic scale catalyst – Cs substitutional atoms, while the reactivity to CO is saturated after the initial enhanced nucleation. Finally, by inserting thin Ag layers in between Pb/Si(111) system, the coherent coupling of double quantum wells (a Pb quantum well and a Ag quantum well) are probed, where combined QWS features are observed by STS measurement. The growth mechanism of these heterostructures – Pb/Ag/Si(111) – is also investigated.

Table of Contents

List of Tables

List of Figures

Chapter 1

Scanning Tunneling Microscopy: Theory and Setup

1.1 Introduction to scanning tunneling microscopy

The scanning tunneling microscope (STM), the first microscope that allowed atomic scale imaging, was invented by Binnig and Rohrer [1] in 1982 and implemented in the same year by Binnig, Rohrer, Gerber, and Weibel at IBM′s Zürich research laboratory [2, 3]. Since its invention, STM has been widely used in both industrial and fundamental research to understand and manipulate nano-scale phenomena and has become an indispensable tool in the field of surface science.

1.1.1 Tunneling theory – Bardeen approach

Through the intensive studies of metal-insulator-metal (MIM) tunneling junctions, several concepts and theoretical methods required to understand MIM tunneling were developed, many of which are instrumental in the understanding of the tunneling phenomena in STM. Among those theoretical methods, Bardeen's time-dependent perturbation approach is the most extensively used method [4]. In this approach, Bardeen considers two separate subsystems instead of trying to solve the Schrödinger equation of the coupled system as

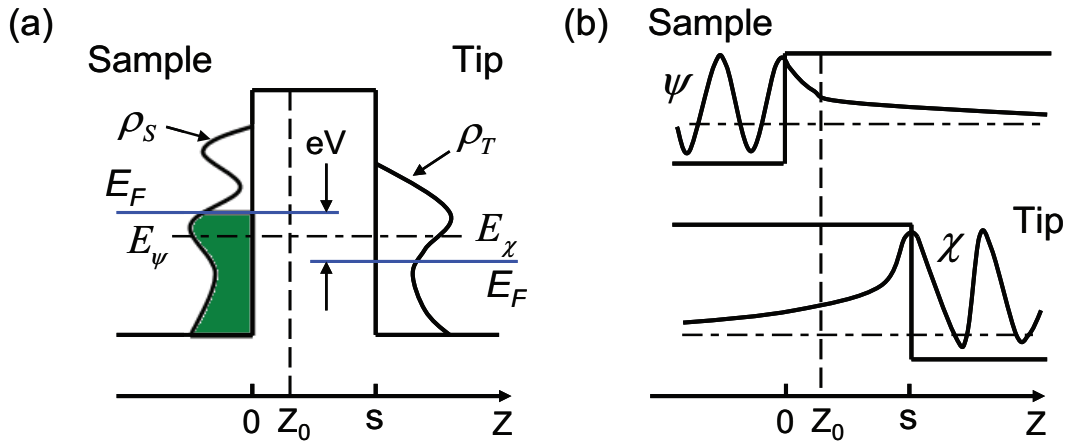

Figure 1.1: (a) The combined system where the tunneling current (I_t) flows with a bias V. $z = s$ is the barrier width. $\rho_S(E)$ and $\rho_T(E)$ are the density of states (DOS) of the sample and tip, respectively. An electron in the state ψ at energy E_ψ tunnels to a state χ with energy E_χ. (b) In the Bardeen approach to tunneling, the stationary Schrödinger equations are solved for two subsystems (tip and sample) separately, then I_t is calculated using Fermi′s golden rule.

shown in Fig. 1.1.

By solving the stationary Schrödinger equations, the electronic states of the separated subsystems (tip and sample) are obtained. The tunneling current is then calculated from the overlap of the wavefunctions of tip and sample using Fermi′s golden rule [5]. Bardeen showed that the tunneling matrix element, M, has the following form:

$$M = \frac{\hbar}{2m} \int_{z=z_0} (\chi^* \frac{\partial \psi}{\partial z} - \psi \frac{\partial \chi^*}{\partial z}) dS \tag{1.1}$$

where ψ and χ are the wavefunctions of the two electrodes. The probability, w, from Fermi′s golden rule, of an electron in the state ψ at energy E_ψ tunneling

to a state χ with energy E_χ, obeys the following equation:

$$w = \frac{2\pi}{\hbar} \mid M \mid^2 \delta(E_\psi - E_\chi) \tag{1.2}$$

The δ function in Equation 1.2 indicates that only states with the same energy level in both electrodes are able to tunnel into each other. The tunneling current (I_t) can then be evaluated by summing over all energy states in the system. Since the electrons in both subsystems follow the Fermi distribution at a finite temperature, I_t can be expressed in the following form,

$$I_t = \frac{4\pi e}{\hbar} \int_{-\infty}^{\infty} [f(E_F - eV + \epsilon) - f(E_F + \epsilon)] \times \rho_S(E_F - eV + \epsilon)\rho_T(E_F + \epsilon) \mid M \mid^2 d\epsilon \tag{1.3}$$

where the bias voltage is V, $f(E)$ is the Fermi distribution function, and $\rho_S(E)$ and $\rho_T(E)$ are the density of states (DOS) of the sample and tip, respectively. When $k_B T$ is small enough compared to the energy resolution required in the measurement, $f(E)$ can be approximated as a step function. Then the Equation 1.3 becomes much simpler,

$$I_t = \frac{4\pi e}{\hbar} \int_0^{eV} \rho_S(E_F - eV + \epsilon)\rho_T(E_F + \epsilon) \mid M \mid^2 d\epsilon \tag{1.4}$$

When a further assumption is applied that the magnitude of the matrix element $\mid M \mid$ does not change much in the considered energy interval, Equation 1.4 can be further reduced to the following form:

$$I_t \propto \int_0^{eV} \rho_S(E_F - eV + \epsilon)\rho_T(E_F + \epsilon)d\epsilon \tag{1.5}$$

where I_t is determined by the convolution of the DOS of the two subsystems. Equation 1.5 clearly states that the tunneling current is determined by the contributions from the DOS of the sample as well as of the tip. In order to obtain sample-sensitive DOS information, the tip′s DOS needs to be approximately constant, which can be achieved with a metallic STM tip. Then, from Equation 1.5,

$$\frac{dI}{dV} \propto \rho_S(E_F - eV) \tag{1.6}$$

where the changes in the tunneling current with respect to bias voltage is directly proportional to the sample′s density of states. Since the tunneling happens within a very small area under a STM tip, Equation 1.6 indicates that dI/dV spectra reveal the sample′s local density of states (LDOS) – this is the working principle of Scanning Tunneling Spectroscopy (STS), in which the electronic structure of sample can be investigated.

1.1.2 STM operation

In order to achieve atomic resolution, STM includes several components: a metallic tip which is mounted on a piezoelectric-controlled x,y, and z scanner; a coarse positioner which moves the STM tip toward a sample (or vice versa) faster than the piezo motion; a vibration isolation system; data

acquisition system; and typically Ultra High Vacuum (UHV) environments to maintain and prepare the surfaces of interest. Fig. 1.2 shows a schematic view of a STM. While a tunneling bias is applied to a sample, a sharp metallic tip is brought close to the sample by a piezoelectric motor in order to scan the surface. The STM tip is mechanically mounted on a piezoelectric tube scanner where the lateral scanning is achieved by applying high voltages on the outer tube, and the height movement is controlled by a feedback control (negative feedback loop) to keep the tunneling current constant by adjusting the sample-tip distance.

1.1.2.1 Constant current topography

In STM operation, constant current imaging is the most widely used mode. In this mode, the tunneling current is set to a specific value, "set point", and maintained by a negative feedback loop. Since the tunneling current is extremely sensitive to the sample-tip distance, any tiny change in the z direction can increase or decrease the tunneiling current significantly. During the scanning, if the tunneling current exceeds its set point due to the height modulation in the sample surface, the control unit adjusts the voltage applied in the z direction to move the tip backward. If the tunneling current is smaller than its set point, the opposite process occurs. Therefore, the tip follows an approximate surface morphology with a constant distance while the tunneling current maintains the constant value. The resultant image is closely related to the topography of the scanned surface.

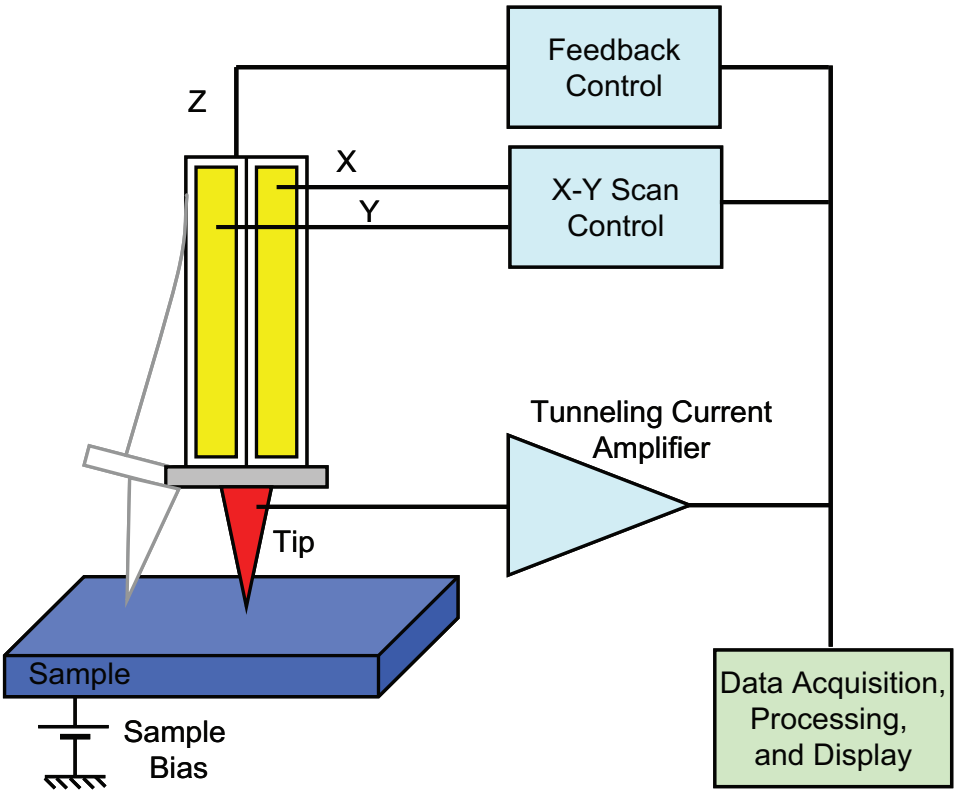

Figure 1.2: Schematic view of a STM. A metallic tip is mounted on the piezoelectric tube scanner which is controlled by a feedback control (Z) and a X-Y scan control. The tunneling bias is applied to a sample. The tunneling current is amplified and controlled by the data acquisition system where piezoelectric movements in x,y, and z directions are recorded and displayed as a 2D image.

1.1.2.2 $I - V$ tunneling spectroscopy

Another important mode of STM operation is the Scanning Tunneling Spectroscopy (STS). As shown in Equation 1.6, dI/dV spectra is directly related to the sample′s LDOS when a metallic tip is used. This dI/dV spectra can be obtained by taking $I - V$ tunneling spectroscopy at the point of interest on the surface. During the process, the tip is held stationary with the feedback

loop disabled. Then, the sample bias is changed with a small increment which results in a change in the tunneling current according to the sample′s LDOS at each sample bias. These changes are recorded and plotted as a function of the applied sample bias: an $I - V$ curve results.

Fig. 1.3 shows a schematic of the tunneling process between a sample and a tip. While positive biases are applied to the sample, electrons flow from the tip′s occupied states to the sample′s unoccupied states – "empty states" imaging of the sample (Fig. 1.3(a)), where the tunneling current is mainly determined by the sample′s DOS. As a result the electronic structure of the empty states of the sample is mapped. In negative biases, the opposite process occurs: electrons flow from the sample′s occupied states to the tip′s unoccupied states – "filled states" imaging of the sample (Fig. 1.3(b)). From this $I - V$ curve, dI/dV can be obtained by taking numerical derivatives or be directly acquired using a lock-in technique which will be discussed in the next section.

1.1.2.3 Differential conductance imaging

The LDOS of a sample can be investigated by STS at a specific point as discussed above. Using a lock-in amplifier, 2D mapping of the LDOS at a given sample bias can be achieved while a topographic image is recorded simultaneously. In this technique, a small AC modulation voltage, V_{mod}, with frequency ω is added to the DC sample bias V. Due to V_{mod}, the tunneling current also has an AC component which the lock-in amplifier detects and compares to V_{mod}. The output from the lock-in amplifier is, therefore, related

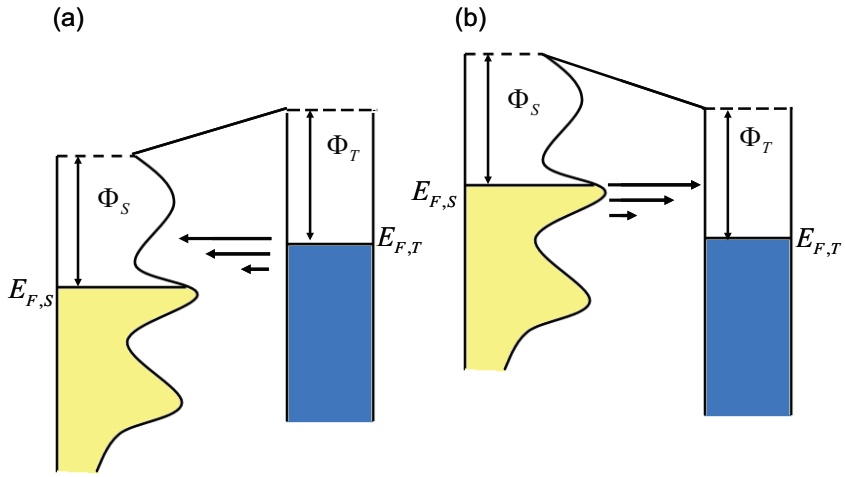

Figure 1.3: (a) When positive sample biases are applied, electrons move from the tip to the sample, which results in mapping of the empty states of the sample. (b) In negative sample biases, electrons move from the sample to the tip while imaging the sample′s filled states. Φ_S and Φ_T are the work functions of the sample and the tip, respectively.

to dI/dV:

$$I(V + V_{mod}cos(\omega t)) \approx I(V) + \frac{dI}{dV}V_{mod}cos(\omega t) + O[V_{mod}^2] \tag{1.7}$$

Since this technique is a phase-sensitive detection which can single out the component of the signal at a specific reference frequency and phase, dI/dV spectra measured by the lock-in techniques are less affected by surrounding noise sources: one can choose the modulation frequency ω to be away from noise frequencies and achieve a good noise to signal ratio even when external noise exists. For this reason, most dI/dV spectra are measured using a lock-in amplifier in the studies discussed in following chapters.

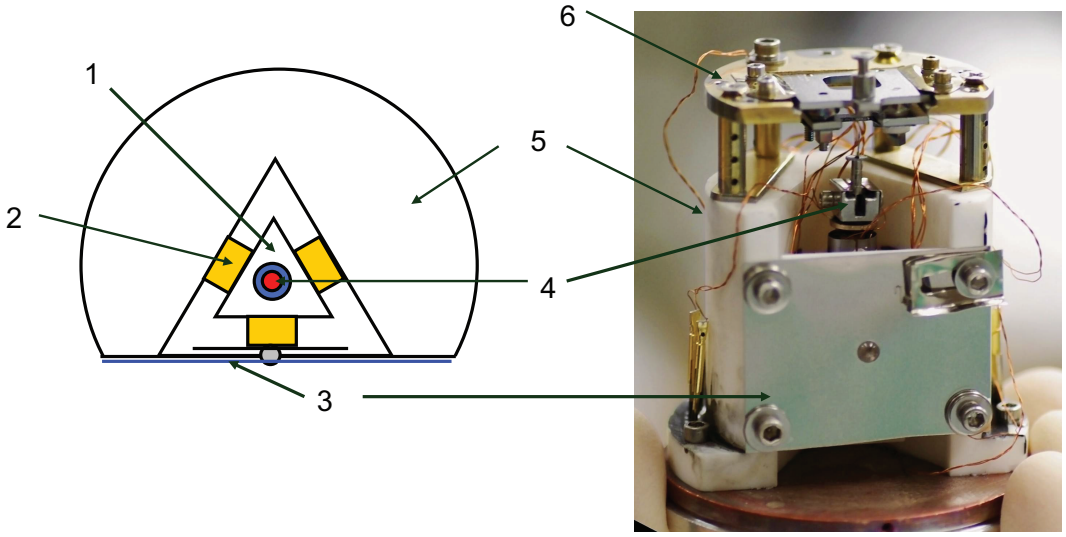

Figure 1.4: Pan-type head design: (1) sapphire prism, (2) shear piezo stacks, (3) spring plate holding the Macor plate by pressing a sapphire ball, (4) tip acceptor mounted on the scanning piezo tube, (5) Macor body, (6) sample stage.

1.2 Low-temperature STM (LT-STM) set-up

1.2.1 Pan-type walker

In order to achieve a good vibration isolation, a rigid STM body is required. Among various STM scanning head designs, the Pan-type head has been proved to be extremely rigid [6, 7] and is used in our LT-STM system.

Fig. 1.4 and Fig. 1.5 show the Pan-type walker′s design and working principles. In Fig. 1.4, a schematic and a real Pan-type STM head are shown. For the main body, Macor is used due to its high mechanical resonance frequency and good thermal matching to Molybdenum, which our sample holders and tip holders are made of. At the center of the Macor body, a sapphire prism

holding a scanning piezo tube and a tip, is pressed and fixed by 6 legs – each leg is made of 4 stacked sheer piezoelectric plates (EBL # 4). 4 of these legs are epoxied on the Macor body and 2 of them are epoxied on the separate Macor plate. This Macor plate is spring loaded: a sapphire ball is placed at the center hole of the Macor plate and a spring plate presses the sapphire ball to hold the Macor plate in position. On top of the Macor body, a sample stage is attached where a sample can be loaded and unloaded. A temperature sensor is mounted on this sample stage to monitor a sample temperature.

Coarse and fine z-motions are achieved by the following method. As shown in Fig. 1.5, at first, the sapphire prism is firmly held by 6 stacked piezo plates (Configuration a). Here, only 4 out of all 6 piezo legs are shown for simplicity. By applying a voltage V_0, a shear motion is created in the piezo leg 1 (Configuration b). Since the sapphire prism is still strongly held by other piezo legs (2-4), the prism can not move due to the friction. Then, consecutively, the same voltage V_0 is applied to leg 2 through leg 4. Still, the prism is in its original position. When all applied V_0 are ramped down simultaneously, all sheared piezo legs are recovered to their original stages, which results a finite movement of the sapphire prism (Configuration f). This finite movement is considered as one step. By repeating this process, a tip which is mounted on the sapphire prism can approach to the sample with great precision. In addition, when the piezo legs are not in motion, the tip is rigidly fixed in position due to the friction applied to the sapphire prism, which is extremely desirable for a stable tunneling current.

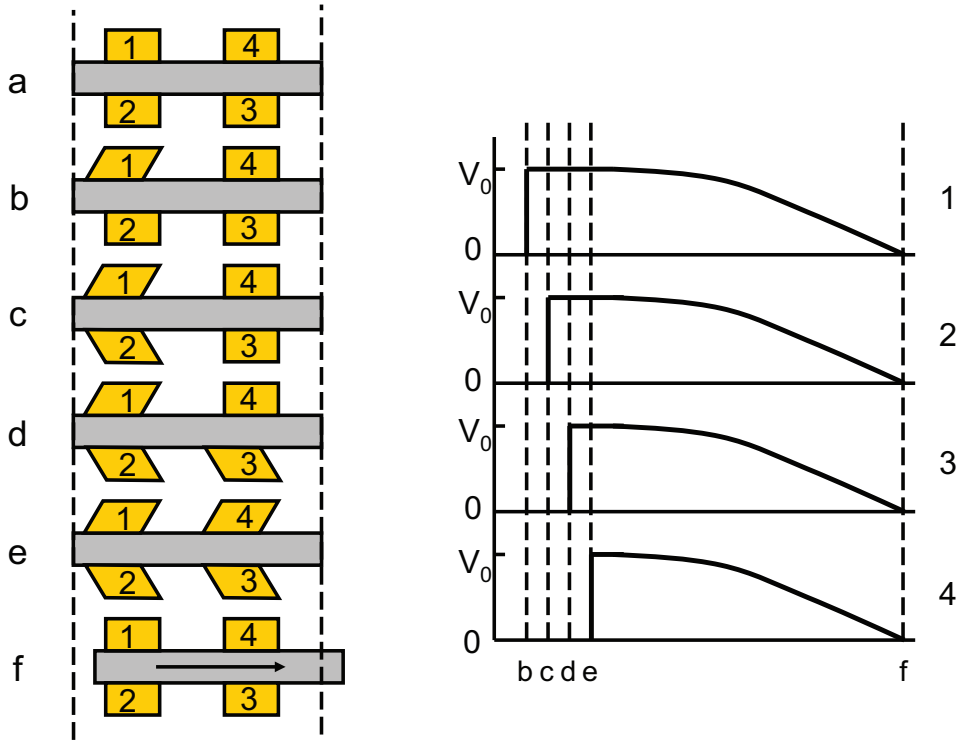

Figure 1.5: Schematic showing the working principles of the Pan-type walker. (Left) The sequential motion (a-f) of piezo legs, numbered 1 through 4. (Right) The voltage signal pattern corresponding to each motion of the piezo legs.

1.2.2 Chamber configuration

Fig. 1.6 shows the configuration of our LT-STM chamber. It has a load-lock system with a turbo pump and a gate valve for tip and sample loading and unloading (3). The transferred sample and the tip can be stored in the carousel, cleaned by direct heating (sample) or by e-beaming (tip), and Ag or Pb can be deposited from a thermal evaporator with a sample cooling capability in order to prepare a desired sample (4). Cs is evaporated from a getter source mounted on one of 2-3/4" flanges (2). Inside the chamber, tip

and sample manipulation is done using a manipulator (1) or a wobble stick (not shown). The pressure is kept lower than 1×10^{-10} torr most of the time by a 400 l/s capacity ion pump (8) aided by a Titanium Sublimation Pump (TSP) (7). The whole chamber sits on an air table (5) for vibration isolation. Four 12" by 12" LP-13 Shake Absorber Vibration Isolation Pads by Kellett enterprises, Inc. are placed under the air table for further vibration isolation (6). Our cryostat consists of a double-dewar design. The inner dewar – filled with liquid helium or liquid nitrogen according to the temperature requirement – has a 4 L capacity (10) and is surrounded by a 15 L capacity outer dewar filled with liquid nitrogen (9) in order to maximize the holding time of liquid helium when low temperature is necessary. The STM Pan-type head is mounted on a cylindrical shield made of oxygen free copper and is directly connected to the bottom of the inner dewar (11). In this way, the scanner stage can be effectively cooled down to 78 K (all with liquid nitrogen), or to 6.5 K (with liquid helium in the inner dewar).

1.2.3 Transfer chamber

Even though the LT-STM chamber is equipped with a thermal evaporator, it can only hold two metal sources with a small capacity. Therefore, a separate growth chamber is desirable for intensive growth studies with various materials. Recently, a new Molecular Beam Epitaxy (MBE) system was designed and built with three Knudsen cells and one e-beam evaporator, which greatly improved our growth capacity. However, this MBE system was not

designed to couple to our existing LT-STM chamber, so it requires a transfer mechanism to combine STM′s analysis power with the MBE system′s growth capability. In order to achieve in-situ sample transfer between isolated chambers, a transfer chamber is prepared (Fig. 1.7(a)). It consists of a small chamber with 8 ports (2), a transfer arm (1), a 60 l/s ion pump, and a gate valve (4). The vacuum is first prepared while it is attached to one of the existing chamber′s load lock system. During the transfer, the power to the ion pump is supplied by an Uninterruptible Power Supply (UPS) which allows long distance transferring without a power failure of the ion pump. It also has a specially designed rotatable sample stage, as shown in Figs. 1.7 (b-d). This rotatable sample stage is required due to the mirror symmetry between the LT-STM and MBE system: the sample can only be grabbed at + 90° relative to the inserting axis in LT-STM, but at - 90° in MBE system. In this design, the sample is loaded to the rotatable head of sample stage (Fig. 1.7(c)), which has a ball bearing epoxied at the bottom. Due to the ball bearing, the head of sample stage is guided to move along the track in the supporting part (Fig. 1.7(d)). Since there are three circular pits which are a bit deeper than the track, whenever the ball bearing sits on one of these pits, the head is preferentially fixed at those positions. This allows easy positioning and manipulating of the sample while it is transferred into the head. The transfer system is used for Ge capping of multi-layer heterostructures, which discussed in Chapter 6.4.

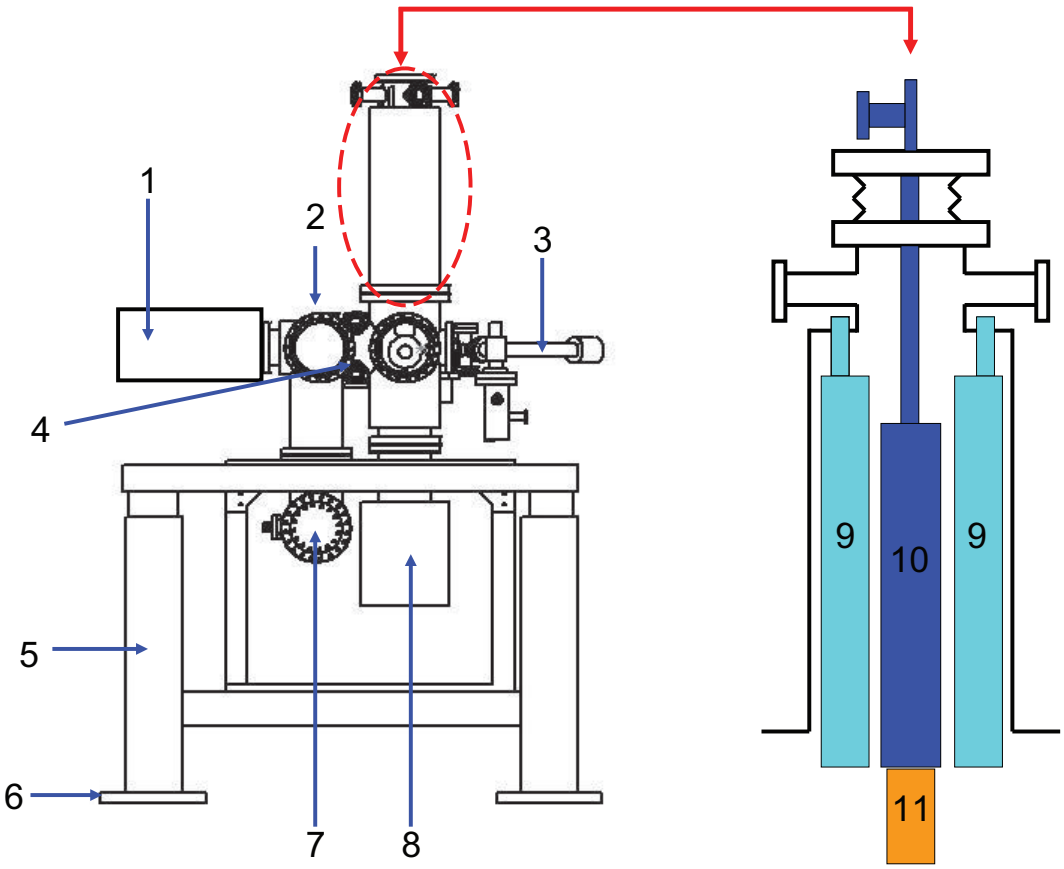

Figure 1.6: LT-STM chamber configuration: (1) manipulator, (2) Cs getter source, (3) load-lock system, (4) sample carousel, tip e-beaming stage, sample heating and growth stage, (5) air table, (6) vibration isolation pad, (7) Titanium Sublimation Pump (TSP), (8) ion pump, (9) liquid nitrogen outer dewar, (10) inner dewar for liquid helium or liquid nitrogen, (11) Pan-type STM head.

1.2.4 Tip preparation

In the studies which will be discussed in the following chapters, commercial Pt/Ir tips (Agilent Technologies, Inc.) are used. As shown in the SEM image (Fig. 1.8(a)), as-received Pt/Ir tips are not clean. In order to clean and

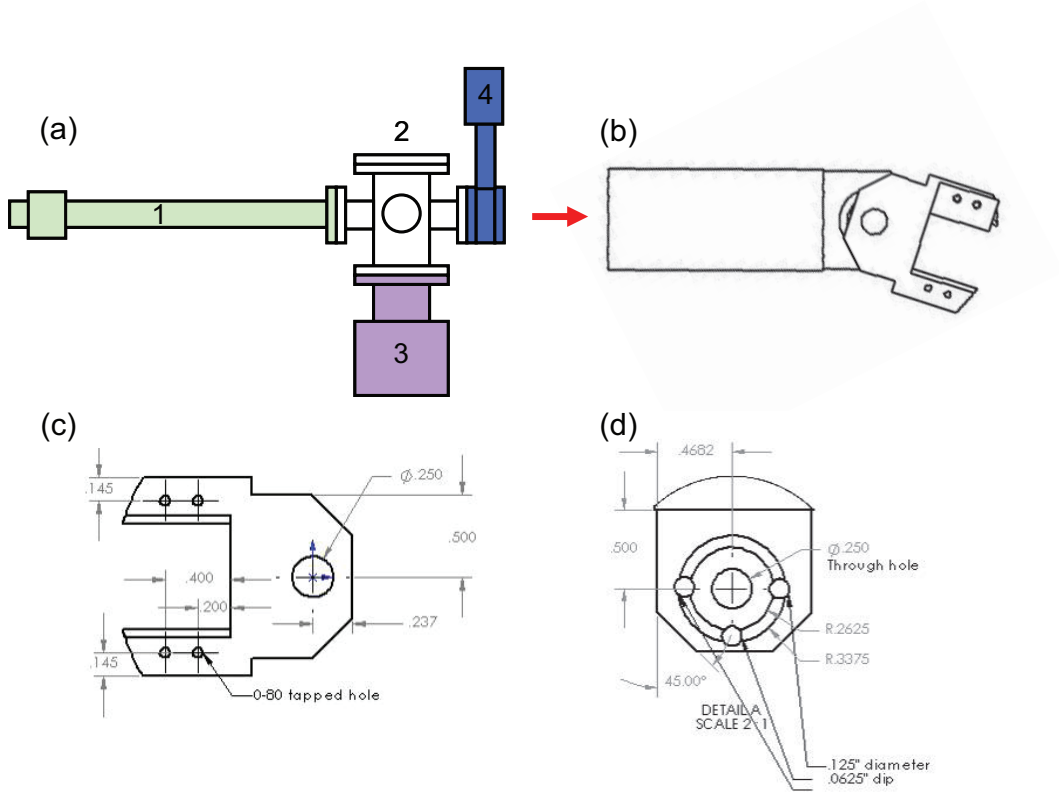

Figure 1.7: (a) Schematic of the transfer chamber: (1) transfer arm, (2) main chamber – sample storage, (3) ion pump, (4) gate value. (b) Assembly of rotatable sample stage. (c) Rotatable head of the sample stage. (d) Supporting part with a track and three stationary positions.

sharpen these tips, Focused Ion Beam (FIB) is used: removing materials from the tip surface by ion bombardment. The resultant tip shows a cleaner and sharper surface (Fig. 1.8(b)).

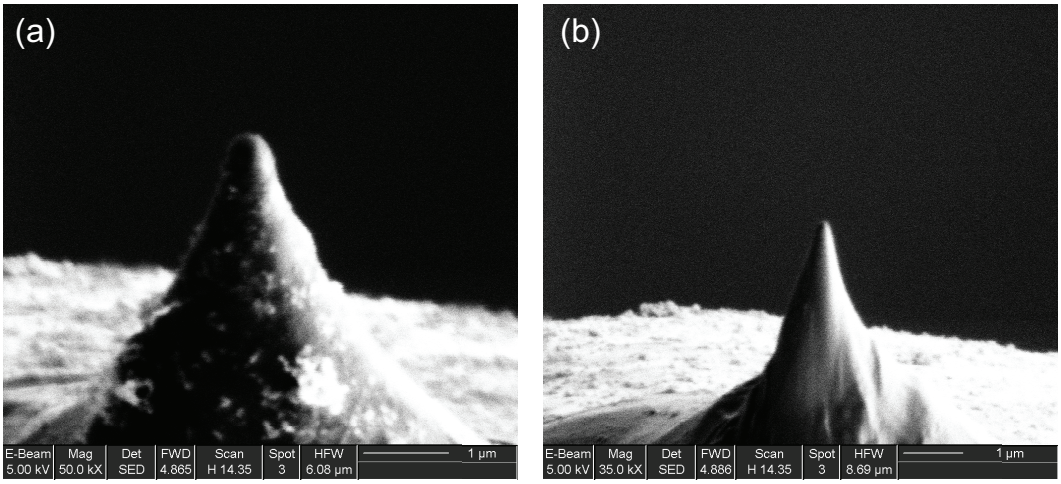

Figure 1.8: FIB tip cleaning: (a) before, (b) after the FIB cleaning. 100 pA is typically used for the FIB ion current during cleaning.

Chapter 2

Quantum Thin Film Growth

2.1 Introduction – quantum size effect (QSE) on thin metal films

When an electronic system is confined in one or more dimensions to a length scale comparable to the de Broglie length, quantum confinement occurs. Such confinements have played a central role in artificially engineered electronic systems such as quantum wells, quantum wires, quantum dots, and related structures. For semiconductors, quantum confinements occur at a length scale somewhere between 10 and 100 nm. For metals, however, they occur at a length scale about one to two orders of magnitude smaller (around 1-5 nm). In order to investigate the quantum size effect in metals, it is required to use epitaxially grown metallic thin films with thickness ranging from 2-25 monolayers (ML). Due to advancements in atomic scale control in epitaxial growth of metallic thin films, it is possible to access this strongly confined regime. In these metallic thin films grown on a semiconductor surface, the conductance electrons are confined in the z-direction perpendicular to the film surface by the vacuum on one side and the metal-semiconductor interface on the other. Meanwhile the energy dispersion in the xy-direction remains nearly parabolic – free electron like – for s-p metals. This confinement in the z-direction results

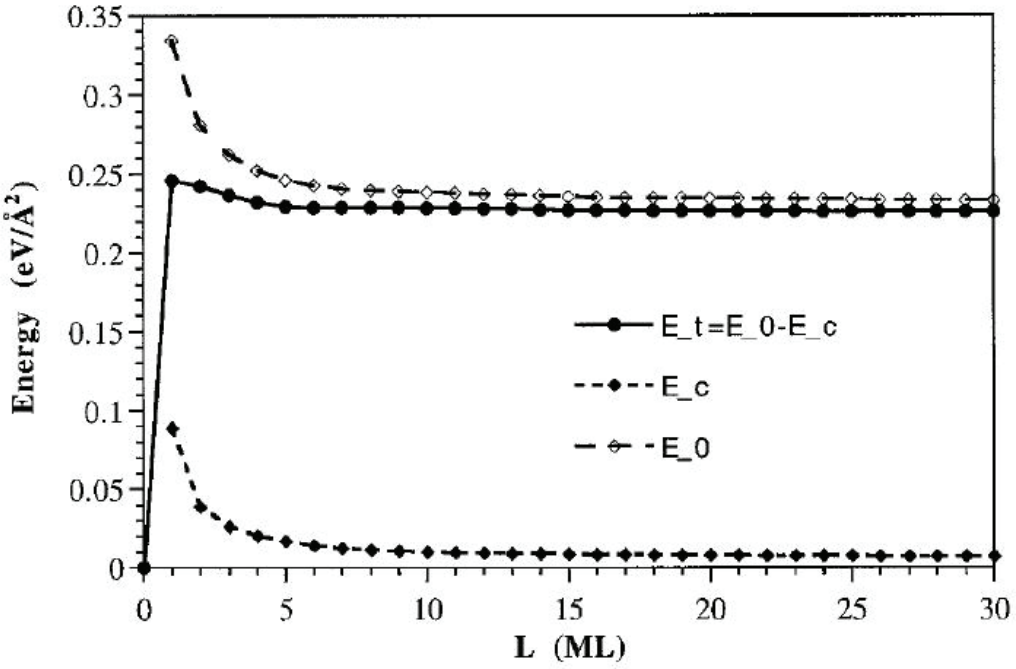

Figure 2.1: Total energy of the system (E_t) as a function of film thickness (L) for Ag on GaAs(110) [8]. The dip at L = 5 ML defines the "critical thickness" in this film [9].)

in discrete energy levels known as quantum well states (QWS).

It was predicted by Feibelman that quantum confinement can cause an oscillation in a metal′s surface energy and affect the growth of metal films for a freestanding metal system in 1983 [10]. In 1998, a new growth model was proposed for metal thin films that considered a supporting semiconductor substrate – so called "electronic growth" or "quantum growth" phenomena [9]. The theory was inspired by the discovery of an unusual growth mode exhibited in Ag films grown on GaAs(110) [8]. In this "electronic growth" model,

three central ingredients are considered to influence the thermodynamic stability of epitaxial thin films: (a) Quantum confinement: a stabilizing factor by mediating a repulsive force between metal-semiconductor interface, (b) charge spilling: a destabilizing factor due to an attractive force between two interfaces caused by electron transfer, and (c) interface-induced Friedel oscillations: an oscillatory modulation factor of (a) and (b). The resultant calculation of the total energy (E_t) based on these three factors, as shown in Fig. 2.1, successfully explains the existence of "critical thickness" – the thickness where the stability of the film changes from stable to unstable (or the other way around) – which was first observed experimentally in Ag films on GaAs(110) [8].

When this model is applied to other metal-semiconductor substrate systems, it is revealed that, depending on the metal type, different growth behavior is expected, categorized as types A through D (Fig. 2.2). Type A (Au, Cu) exhibits a "critical thickness" around 5 ML which is similar to Ag. However, type B (alkali metals) shows no dip in E_t which explains the experimental fact that a flat film of alkali metals thicker than 1 ML cannot be grown. Type C (Be, Mg) exhibit a new feature – a "magic thickness" where the film is only stable among adjacent thicknesses – as well as a "critical thickness." Type D (Al, Pb) shows an oscillatory behavior in E_t. These calculations clearly demonstrate that the QSE is closely linked to the growth behavior of metal thin films and should be considered when the thin film growth is investigated as well as the interplay with the substrate.

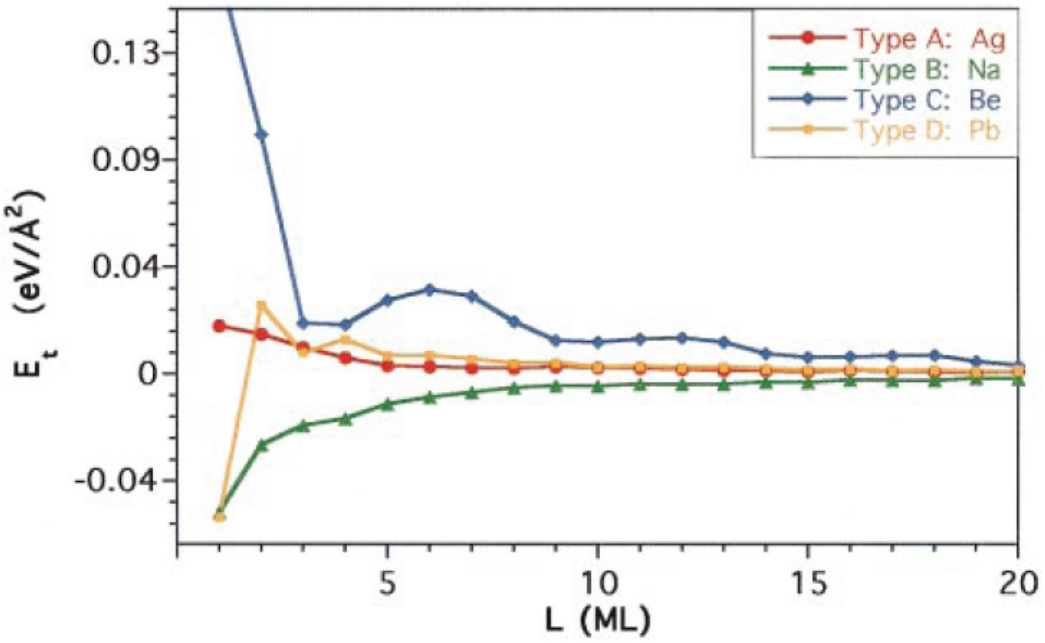

Figure 2.2: Film stability for different metals grown on GaAs(110) for four representative types. For comparison, an element-specific constant term is subtracted from each curve to make the E_t equal to zero when L increases [9].

2.2 Pb/Si(111) system

Among various thin metal on semiconductor systems, Pb on Si(111) has been the most intensively investigated one. This is due to the nearly half-integer phase matching between the Fermi wavelength ($\lambda_F = 3.98$Å) and the lattice spacing along [111] (d = 2.86 Å), $1.5\lambda_F \approx 2d$. When thin Pb films are grown on Si(111) substrate, electrons are confined in the z-direction and $k_\perp(E)$ is determined by the Bohr-Sommerfeld quantization rule,

$$2k_{\perp}(E)Nd + \Phi_v + \Phi_i = 2n\pi \tag{2.1}$$

where N is the number of layers (ML), d is the interlayer spacing, Φ_v is the phase shift of the electron wave function at the vacuum-metal interface, Φ_i is the phase shift at the metal-semiconductor interface, and n is an integer number. Due to this unique half-integer matching, a bi-layer oscillation of the QWS in the Pb films occurs as expected from Equation 2.1. The oscillation of QWS causes the density of states (DOS) at the Fermi level to change accordingly and this alteration of DOS further induces a bi-layer oscillation in physical properties of Pb films which are observed in the thickness relaxations [12], chemisorption behavior [13], superconducting transition temperature [14–16], surface energy [17], and work function [18, 19]. Among these various properties, the relationship between the surface energy and the work function is one of the special topics which will be thoroughly discussed in Chapter 3. Here, only one calculated surface energy is briefly mentioned to explain the origin of two growth modes of Pb films. Fig. 2.3 illustrates the oscillatory nature of the calculated surface energy as a function of thickness and corresponding QWS of each layer. The thicknesses showing local minima in the surface energy are energetically more favorable and considered as "quantum stable" thicknesses. Similarly, the thicknesses showing local maxima in the surface energy correspond to "quantum unstable" thicknesses. This oscillating film stability plays a very important role in the growth modes of Pb films on Si(111).

2.2.1 Two growth modes of Pb films on Si(111)

The growth of Pb films on Si(111) substrate is governed by thermodynamics, kinetics and QSE of the system. Therefore, the final configuration of the system is determined by the growth path which can alter each contribution from these three key factors. In addition, "electronic growth" model [9] indicates the charge transfer at metal-semiconductor interface affects the resulting film′s magic/critical thickness. This suggests the interface also can play an important role in the quantum thin film growth. In following sections, two distinctive growth modes of Pb films, consequences of the competition of all key factors, are discussed.

2.2.1.1 Globally flat film growth

When Pb is deposited at low temperature ($\sim$ 100 K) and annealed to room temperature (two-step method), an atomically flat, epitaxial Pb film, also know as a "globally flat film" can be grown on Si(111)-7$\times$7 surface. This type of growth mode is first observed in Ag on GaAs(110) system [8] and it has been applied to several metal-semiconductor system to form globally flat films such as Al, Ag, and Pb on various substrates [20–23]. Due to the low mobility of Pb adatoms deposited on the Si substrate, Pb adatoms nucleate on the landing sites and form small clusters rather than diffuse the surface to attach an existing island and grow. These nucleated and clustered Pb atoms then slowly gain a kinetic energy to form epitaxial films during the slow annealing process. Since Pb atoms cover the Si surface uniformly, it is energetically not

favorable to create relatively huge steps in order to form 3D islands. Rather, the system keeps its uniformity and develops epitaxial films with a uniform thickness over large areas following the underlying Si morphology. Figs. 2.4(b) and (c) show the STM image and the schematics representation of such a system.

While surface diffusion and nucleation decide the final morphology of the films, QSE still plays an important role. As discussed in Chapter 2.2, the conduction electrons in thin Pb films are confined in the growth direction resulting in QWS formation, which can be measured by STS. Fig. 2.4(d) shows clear QWS peaks in dI/dV spectra taken on a 13 ML film. Due to the bi-layer oscillation in the surface energy caused by QWS oscillation, every other layer is a stable thickness. Therefore, the globally flat Pb films consist of one of the stable thicknesses since it is energetically favorable. When the Pb coverage is not enough to complete the stable thickness (N-layer), it forms 2 ML holes (islands) on the films instead of 1 ML holes (islands) since N-2 (N+2) layer is the next stable thickness. This is the reason why the observed 13 ML films in Fig. 2.4(b) have a 2 ML deep hole (11 ML).

Interface effect

Different interfaces can affect the film growth. Due to the strain existing at Pb and Si(111)-7×7 surface interface, it is not possible to grow thin Pb films below 5 ML [22] on this interface. In order to access thinner films, an alternative interface is required and recently, 2 ML Pb films were successfully grown on the mixture of $\sqrt{3} \times \sqrt{3}$ and $\sqrt{7} \times \sqrt{3}$ surfaces [16]. The stripe

incommensurate (SIC) phase [24, 25] mixed with a $\sqrt{7} \times \sqrt{3}$ phase [26] can be prepared with about 1 ML Pb deposition at room temperature (RT) followed by annealing up to 400°C for 4 min. (Fig. 2.5(a)). The stripe incommensurate Pb surface consists of domains (bright area) which are $\sqrt{3} \times \sqrt{3}$ structure and domain walls (dark area) while the $\sqrt{7} \times \sqrt{3}$ phase exhibits combined bright and dark row-like structures (right-bottom area in Fig. 2.5). With this new interface thin Pb films can be prepared. Fig. 2.5(b) is a topographic STM image of such films. It is made of 4 ML globally uniform films with 1 ML high islands. Note that 4 ML and 5 ML lie in the cross-over regime where two consecutive thicknesses can be stable. This is a result of the accumulated phase mismatch since the half-integer phase matching is not perfect ($1.5\lambda_F \approx 2d$) and for every 9 ML, the accumulated difference causes a phase-slip (cross-over) in the bi-layer oscillation. This is why 1 ML height difference is allowed on 4 ML flat films, which is not possible in the case of 13 ML films, shown in Fig. 2.4(b). By changing an interface structure, therefore, a wide range of film thicknesses can be accessed and the interplay between the QSE, thermodynamics, and kinetics of the system can be investigated.

2.2.1.2 Flat top mesa growth

When Pb is deposited at room temperature (RT) on Si(111)-7×7 surface, it forms first a wetting layer and then 3D islands with flat-top which span over several terraces of Si substrate. Fig. 2.6(a) shows a typical STM image of the mesa formed after 3.25 ML of Pb deposition at RT. Si steps are still visible

even after being covered with a rough wetting layer while the mesa shows a smooth flat-top. Schematic representation of this structure is shown in Fig. 2.6(b). Compared to the globally flat film growth, Pb adatoms are quite mobile at RT [27] so they can diffuse across the surface and make large 3D islands. Even though the QSE is still present and the oscillation of the surface energy exists accordingly, it is now energetically unfavorable to form only quantum stable thicknesses since it requires a step formation in every other layer, which costs large step energy. Therefore, RT growth prefers flat-top geometry and as a result, a quite interesting structure which includes quantum stable and also unstable thicknesses is formed. This is a very unique characteristic of the Pb/Si(111) system which allows access to both stable and unstable thicknesses at the same time and provides a perfect platform to investigate how the oscillatory nature of DOS caused by quantum confinement affects the physical properties of the system.

2.2.2 Imaging buried Si(111)-7×7

When conduction electrons are confined in thin metal films by a vacuum and substrate interfaces, they contain the information of these interfaces as shown in Equation 2.1. Even though STM is a surface sensitive technique, it can probe electronic properties of the sample as explained Chapter 1.1.2.2. Therefore, the quantized conduction electrons can be used as a probe to investigate buried interfaces by STM. However, the lateral resolution of the buried interfaces is limited by scattering. When a feature of lateral size σ at the

interface is detected by a quantized electron in the z direction (perpendicular to the surface), the angular divergence is proportional to $\alpha(\lambda/\sigma)$ due to the Heisenberg uncertainty principle. Here, α is the ratio of electron′s effective mass in the z-direction to the xy-direction, $m_\perp/m_\parallel$ and λ is the de Broglie wavelength of the electron. Thus, when the feature of size σ is imaged at the vacuum side with STM tip, it is imaged with a size of $\sigma + L\alpha(\lambda/\sigma)$, where L is the thickness of the films. Therefore, the best lateral resolution is around $\sigma \sim \sqrt{\alpha L\lambda}$. If a free electron gas is considered, only the film thickness with the same order of magnitude of the λ_F, the Fermi wavelength, can resolve the interface structure.

In the case of Pb films grown on Si(111), surprisingly, it was demonstrated that the Si(111) 7×7 interface buried as deep as 100 Å can be imaged, which is well beyond the scale of its Fermi wavelength, $\lambda_F = 3.98$ Å [28]. Fig. 2.7 shows a series of STM images taken on the 13 ML Pb films shown in Fig. 2.4(b). Clearly, the fringe patterns in Fig. 2.7 are caused by electronic interference, rather than the surface morphology of the Pb films, since they change their contrast (Figs. 2.7(c),(e),(f)) and can be totally washed out at different sample biases (Figs. 2.7(b),(d)). These images exhibit the underlying Si(111)-7×7 interface at different sample biases. As shown in Fig. 2.8, the border lines and vertices with dark/bright contrast on Pb films originate from the underlying Si(111)-7×7, corner holes, and dimer chains. This enhanced lateral resolution is accounted for by a large anisotropy in the electron′s effective mass in the z-direction relative to the xy-direction – $\alpha(m_\perp/m_\parallel) \ll 1$.

All of the characteristics discussed in this chapter make the Pb/Si(111) system a favorable template to investigate quantum phenomena and its interplay with classical properties; thus, the main studies in the following chapters are based on this system.

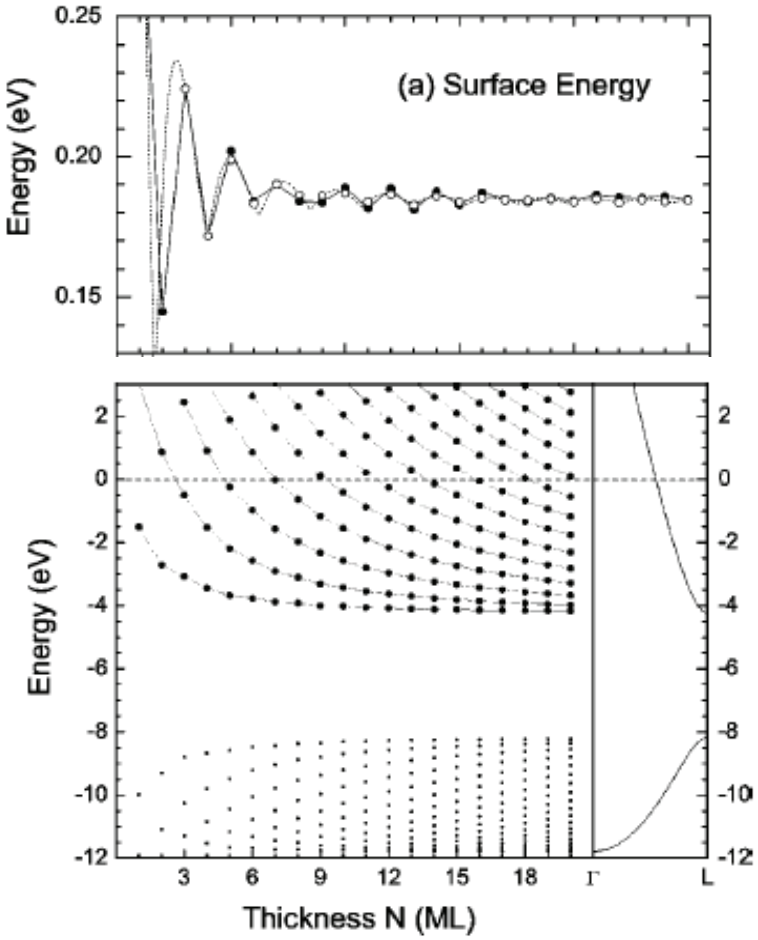

Figure 2.3: Calculated surface energy per 1×1 unit cell (top) and QWS energies at $\overline{\Gamma}$ in Pb (111) thin films as a function of thickness relative to the Fermi level (bottom)[11].

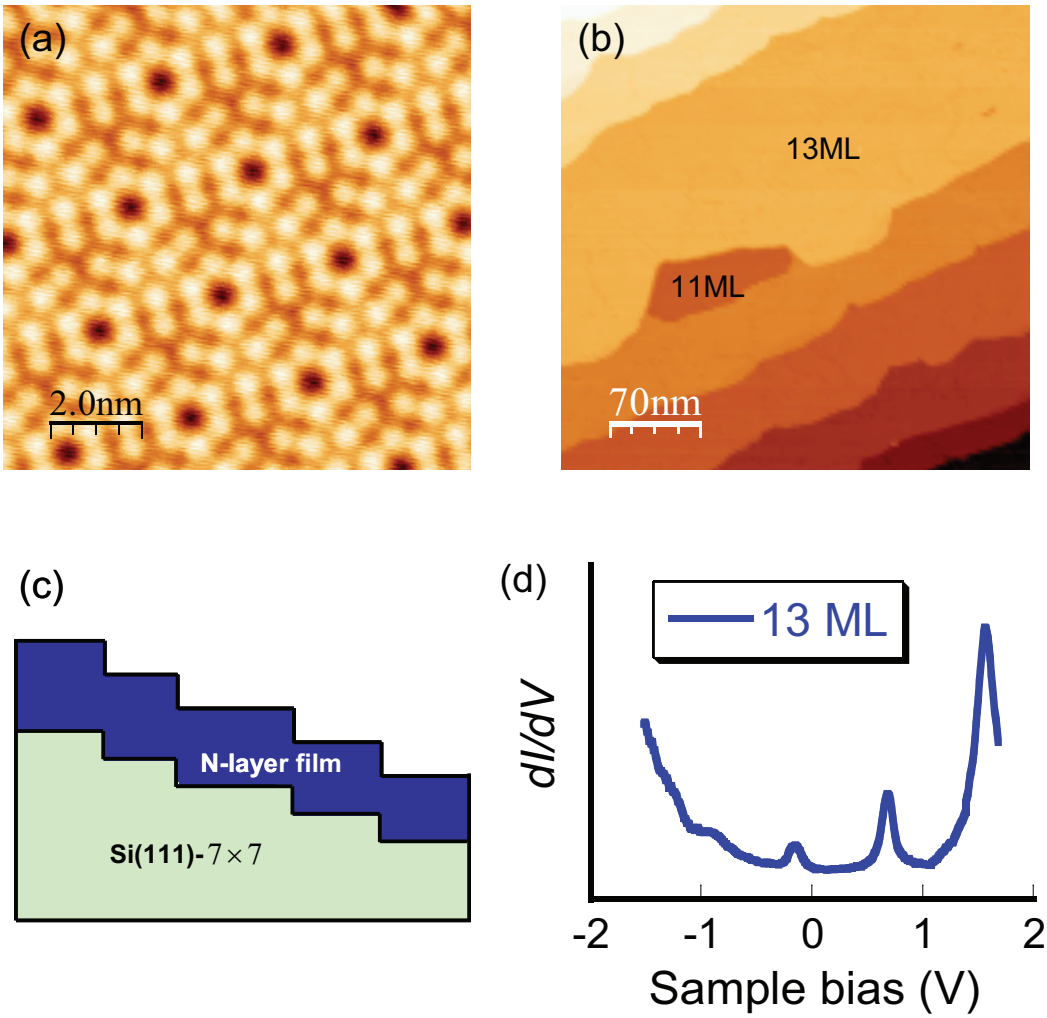

Figure 2.4: Globally flat Pb films grown on Si(111)-7×7 surface. (a) Initial Si(111)-7×7 surface. (b) Resultant Pb films (13 ML) grown by two step method. Note the area showing a 2 ML deep hole (11 ML). (c) Schematic diagram of this system. (d)dI/dV spectra taken on 13 ML Pb films. Distinctive QWS are clearly observed.

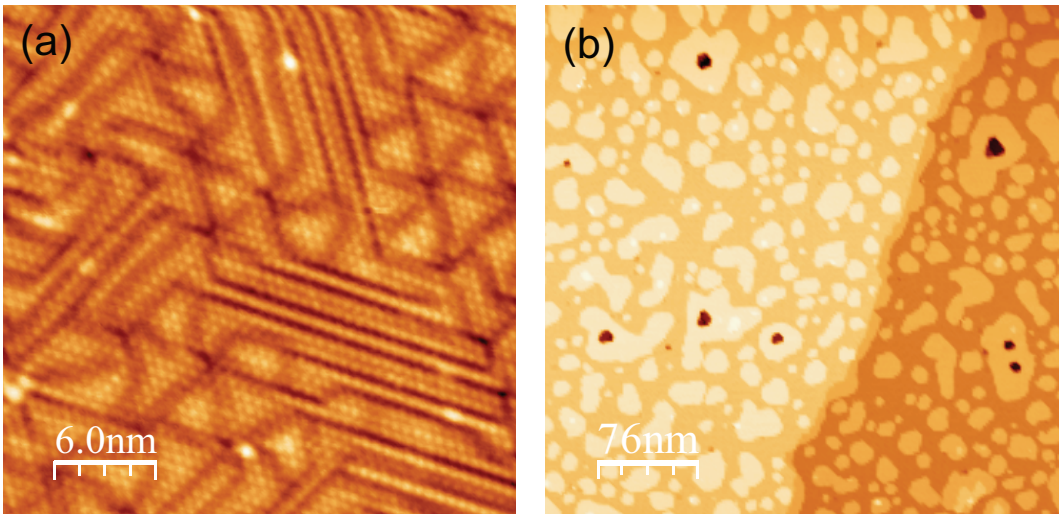

Figure 2.5: (a) The SIC Pb surface mixed with $\sqrt{7} \times \sqrt{3}$ phase. (b) 4 ML Pb films with 1 ML high islands grown on the SIC surface.

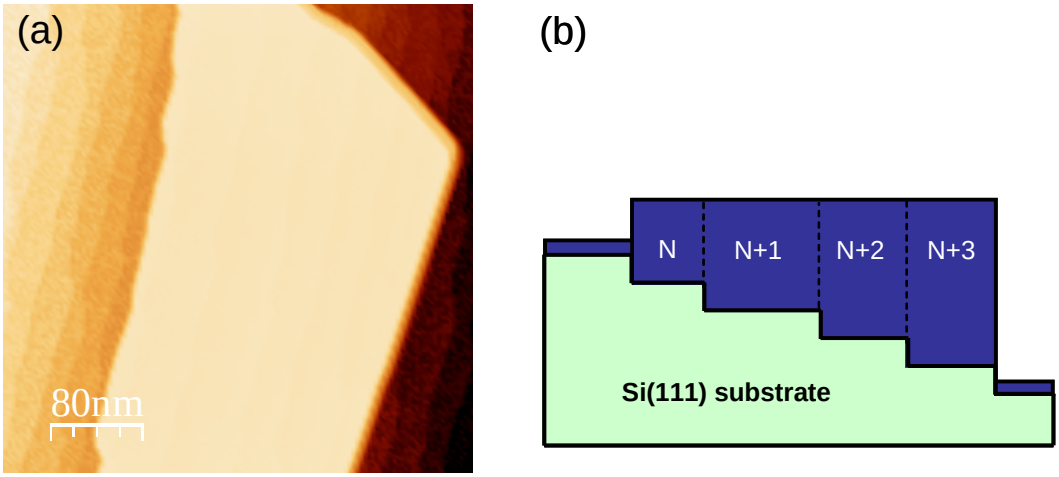

Figure 2.6: (a) Flat-top mesa formed on Si(111)-7×7 surface. (b) Schematic of a mesa structure. Due to the underlying Si steps, this structure has a series of consecutive thicknesses including quantum stable and unstable thicknesses.

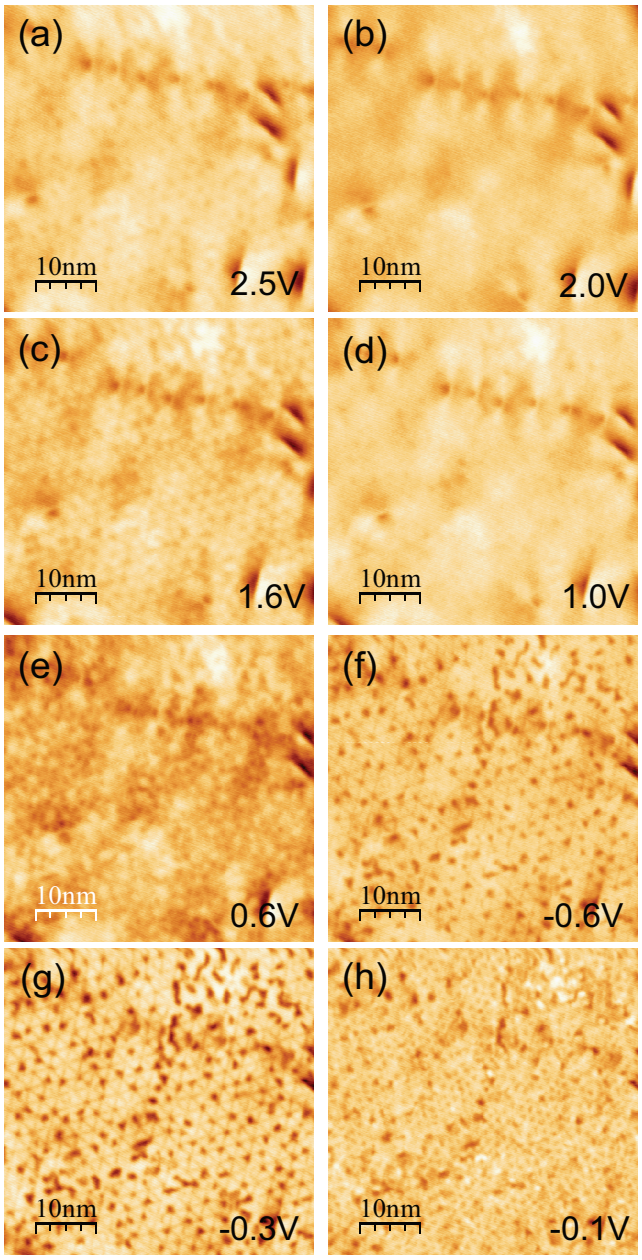

Figure 2.7: Buried Si(111)-7×7 interface under 13 ML thick Pb films is imaged at various sample biases from 2.5 V to -0.1 V.

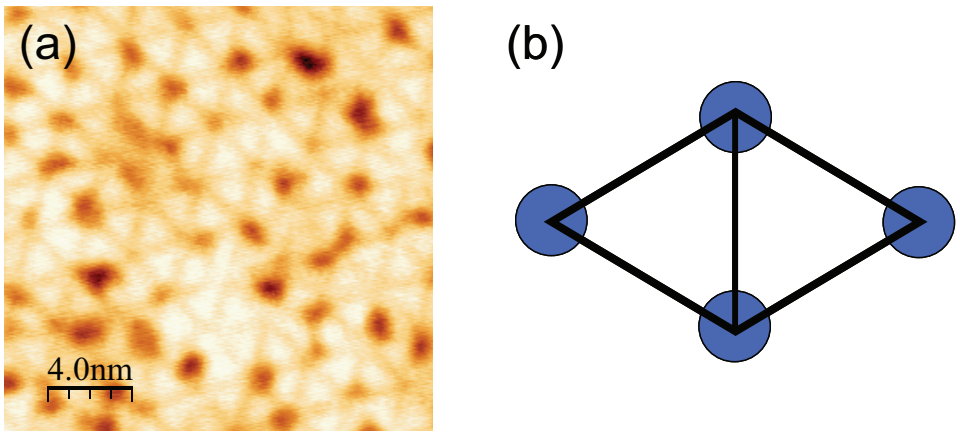

Figure 2.8: (a)Resolved Si(111)-7×7 interface at the sample bias $V_{sample} = -0.3$ V. (b) Corresponding Si(111)-7×7 structure. At this sample bias, each corner hole (blue circle) and dimer chain (black line) of the 7×7 structure are imaged as dark border lines and vertices in (a).

Chapter 3

Measuring Phase Relations of Quantum Size Effects in Ultra-Thin Metal Films: a New Surprise and Its Resolution

Quantum oscillations of work function and film stability as a function of the film thickness in Pb thin films on Si are measured directly using scanning tunneling microscopy and spectroscopy. The comparison of the phase relationship in quantum oscillations (surface energy vs. work function) reveals a complete surprise: in contrast to a theoretically predicted 1/4 wavelength phase shift in the phase relationship, we found that their quantum oscillations have identical phase. A solution to this new puzzle is also provided.

3.1 Introduction

As discussed in the earlier chapter, many studies examine the Pb on Si(111) system due to its unique phase matching between the Fermi wavelength and the lattice spacing along [111], leading to a bi-layer quantum oscillation phenomenon which has been observed experimentally for many physical properties. Several ab-initio calculations also reveal such quantum oscillations for different physical properties such as the surface energy (E_s) and the work func-

tion (W)[11, 29]. One very interesting feature consistently reproduced from these theoretical calculations is the phase relationship in the quantum oscillations of the surface energy and the work function as a function of the film thickness (E_s vs. L and W vs. L): they are not in phase – within a quantum beat period of about 9 ML, these two quantities (E_s and W) are roughly in phase for half of the period and out-of-phase for the other half, as shown in Fig. 3.1 [30]. A recent model calculation further elucidated this phase relationship as a consequence of a *quarter wavelength* phase shift.

The 1/4 wavelength shift is with respect to a continuous variable of L. Since L is discrete in reality, it leads to an alternating in-phase and out-of-phase relationship. As the work function property is dominated by the quantum well states (QWS) near the E_F, and E_s is a property due to all QWS below E_F, a quarter wavelength shift seems to be a natural consequence: the integral of an oscillatory function leads to another oscillatory function which is phase shifted by $\pi/2$. Experimentally, photoemission studies of the Ag/Fe(100) system provide some supporting evidences for this $\pi/2$ phase-shift relationship, albeit only over two quantum oscillation periods [30–32]. Interestingly, no experimental determination of this phase relationship had been carried out for Pb on Si(111) – the most widely investigated quantum thin film system.

By using scanning tunneling microscopy and spectroscopy (STM/S), we report the first direct experimental determination of the phase relationship between quantum oscillations of E_s vs. L and W vs. L. To our surprise, such a

$\pi/2$ phase shift relationship is *completely absent* in Pb on Si(111). In fact, these two quantities ($E_s(L)$ and $W(L)$) are in-phase within a large layer thickness range (from 9 to 20 ML), spanning over 6 oscillation periods. We further propose a model to account for the total absence of a phase shift.

3.2 Materials and methods

All experiments were carried out in a home-built low-temperature UHV-STM at a base pressure $<1.0\times10^{-10}$ torr. STM measurements were carried out either at 78 K or 6.5 K with the same result. Si(111) wafers (n-doped with a resistivity of 0.022-0.06 Ω cm) with 1.1° miscut toward $[\overline{11}2]$ were utilized. Pb was deposited on a Si(111)-7×7 surface from a thermal evaporator with typical growth rate of 0.4 ML/min at room temperature which results in flat-top mesas. Additional 0.1 ML Pb was deposited on such mesas while a sample was kept at 95 K during the growth and further annealed to 145 – 255 K. WSxM software was among the tools used for image preparation an analysis [34].

3.3 Results and discussion

There already exists a vast amount of literature investing the quantum stability (i.e. E_s vs. L) of the Pb/Si(111) system. For example, by investigating the height distribution of 2D Pb islands either using STM [12, 35–37] or using x-ray scattering [17, 38], a probability distribution can be associated with the quantum oscillations of the film stability. A different approach uses STM

to investigate the extended thin film growth as a function of layer thickness, from which only the "quantum stable" thicknesses are observed [22]. Here we use yet another approach to determine the quantum stability based on homo-epitaxial growth of additional 2D islands on flat-top mesas, as described below. This approach has additional advantages of allowing us to simultaneously correlate QWS locations, quantum stability (E_s) and work function (W) as a function of the thickness, thus enabling unambiguous determination of the phase relationship of E_s vs. W.

Shown in Fig. 3.2(a) is a STM image of a typical mesa structure before an additional Pb deposition. On such a mesa, QWS and W as a function of layer thickness can be simultaneously determined and their relationship can be directly correlated. The QWS determination is rather straightforward. Aided by a differential conductance image (dI/dV) (Fig. 3.2(b)) which is mapped simultaneously with a topographic image at a sample bias of $V_{sample} = 1$ V, each layer of a mesa can be distinguished. Using scanning tunneling spectroscopy (STS), distinctive QWS peaks can be measured on every layer of the mesa and its thickness can be directly assigned from the topographic height of such layers. A series of spectra representing QWS of 9 – 16 ML is shown in Fig. 3.2(c) as examples. Note that the sample bias where Fig. 3.2(b) is taken is marked with a green arrow in each spectrum. It is clearly shown that the contrast of the differential conductance image is directly related to the local density of states: the bright contrast corresponds to higher LDOS due to the presence of QWS peak near a given sample bias. As shown in this figure,

$V_{sample} = 1$ V is a good choice for the conductance image to distinguish each thickness since the local density of states oscillate relative to this energy at 1 eV: even thicknesses have a QWS peak closer to 1 eV than odd thicknesses. This oscillation results in clear contrast alternation every other layer in the differential conductance image which facilitates the distinction of each layer. In this way the relationship between the QWS and the thickness can be experimentally established. The determination of work function, on the other hand, is not trivial. Earlier attempts using STM to measure the tunneling decay constant yielded incorrect results. Recently, Kim *et al.* [19] revealed that correct work function variations in Pb quantum films can be measured using STM only by probing states near the Fermi energy. Here we adopted the same approach. Shown in Fig. 3.3(a) is a differential conductance image taken at 1 V; Figs. 3.3(b)-(c) are spatial mapping of dI/dZ acquired at ± 10 mV respectively, exhibiting the work function contrast at different thicknesses. The measured decay constant κ as a function of thickness is plotted in Fig. 3.3(d) accompanied by the measured QWS locations shown in Fig. 3.3(e). Consistent with the observation earlier, strong suppression of the work function occurs when the QWS crosses the Fermi energy.

To reveal the modulation of surface energy due to the quantum confinement effect, we utilize the phenomena of selective homo-epitaxy of additional 2D islands on originally flat-top mesas which contain a large range of thicknesses, including both stable and unstable thicknesses. When an additional 0.1 ML of Pb is deposited on typical mesas at low temperature (95 K) and

further annealed to 145 K for a few minutes, fractal shaped islands with 1 ML height are observed on mesas (Fig. 3.4(a)). This fractal shape is more clearly observable in Fig. 3.4(b), which is a magnified image of the marked area in Fig. 3.4(a). Fig. 3.4(c) shows a schematic of this system. Note that the initial Pb deposition for mesa structures is done at room temperature, but additional Pb deposition resulting in fractal islands is done at low temperature. The fractal shape is a characteristic of Diffusion-Limited Aggregation (DLA) [39, 40] which results from the low mobility of deposited Pb atoms at the experimental growth temperature (95 K).

After the initial growth, the same sample is annealed to higher temperatures without further deposition of Pb. The evolution of the island′s shape is shown in Figs. 3.5(a)-(c). Initially, islands preserve their fractal shapes up to the annealing temperature of 195 K, but they start to change at higher annealing temperatures: more rounded shapes with fewer branches appear at 225 K (Fig. 3.5(b)) and elongated circular shapes with no branches appear at 255 K (Fig. 3.5(c)). While the initial fractal-shaped islands span over 2-3 layers, the sign of the correlation is visible: islands seem to be preferentially centered on regions of specific thicknesses, as shown in Fig. 3.5(d). After further annealing, this preference evolves into a total confinement of individual islands within certain thicknesses, as shown in in Fig. 3.5(f). As discussed below this phenomenon is a direct manifestation of the thickness dependent surface energy.

The formation of flat-top mesa structures is a result of an energetic

competition between the surface energy due to vertical quantum confinement and the step energy. Flat-top geometry is established in order to avoid a high energy cost from multiple step formation and, as a consequence, quantum stable and unstable thicknesses coexist in one mesa. When additional Pb atoms are deposited on the surface, the 2D islands that form inevitably contain step-edges at the island boundary, regardless of whether they are on top of the stable or unstable thicknesses. Therefore, it is only the surface energy that determines the formation of 2D islands. Consequently, 2D islands are preferentially formed on the originally quantum unstable thicknesses to convert the local region into a quantum stable thickness. Therefore, by monitoring the evolution of Pb islands on a mesa, quantum "unstable" (high surface energy) thicknesses are successfully assigned.

Table 3.1 shows the results of our statistical analysis of the system. In order to confirm the relationship between an island distribution and Pb thickness, the total area of a specific thickness covered with islands is analyzed by observing 4-5 mesas at each annealing temperature. Note that most of the mesas we studied have a thickness ranging from 9 – 20 ML and only a few mesas showed higher thicknesses (21 – 24 ML).

Fig. 3.6(a) shows the island distribution (percentage coverage) as a function of thickness at each annealing temperature. Each data point is based on a statistical analysis of 4-5 mesas; each mesa is approximately 100,000 nm^2 on average. The layers ranging from 9 to 19 ML are observed on almost all mesas in our study with the sampled total area of each layer being more

ML	145 K		225 K		255 K	
	Number of mesas	Total island area (nm^2)	Number of mesas	Total island area (nm^2)	Number of mesas	Total island area (nm^2)
9	5	32761	5	29636	4	40543
10	5	50334	5	42222	4	45762
11	5	62092	5	38303	4	43632
12	5	64229	5	53418	4	46978
13	5	50308	5	38302	4	48825
14	5	69625	5	47148	4	52624
15	5	72423	5	44768	4	43231
16	5	64595	5	39121	4	44018
17	5	40092	5	36725	4	40414
18	5	49672	5	40900	4	29907
19	4	32093	4	24011	4	18765
20	3	28001	4	15157	2	12301
21	2	4858	2	8443	1	5243
22	2	6098	1	4122	1	3637
23	1	4043	1	4475	1	3250
24	0	0	1	2793	1	2953

Table 3.1: Statistical results of observed 1 ML high islands on mesas at a given annealing temperature. The number of mesas where a given thickness is observed is specified and the total area covered by the additional islands is recorded at each thickness.

than 18,000 nm^2. 20 ML is observed on fewer mesas (2-3 mesas) with a total area of more than 12,000 nm^2 (Table 3.1). The layers observed only on one mesa among all studied mesas are excluded from further analysis (Fig. 3.6(a)) due to too small of a sample size. As one can observe, even at the lowest annealing temperature of 145 K, bi-layer oscillation of island distribution is quite obvious and its tendency gets stronger with further annealing. At 255

	Interface	Stable Thickness										
From ref. [22]	Si(111)-7×7-Pb	5	7	9	11	13	14	16	18	20		
	Si(111)($\sqrt{3}\times\sqrt{3}-\alpha$)	5	7	9	11	13	14	16	18	20	22	25
	Ge(111)($\sqrt{3}\times\sqrt{3}-\alpha$)	5	7	9	11	13	14	16	18	20		
Our result	Si(111)-7×7-Pb			9	11		14	16	18	20		

Table 3.2: Comparison between the stable thicknesses reported in ref. [22] and our result. The thicknesses marked with red color indicate cross-over regimes.

K, odd layers before 12 ML and even layers after 12 ML show almost no island distribution which indicates these layers are quantum stable – lower surface energy. This is summarized in Table 3.2 with the result done by M.M. Özer *et al.* [22] for the comparison. In their study, M.M. Özer *et al.* deposited Pb on three different interfaces at low temperature (150 K) and annealed to higher temperature (210 K – 300 K) to form a uniform film. They monitored thicknesses of such a uniform film with various Pb coverage. As discussed in Chapter 2.2.1.1, only stable thicknesses can form globally uniform flat films so that these observed thicknesses represent stable thicknesses. As shown in Table 3.2, our determination of stable thicknesses is consistent with theirs. Thus, Fig. 3.6(a) effectively represents E_s vs. L: a high peak corresponds to high surface energy and a low peak corresponds to low surface energy. When compared to experimentally measured work functions as a function of thickness (Fig. 3.6(b)), much to our surprise, E_s vs. L is perfectly in phase with W vs. L: all the low work function locations correspond to the locations of low quantum stability and vice versa. The predicted $\pi/2$ phase-shift is not observed.

3.4 Conclusions – new model

The work function properties are dominated by the QWS near E_F, while E_s results from the contribution of all QWS channels below E_F; a 1/4 wavelength phase shift seems to be a natural result. What could be responsible for this total absence of a 1/4 wavelength phase-shift between W vs. L and E_s vs. L ? Here we propose a model. We believe that there is an underlying connection between this apparent mystery and several intriguing phenomena related to the quantum thin films of Pb on Si(111) which have been recently investigated. The first is the anomalous slow decay of the Friedel oscillations as a function of thickness recently investigated theoretically by Jia *et al.* [41]. They found that due to Pb's nearly flat Fermi surface perpendicular to the [111] direction, the Friedel oscillations persist much longer as a function of layer thickness, having a $1/L$ decay instead of a more typical $1/L^2$ dependence in other metals such as Cu or Al. A nearly flat Fermi surface implies a large lateral effective mass for states near E_F. Reported even earlier by using angle-resolved photoemission spectroscopy (ARPES) is the anomalous mass enhancement of lateral effective mass, m^*, for the highest occupied QWS in the Pb/Si quantum films: the enhancement is nearly one order of magnitude [42, 43]. While the two phenomena are consistent, the ARPES studies provided additional information which is important to our model: the mass enhancement is absent for deeper occupied QWS. For a 2D electronic system, the density of states (DOS) is directly proportional to its effective mass. Thus while all occupied QWS contribute to the total surface energy, the anomalously

large m* makes the QWS channel near the E_F the most dominant electronic contributor. In the mean time, the work function is also dominated by QWS near the Fermi energy; thus it is not surprising that E_s vs. L and W vs. L would have the same phase in quantum oscillations. The apparent inconsistency is resolved.

There is additional experimental evidence to support this resolution. In all STS studies of Pb quantum films, sharp resonances are observed for unoccupied QWS and the highest occupied QWS. However, such sharp resonances are not observed for deeper occupied QWS. This can be seen in the STS spectra displayed in Fig. 3.2(c). The sharpness of QWS resonance is more like a sharp DOS due to a Van Hove singularity, which would be consistent with a flat dispersion.

In summary, we have experimentally investigated the phase relationship of the quantum oscillations phenomena of surface energy and work function (i.e. E_s vs. L and W vs. L) in Pb thin films on Si(111). Contrary to a 1/4 wavelength phase shift predicted theoretically, we found that there is no phase shift relationship. We further resolve this apparent inconsistency by relating this phenomenon to the anomalous lateral mass enhancement for the highest occupied QWS.

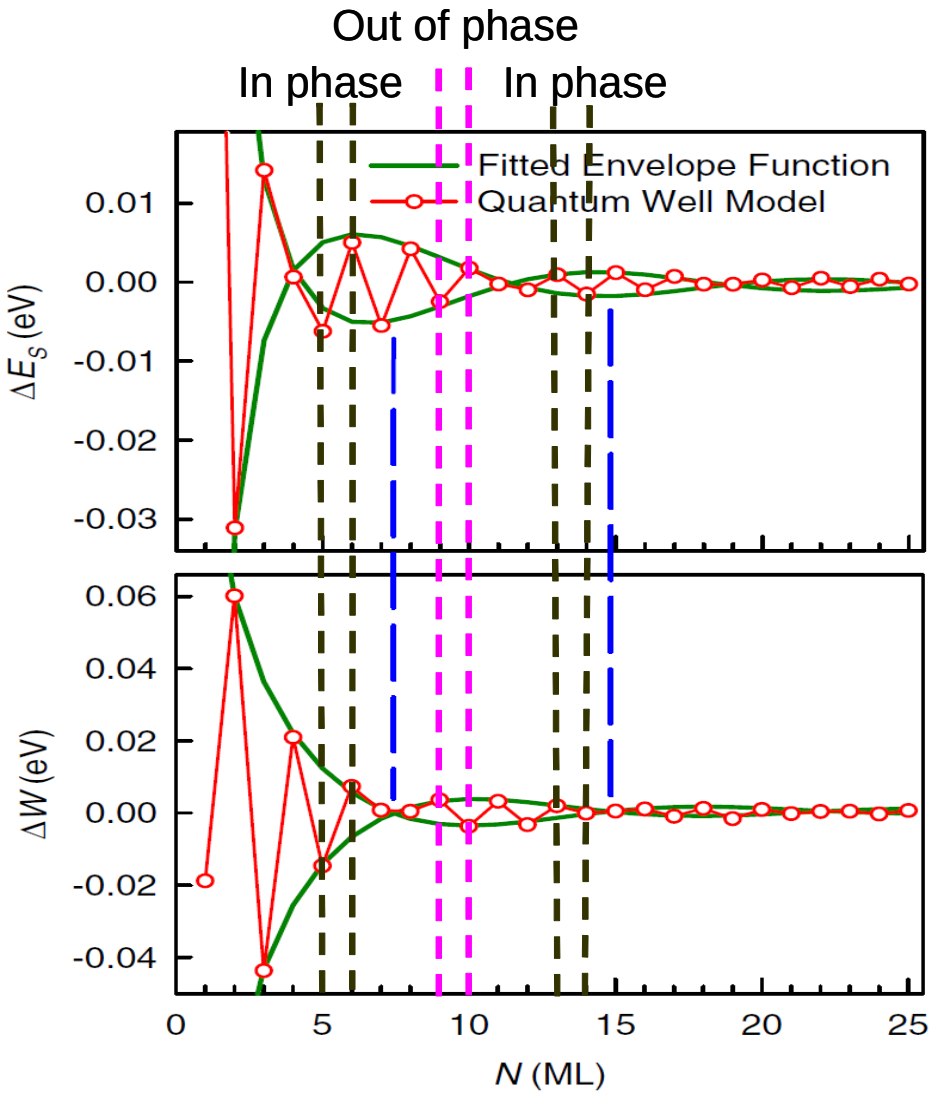

Figure 3.1: First-principles calculations done for freestanding Pb(111) films. Surface energy E_s per surface atom and work function W as a function of thickness N. Envelope functions are derived from a model and shown as solid green lines. The thicknesses where the E_s and W are in phase (out of phase) are marked with dashed black (pink) lines [30, 33].

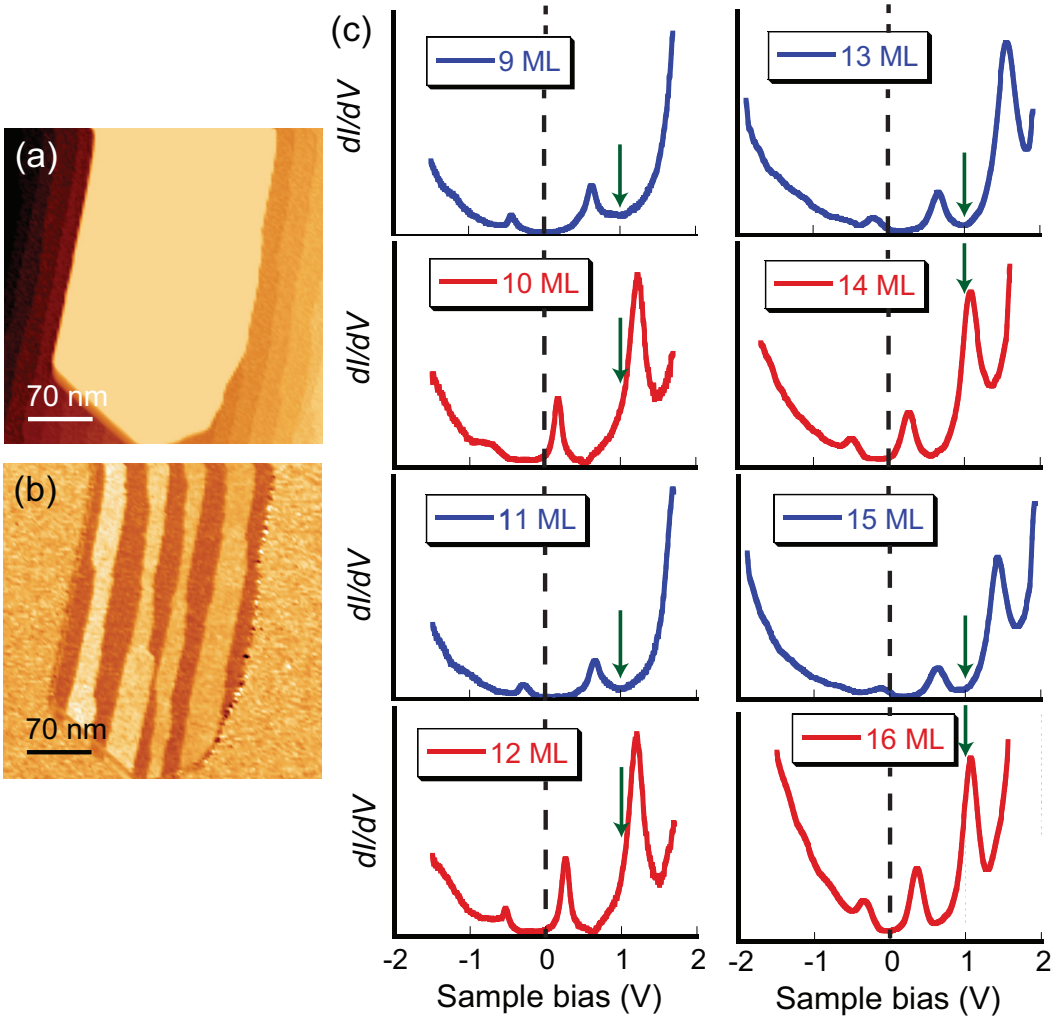

Figure 3.2: (a) Topographic image of mesa structure. (b) Differential conductance image taken simultaneously with (a) at sample bias, V_{sample} =1 V. (c) A series of spectra showing QWS of each thickness (9 – 16 ML).

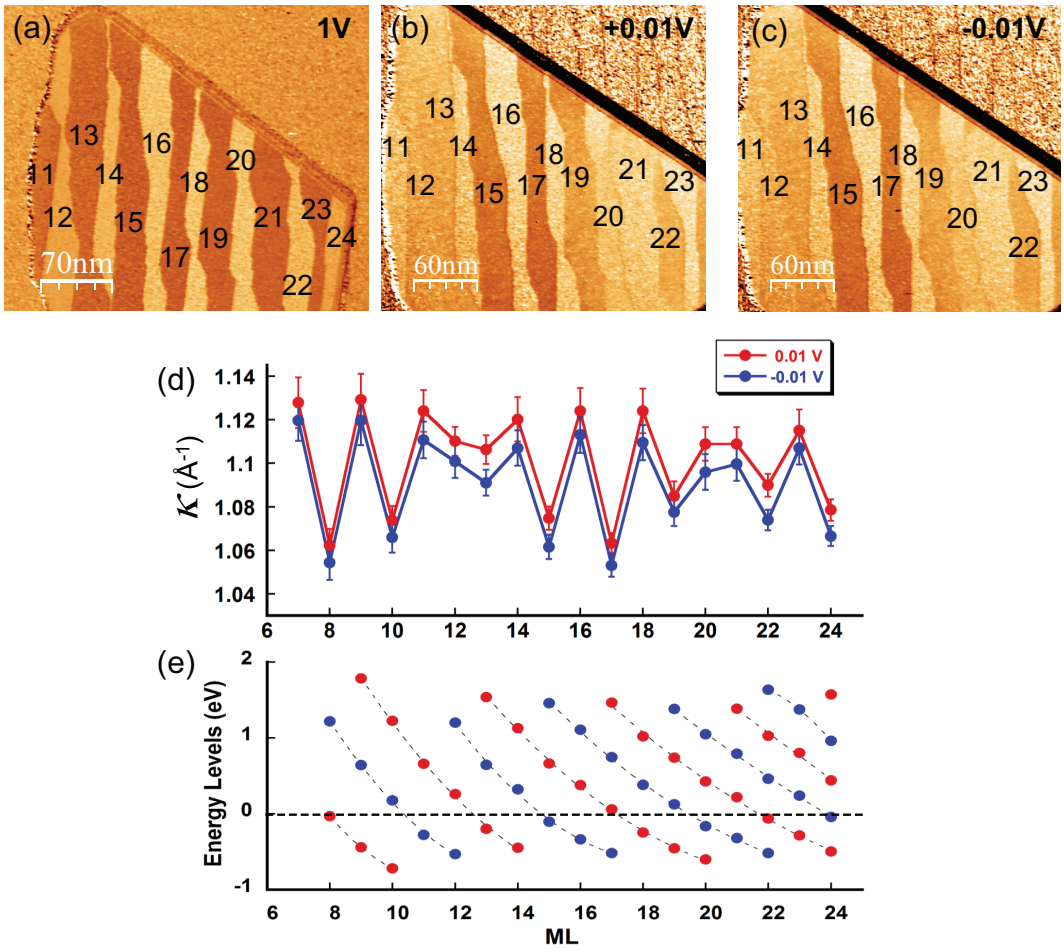

Figure 3.3: (a) Differential conductance image taken at the sample bias of V_{sample} =1 V. (b-c) The corresponding dI/dZ images acquired at V_{sample} = ±0.01 V, respectively. (d) The tunneling decay constant, κ, as a function of thickness, acquired at the very low sample biases. (e) The QWS locations as a function of thickness. The dashed line at 0 eV represents the Fermi energy (E_F).

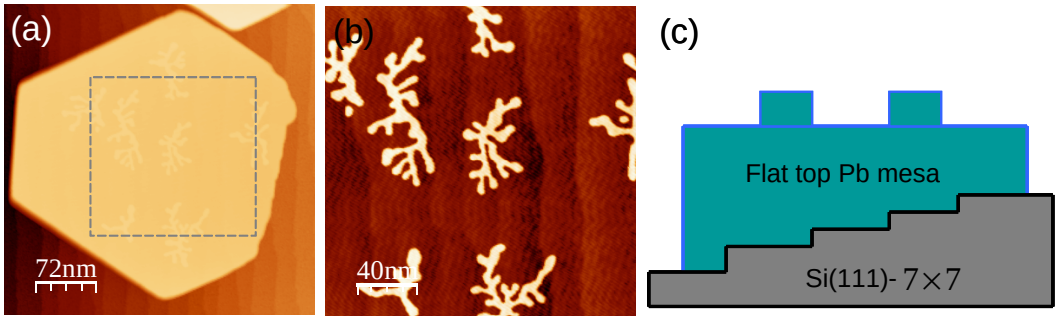

Figure 3.4: 1 ML high Pb island formation after additional 0.1 ML Pb deposition at low temperature (95 K). (a) A mesa with fractal shaped islands. (b) Magnified image of the area marked in (a) with a square. (c) A schematic of this structure.

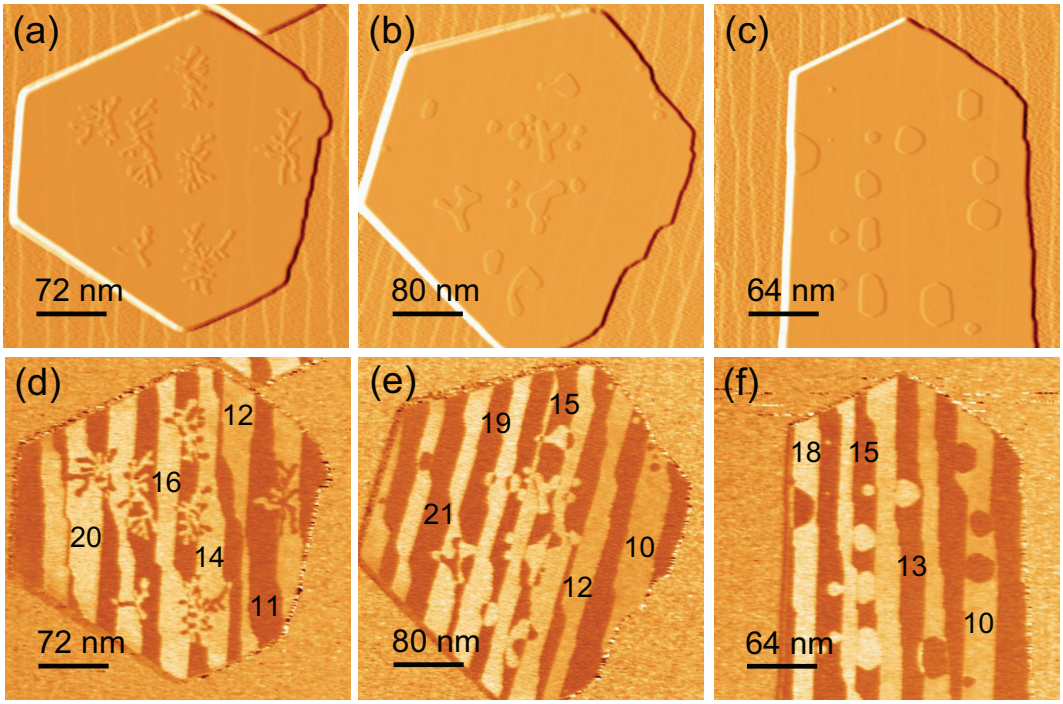

Figure 3.5: (a – c) STM topographic images (light shaded for a better recognition) showing the distribution of Pb islands grown on mesas. Initially 0.1 ML of Pb is deposited and the same sample is further annealed. After annealing to (a) 145 K, (b) 225 K, and (c) 255 K. (d – f) Simultaneously taken differential conductance images (dI/dV) at the sample bias of $V_{sample} = 1$ V. At this bias, bright (dark) contrast represents even (odd) layers. Several layers are marked for distinction.

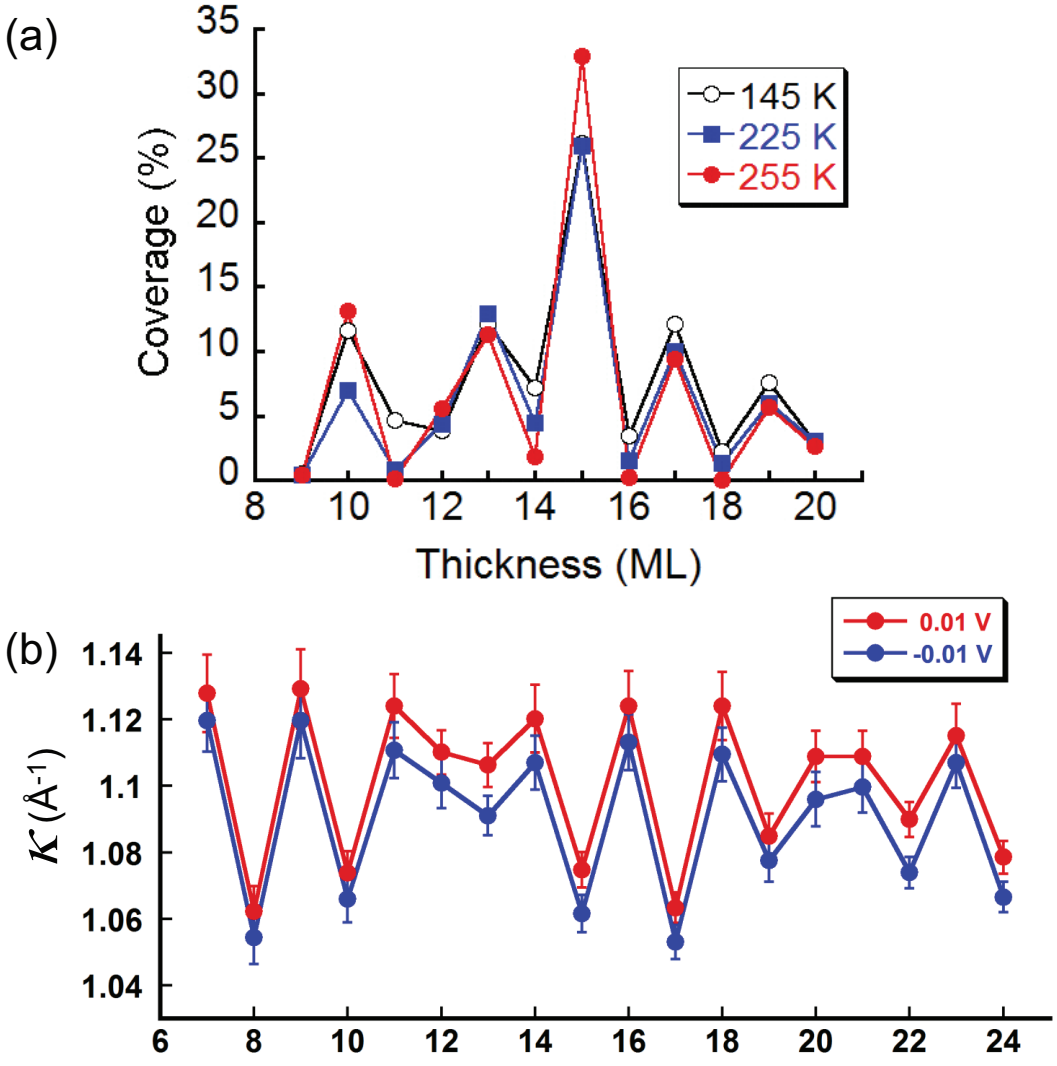

Figure 3.6: (a) Quantitative analysis of the Pb island coverage (%) as a function of thickness (ML) for each annealing temperature. (b) Measured κ as a function of thickness at the sample bias of $V_{sample} = \pm 0.01$ V.

Chapter 4

Atomic Scale Control of Catalytic Process in Oxidation of Pb Thin Films

Using scanning tunneling microscopy (STM), we demonstrate that oxidation on Pb films is greatly enhanced by atomic Cs catalysts. With only a minute concentration of isolated Cs substitutional atoms in the surface layer (0.004 ML coverage), surface oxidation rates are greatly enhanced. First-principles density functional theory (DFT) calculations reveal that a substitutional Cs atom strongly increases O_2 binding on the surface. Then, with additional oxygen exposure this substitutional Cs-initiated oxidation process results in growth of PbO layers in an auto-catalytic manner. Furthermore, we investigate the role of temperature in the oxidation of the Pb films with and without Cs, and we explore the overall morphology of the resultant oxide layers.

4.1 Introduction

Catalysis is a subject of great interest, both from a fundamental chemistry point of view and in light of its technological importance. Recent fundamental studies of chemical reactivity and catalysis of elegantly fabricated

novel materials have led to a wealth of important advances as regards enhanced functionality via dimensionality reduction. As a prominent example, gold, a noble metal, is exceptionally inert in three-dimensional (3D) bulk form, but becomes highly reactive when adopting 1D nanocluster form [44–48] or 2D form in supported atomic layers [49, 50]. Another class of systems which exhibit enhanced chemical reactivity is bimetallic alloys formed at the surface of a metal substrate upon adsorption of another type of metal, with the two metals being immiscible in 3D bulk form [51–59]. Since chemical processes occur at an atomic scale, it is not surprising that the modification of local atomic environments could significantly influence chemical processes. Specifically how this occurs, however, varies dramatically from case to case, and is a topic of fundamental interest.

Oxidation of Pb is a very interesting case. It is well known that pure crystalline Pb is rather inert to O_2 adsorption. What chemical processes are responsible for the formation of PbO? In 2002, Thürmer *et al.* used scanning tunneling microscopy (STM) to investigate the nucleation and growth of PbO on Pb surfaces at the initial stage. They discovered that for atomically clean Pb(111) surfaces, the initial oxidation occurs at unspecified point defect sites. Once initiated, rapid 2D growth of PbO occurs through an autocatalytic process. While this study shed new light on the oxidation process of Pb, several key questions remained. The most important one concerns the nature of the atomic defects. Why and how do these point defects initiate oxidation? Moreover, how does the auto-catalyzation proceed?

In the present study we have sought to address these critical questions by experimentally controlling the specific nature of atomic scale defects – in this case, substitutional Cs atoms. Our investigative approach relies on scanning tunneling microscopy (STM) aided by first-principles density functional theory (DFT). Specifically, we have found: (a) oxygen preferentially bonds to Cs atoms on the surface, and they form the nucleation sites for PbO – in fact, these are far more effective nucleation sites than defect sites such as stacking faults, or step edges; (b) from these nucleation sites, PbO grows laterally by consuming Pb atoms in neighboring areas on the surface. The role of temperature in oxidation is also addressed.

4.2 Materials and methods

4.2.1 Sample preparation

All experiments were carried out in a home-built low-temperature UHV-STM at a base pressure $<1.0\times10^{-10}$ torr. STM images were taken with PtIr tips and at a temperature of 78 K. Globally flat Pb films were grown by a well-known two step method [8]. Cs was evaporated from a getter source, as described in ref. [60], onto the Pb films. 1 ML Cs corresponds to 1 Cs atom sitting at each Pb surface lattice site. The surface was exposed to properly cleaned and purged gaseous O_2 in-situ via a leak valve, with exposure pressures between 2×10^{-7} and 1×10^{-6} torr. O_2 was deposited on Pb films at T = 155 K and annealed to T = 260 K in most cases, but in some instances was deposited near room temperature ($\sim$ 290 K), as specified below. WSxM

software was among the tools used for image preparation and analysis [34].

4.2.2 First-principles calculations

The first-principles calculations were performed using the VASP code [61], which is based on density functional theory (DFT) and employs pseudopotentials within the projector augmented wave (PAW) scheme [62, 63]. To more accurately evaluate O_2 adsorption energies on Pb substrates, we used the revised Perdew-Burke-Ernzerhof functional (RPBE) for exchange-correlation [64]. The 6s and 6p electrons of Pb; the 5s, 5p, and 6s electrons of Cs; and the 2s and 2p electrons of O are treated as valence electrons in the pseudopotentials. The default plane-wave energy cutoff for O, 400.0 eV, was consistently used in all the calculations. The calculated crystal parameters for bulk Pb are a= 5.035 Å, in good agreement with the experimental value of 4.95 Å[65]. The Pb(111) surface is modeled by a 4×4 surface slab, consisting of four atomic layers and a vacuum region of 18 Å. For Brillouin Zone integration, we used a 5×5×1 k-point mesh including the point (0,0,0) [66]. The atoms in the bottom layer are fixed at their bulk positions during the relaxation. Optimized atomic geometries are obtained when the forces on all the unconstrained atoms are smaller in magnitude than 0.01 eV/Å. We use the climbing image nudged elastic band method (NEB) [67], followed by spline interpolation, to determine the diffusion pathways and energy barriers.

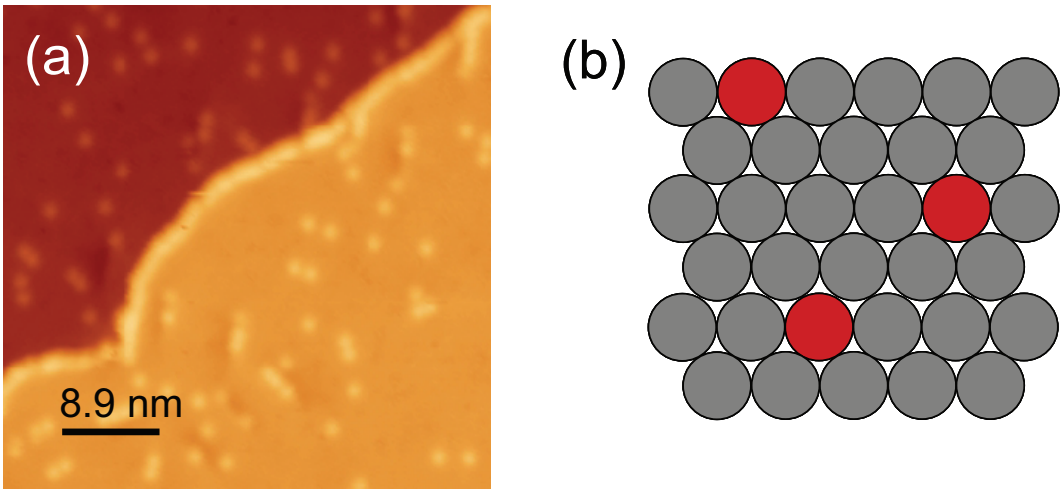

Figure 4.1: (a) (Before oxygen exposure) Substitutional Cs atoms with 0.004 ML coverage on 14 ML Pb film grown on a Si(111)-7×7 surface. $V_{sample} = +1.2$ V. (b) A schematic showing Cs atoms (red) incorporated into the substitutional sites of a Pb (grey) surface.

4.3 Results and discussion

Utilizing two step growth [8], an atomically flat 14 ML Pb film is first obtained before subsequent Cs exposure [22, 68]. After Cs deposition, Cs atoms preferentially decorate step edges and form a Pb surface with substitutional Cs atoms [60]. Fig. 4.1(a) shows the STM image of the Pb surface with a coverage of 0.004 ML of Cs. As explained in ref.[60], the bright step edge indicates the Cs step-decoration and the bright dots on the terrace are substitutional Cs atoms. Fig. 4.1 shows a schematic of the Pb surface with Cs atoms in substitutional sites. Note that STM images were taken at $\sim$ 6 K in ref.[60] but here the image was taken at 78 K. At our experimental temperature it is hard to get clear atomic resolution of Cs atoms at step edges, but substitutional

Cs atoms are distinguishable on terraces. The STM tip is also more interactive with the Cs atoms on the surface while scanning. Therefore, the sample bias is chosen to be around 1 V in most cases where STM tip is less interacting with the Cs atoms presenting scanning surfaces.

After 0.004 ML of Cs is deposited, the same sample is exposed to oxygen. Fig. 4.2(b) shows the initial Pb film topography with a coverage of 0.004 ML of Cs before the oxygen exposure. Upon exposure of 2 Langmuirs (L) oxygen at 155 K on this Pb surface with substitutional Cs atoms and subsequent annealing to 260 K, the initial oxidation occurs (Fig. 4.2(c)). Interestingly, oxidation occurs along the step, which was originally decorated by Cs atoms before the exposure. This preferential step oxidation is not found in the case of 1 L oxygen exposure on the bare Pb surface (no Cs atoms) in Fig. 4.2(d). Moreover, the density of oxide clusters in Fig. 4.2(c) is similar to the original Cs atom density (Fig. 4.2(b)). These observations suggest that oxidation first occurs preferentially where Cs atoms were present before the exposure: clusters, most likely CsO or PbO in origin, form at these sites. During the oxidation process, a small pit starts to appear around clusters as shown in Fig. 4.2(c). Fig. 4.2(a) is a line profile across the dip and cluster marked by the arrow in Fig. 4.2(c).

Oxide clusters formed during the initial exposure (Fig. 4.3(a)), regardless of their chemical nature, catalyze the subsequent growth of PbO, as shown in Figs. 4.3(b) – 4.3(d). In these images, the same sample is exposed to additional oxygen without further introduction of Cs. In contrast to the

defect-initiated oxidation reported earlier, PbO is nucleated effectively on terraces due to substitutional Cs atoms. After nucleation, PbO grows laterally with additional oxygen exposure; the required Pb atoms are supplied from the neighboring area on the surface layer, due to the low mobility of Pb atoms at the exposure temperature (155 K). This process results in a significant morphological change: as oxygen exposure increases, the darker contrast regions grow in the vicinity of oxidation sites. To further clarify the role of Cs, a Cs-free Pb surface was oxidized with similar oxygen doses. Figs. 4.3(e) – 4.3(h) demonstrate that a clean Pb film (16 ML) is much more inert to oxidation. The overall oxidation process in this case is similar to the case of Pb with substitutional Cs atoms, but the initial nucleation rate is much lower (Fig. 4.3(e)), which delays the lateral growth of PbO. It is clearly shown that only after 32 L of oxygen exposure is the cluster density on a clean Pb film (Fig. 4.3(g)) comparable to the cluster density on a Pb surface with substitutional Cs atoms after 2 L oxygen exposure (Fig. 4.3(a)).

Our first-principles calculations reveal that the substitutional Cs atom greatly enhances O_2 binding on the surface. Figure 4.4 shows the most stable atomic structure for an O_2 molecule at a Cs substitutional site: the O_2 molecule adsorbs at the hcp hollow site adjacent to the embedded Cs atom and is oriented along the $[1\bar{1}0]$ direction. The distance between the Cs atom and the two O atoms is equally 2.80 Å. The bond length of the O_2 molecule is stretched from 1.24 Å in free space to 1.46 Å after the adsorption. The calculated adsorption energy of a single O_2 molecule at the Cs substitutional site on the

Pb surface is -1.22 eV, which is much stronger than that on a clean Pb(111) surface (-0.58 eV) [69]. Thermodynamically, the Gibbs free energy of gas-phase O_2 at the experimental pressure of 1×10^{-7} torr and temperature of 155 K is estimated to be -0.52 eV per O_2 molecule [70], only slightly higher (0.06 eV) than the adsorption energy of O_2 molecules on the clean Pb(111) surface, but much higher than that at the Cs substitutional site (0.70 eV). This suggests that under the experimental conditions, adsorption of O_2 molecules should indeed be greatly enhanced by atomic-scale Cs catalysts. We further investigated the dissociation barrier of an O_2 molecule at a Cs substitutional site. The calculated activation barrier is 0.51 eV. Though this barrier is higher than the dissociation barrier of an O_2 molecule on a clean Pb(111) surface (0.27 eV), the estimated rate coefficient based on the Arrhenius equation for O_2 dissociation at a Cs substitutional site is 103 s^{-1}, large enough to facilitate surface oxidation at the experimental annealing temperature of 260 K. The atomic structures and corresponding energies of the transition state and the final state are also shown in Fig. 4.4. At the transition state, the two O atoms are separated by 1.88 Å. After the dissociation, the O atoms reside at adjacent surface fcc and hcp hollow sites, respectively, and the total energy is lowered by 2.28 eV relative to the initial state.

In Fig. 4.5, the catalytic role of Cs is shown quantitatively, with the overall oxide coverage illustrated as a function of exposure. The total oxidized area increases with the exposure of oxygen for both surfaces. The difference in slopes is small, but it is evident that the initial coverage is significantly higher

on the Pb surface with substitutional Cs atoms. Thus, the substitutional Cs atom enhances the oxidation rate of the Pb surface by enhancing the nucleation rate of oxygen clusters.

It is particularly illuminating to compare the present study with work involving Pb crystallites [71] and bare Pb mesas [13]. In the work of Ma *et al.*, it was found that oxygen adsorption on thin Pb films can occur within a specific temperature window that is below room temperature. Following adsorption, oxidation occurs when the sample is annealed to a higher temperature. This process is similar to our procedure for oxidation of the clean Pb film. In the work of Thürmer *et al.* it was found that, while a clean Pb surface is inert, oxidation is initiated by the presence of some unknown impurities and continues by an auto-catalytic process. Our work indicates that by the incorporation of a minute amount of Cs into the Pb surface layer, one can dramatically enhance the initial oxidation rate. After this initial oxidation, the growth of PbO follows a similar auto-catalytic process as described by Thürmer *et al.* The main difference is that in our work, every Cs atom in a substitutional site can initiate this process.

When a typical Pb surface with substitutional Cs atoms is annealed to room temperature, the surface undergoes a morphological change. The inset of Fig. 4.6 shows a Pb film covered by 0.0027 ML Cs, resulting in a typical Pb surface with substitutional Cs atoms. When it is slowly annealed to near room temperature ($\sim$ 290 K), the substitutional Cs atoms are ejected from their substitutional sites and agglomerate at the step edges of the Pb film (Fig.

4.6). Pb atoms are much more mobile at room temperature [72] than at low temperature, so once a Cs atom is ejected from its substitutional site, the site can be easily filled with an adjacent Pb atom during the annealing process. The result is terraces that are almost Cs-free, with few-Cs clusters on step edges.

After confirming the effect of temperature on the morphology of the Pb surface with substitutional Cs atoms, a Pb surface more dilutely covered with Cs (0.001 ML) was warmed up and oxygen was deposited at room temperature. Figs. 4.7(a) – 4.7(d) show the initial oxide cluster formation and subsequent growth of PbO islands. Each aggregated Cs cluster at the step edge acts as a nucleation site for growth of high quality PbO islands. Furthermore, in contrast to the low temperature case, the resultant PbO islands have a distinctive shape. Fig. 4.7(i) shows a magnified image of the island in Fig. 4.7(d), and a periodic corrugation is observed. This corrugation is a Moiré pattern caused by overlapping unit cells between the PbO islands and the underlying Pb surface [13, 71].

When compared with the case of oxygen exposure on bare Pb films at the same temperature ($\sim$ 290 K), the role of Cs clusters in the oxidation process becomes clearer. For bare Pb films at lower exposure ($\sim$ up to 6 L) at room temperature, there is no sign of oxidation (Figs. 4.7(e) – 4.7(f)), while PbO clusters are unmistakably found on the Pb surface with Cs clusters at the same exposure and temperature. For the bare Pb film, it is not until 31 L of oxygen exposure that PbO islands are found (Fig. 4.7(g)) and only with

higher exposure ($\sim$ 56 L) are PbO islands distinguished by a Moiré pattern (Fig. 4.7(k)).

These oxide islands are only found at native film defect sites or step edges (Figs. 4.7(j) – 4.7(k)), which indicates that defect sites [72] act as a favorable nucleation site for oxygen adsorption. Oxidation due to defects is, however, much less efficient than oxidation due to the presence of Cs: the density of defects on the Pb surface is high, but only a few of the defects can let oxygen nucleate on the surface, whereas almost all Cs atoms – even those Cs atoms clustered at step edges – act as nucleation sites. It is shown that the presence of Cs has a great impact on the initial sticking probability of oxygen and consequently on the subsequent oxidation, even at room temperature.

There are a few additional observed phenomena that deserve to be mentioned. In the case of low temperature exposure, the Pb atoms required to form a PbO island are supplied from the area immediately adjacent to the island, as observed by the roughing of the films there. However, at room temperature Pb atoms are quite mobile at both step edges and terraces [27], allowing Pb atom migration over relatively long distances and thereby preserving a more energetically favorable flat surface. Moreover, a signature of the catalyzing Cs cluster is shown in Fig. 4.7(i): a small topographic protrusion that appears near the center of the island where the step edge is located. This protrusion, not observed on PbO patches grown on bare Pb films (Figs. 4.7(e) – 4.7(h)), suggests that the island originated from Cs clusters. The last phenomenon is the sample bias dependent contrast modulation in the Moiré pattern of PbO

patches, shown in Fig. 4.8. Fig. 4.8(a) is the image taken after 57 L of oxygen exposure at RT on a Pb surface with substitutional Cs atoms. This image is taken on the same sample shown in Fig. 4.7(d), but at different area. Two small PbO patches are imaged at various sample biases (Figs. 4.8(b) – 4.8(f)) and interestingly, the Moiré pattern of the patches are clearer at certain biases than the others. Note that the underlying Si(111)-7×7 interface is visible in Figs. 4.8(d) – 4.8(f) where the Moiré pattern is washed out. The Moiré pattern shows clear contrast only at the sample biases at which STM is sensitive to surface morphology rather than electron fringe patterns (Figs. 4.8(b) – 4.8(c)).

4.4 Conclusions

In this study, we have demonstrated that oxidation of Pb thin films can be greatly enhanced by the presence of Cs atoms, even with only 0.004 ML coverage. When low temperature (155 K) exposure is followed by annealing to higher temperature (260 K), substitutional Cs atoms provide excellent nucleation sites for oxidation. As confirmed by DFT calculations, substitutional Cs atoms are favorable nucleation sites because they enhance O_2 binding on the surface. After initial nucleation, oxidation follows an auto-catalytic process, consuming neighboring Pb atoms on the surface. When the Pb surface with substitutional Cs atoms is annealed to near room temperature, substitutional Cs atoms diffuse and agglomerate at step edges. These clustered Cs atoms further function as favorable oxidation sites when subsequently exposed to

O_2. Similar to low temperature oxidation, this room temperature oxidation proceeds auto-catalytically, resulting in the growth of smooth oxide islands on the surface. In this case, the Pb surface remains flat due to the high mobility of Pb atoms at room temperature.

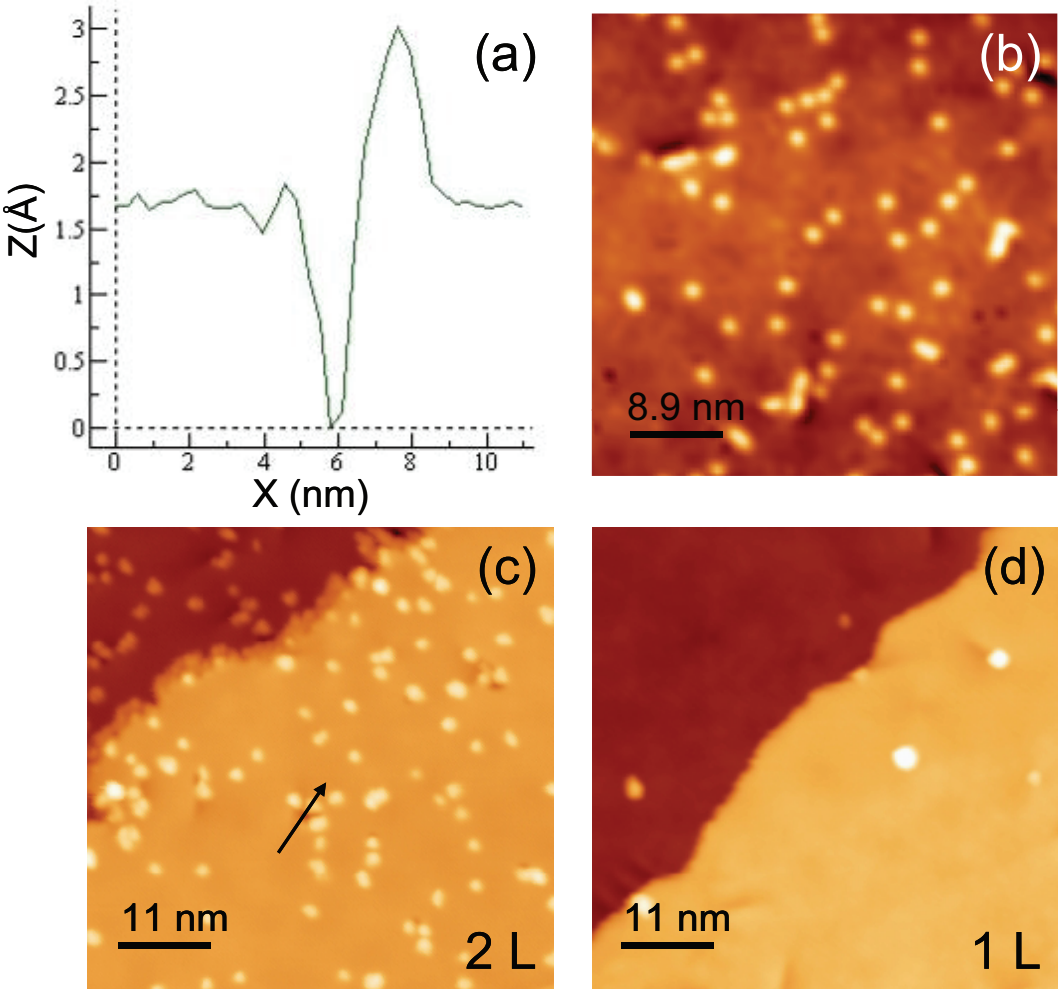

Figure 4.2: (a) Line profile crossing a dip and a cluster in the location indicated by the arrow in (c). (b)(Before oxygen exposure) Substitutional Cs atoms with 0.004 ML coverage on 14 ML Pb film grown on a Si(111)-7×7 surface. V_{sample} = +1.2 V. (c) After 2 L oxygen exposure on a Pb surface with substitutional Cs atoms. (d) After 1 L oxygen exposure on a clean 16 ML Pb film.

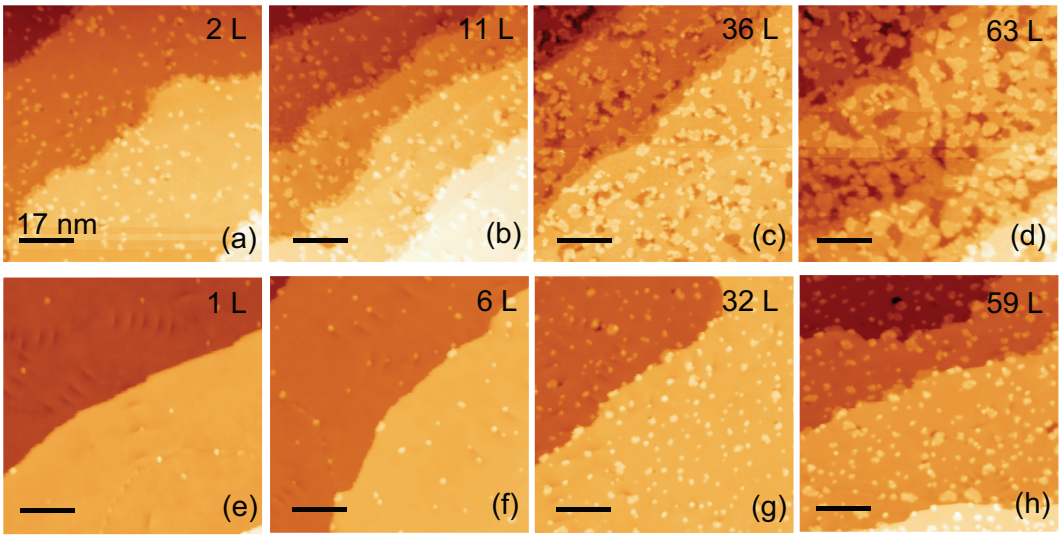

Figure 4.3: Substitutional Cs atom driven enhanced oxidation of Pb surface. (a-d): Pb surface with substitutional Cs atoms after oxygen exposure from 2 L to 63 L. (a) V_{sample} = +1 V; (b) V_{sample} = +2.5 V; (c) V_{sample} = +1.2 V; (d) V_{sample} = +1 V. (e-h): Oxygen exposure of clean 16 ML Pb films on a Si(111)-7×7 surface, 1 L to 59 L. V_{sample} = +1 V. All oxygen exposure was done at a sample temperature of 155 K and all the samples were subsequently annealed to 260 K. All indicated scale bars reference 17 nm.

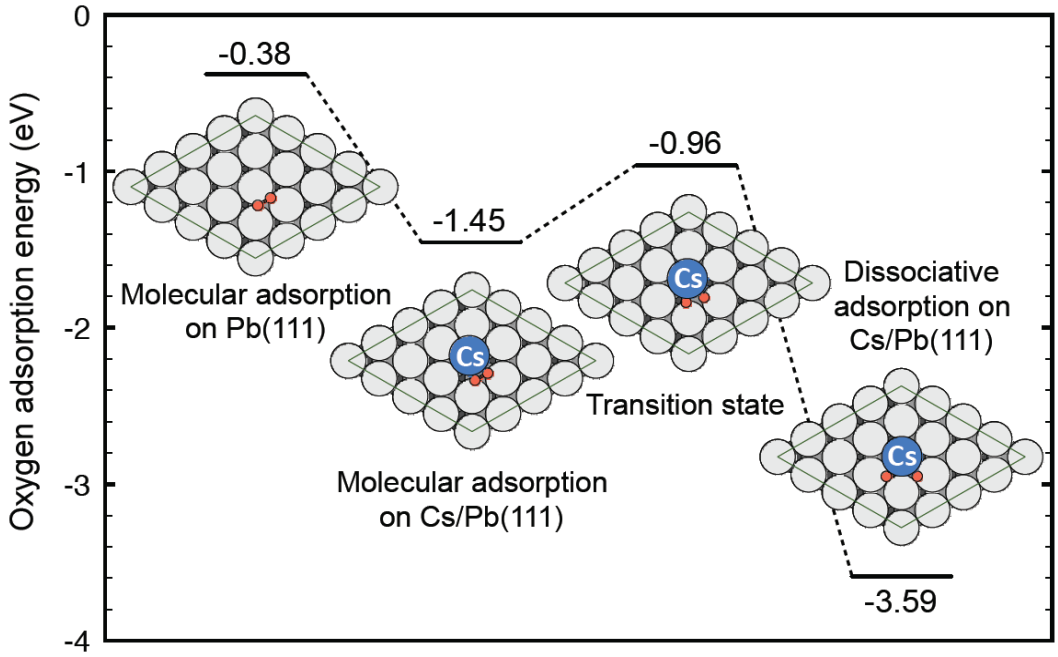

Figure 4.4: Enhanced O_2 adsorption at a Cs substitutional site. The atomic structures and energies of O_2 molecular adsorption on a clean Pb(111) surface, showing molecular adsorption, dissociative adsorption, and the transition state of O_2 dissociation on a substitutional Cs atom. Gray, blue, and red balls represent Pb, Cs, and O atoms, respectively.

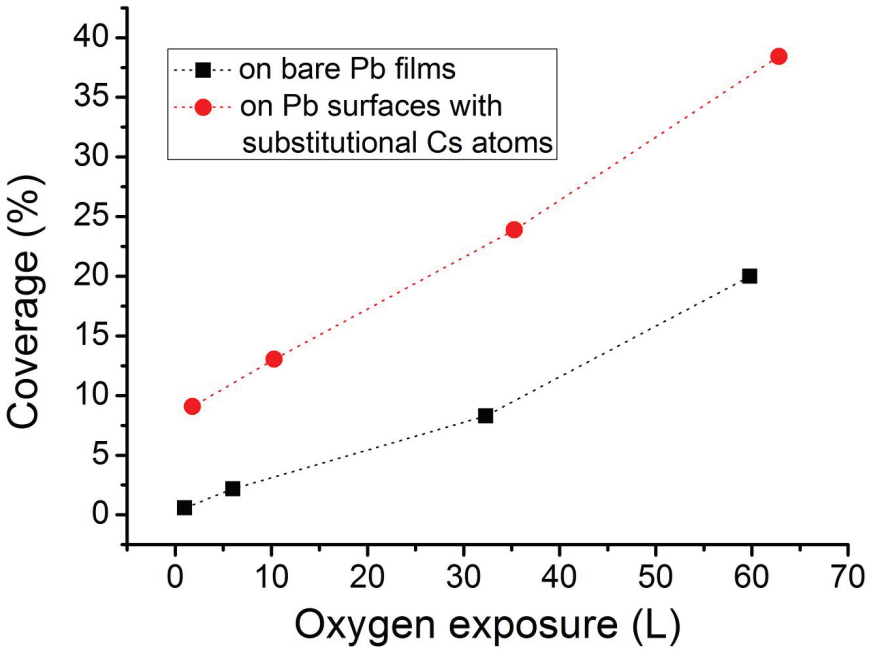

Figure 4.5: Statistical results demonstrating the catalytic role of Cs. Coverage (%) of oxide clusters on bare Pb films (black square), and on Pb surfaces with substitutional Cs atoms (red circle). Every data point is based on a statistical analysis of 16 STM images, 87.4 nm by 97.4 nm each.

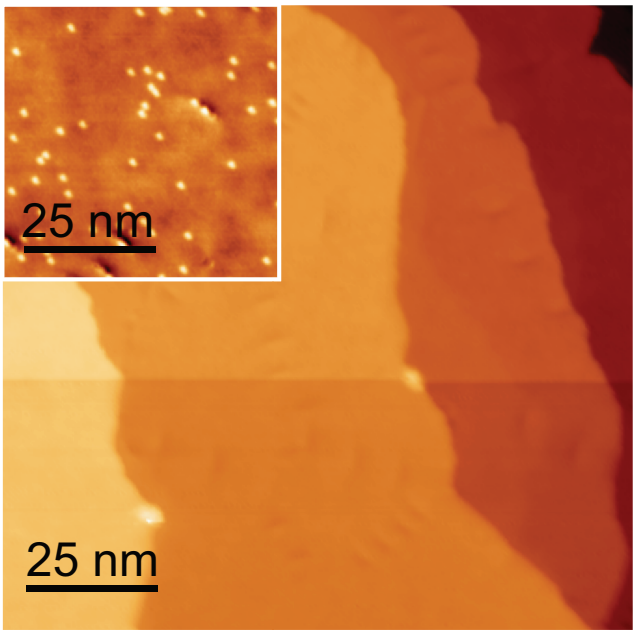

Figure 4.6: Effect of temperature on Pb surface with substitutional Cs atoms. (Inset): Initial Pb surface with 0.0027 ML of Cs, at 155 K, $V_{sample} = +0.7$ V. Same sample after annealing to room temperature. Terraces are clean and only a small number of Cs clusters are found at step edges, $V_{sample} = +1$ V.

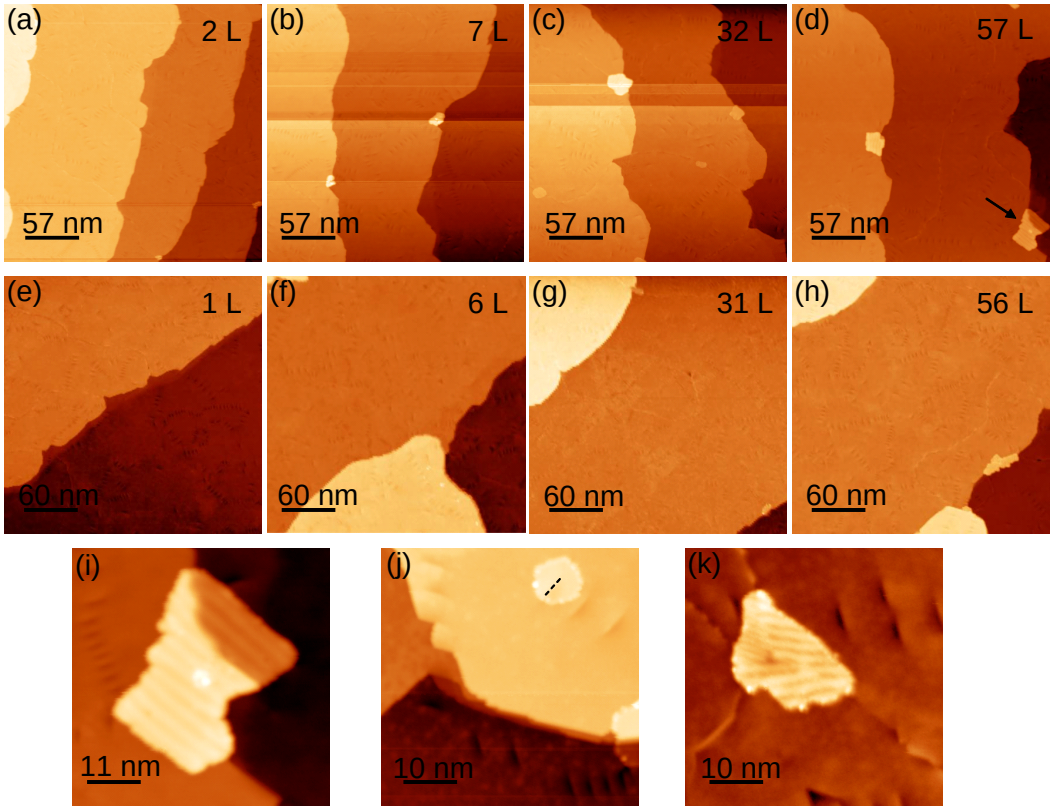

Figure 4.7: Oxidation at room temperature on annealed Pb surface with substitutional Cs atoms after oxygen exposure from 2 L to 57 L (a-d), and on bare Pb surface with oxygen exposure from 1 L to 56 L (e-h). (i) Magnified image of the PbO island marked by an arrow in (d). (j) PbO island after 31 L of oxygen exposure on the bare Pb surface. Underlying defect is marked with a dashed line. (k) PbO island after 56 L on bare Pb surface.

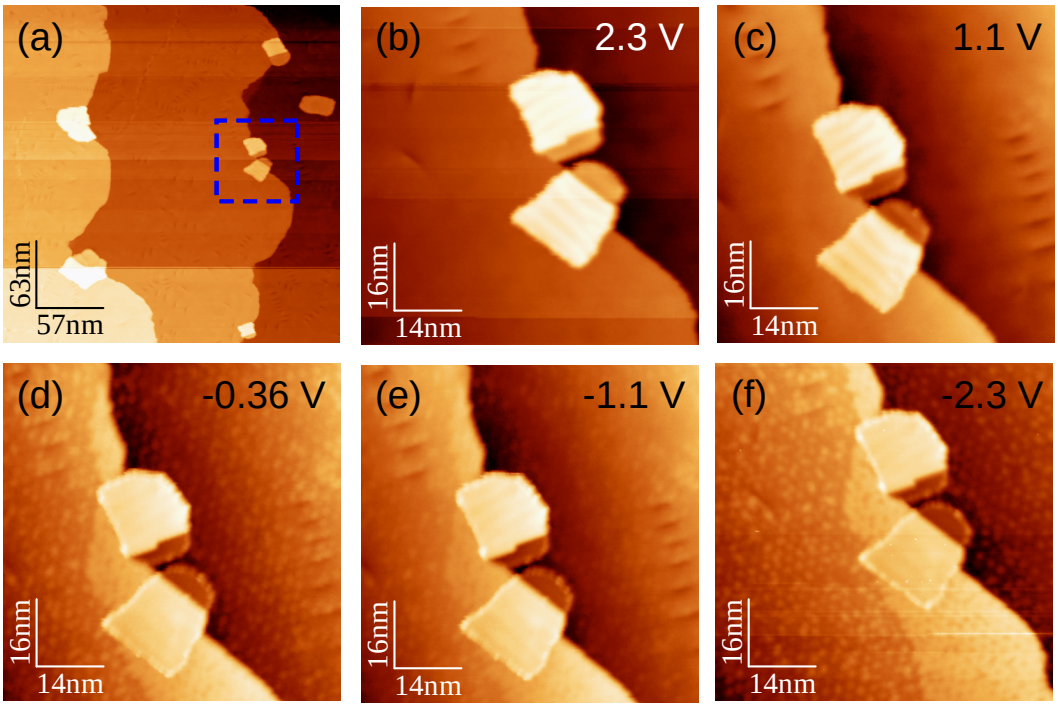

Figure 4.8: (a) Pb surface with substitutional Cs atoms after 57 L of oxygen exposure at RT. Taken on the same sample shown in Fig. 4.7(d). (b-f) Images of PbO patches marked in (a) with a dashed box, at various sample biases from 2.3 V to -2.3 V. Buried Si(111)-7×7 interface is visible in (d-f).

Chapter 5

Reactivity of Pb Surface with Cs Substitutional Atoms: CO Exposure

5.1 Introduction

As discussed in Chapter 4, the reactivity of the Pb surface can be greatly affected by substitutional Cs atoms. Thus, it is intriguing to consider how this Pb surface will react with gases other than oxygen in the presence of Cs atoms. Among various possible choices of gases, CO is a very interesting choice since the CO oxidation reaction has been long studied: investigation of catalysts is motivated by the toxicity of CO and the consequent desire to eliminate CO by converting it to less harmful CO_2 through the oxidation process. The initial reaction between CO and O_2 in the low exposure regime is key to understanding the efficiency of the CO_2 conversion process. In this chapter, the reactivity of CO at Cs substitutional sites is investigated, and also reactivity between CO and O_2 on the Pb surface with Cs atoms. All reactions are studied in the low exposure regime (1 L to 64 L).

5.2 Sample preparation

STM images were taken with PtIr tips and at a temperature of 78 K with a home-built low-temperature UHV-STM at a base pressure $<1.0\times10^{-10}$ torr. N-doped Si(111) with low miscut ($\sim 0.1^{\circ}$) was used in order to grow globally flat Pb films with large terrace size. Cs and oxygen were introduced in the same way as explained in Chapter 4. Gaseous CO was introduced in-situ via a leak valve and its exposure was controlled to be between 1×10^{-7} and 1×10^{-6} torr. The gas line was mounted in such a way that it was possible to introduce O_2 and CO in sequence onto the sample surface in-situ. CO was deposited on Pb films at T = 155 K and annealed to T = 260 K, in the same manner as for O_2 exposure. WSxM software was used for image preparation [34].

5.3 CO exposure

0.0027ML of Cs is deposited on 16 ML Pb films (Fig. 5.1(a)) where substitutional Cs atoms are well isolated on the terrace. Onto this surface, 1.5 L of CO are introduced at 155 K and the sample is subsequently annealed to 260 K after the exposure. The resultant surface is shown in Fig. 5.1(b). In similar manner as for the oxygen exposure (Fig. 4.2(c)), the step edge preferentially reacts with CO to form clusters. However, in the case of CO exposure, the preferential step reaction is not perfect and some part of the step is exposed – no Cs atoms or clusters. Moreover, the terrace is almost clean. Only a few small clusters are found at Pb defect sites but no Cs atoms.

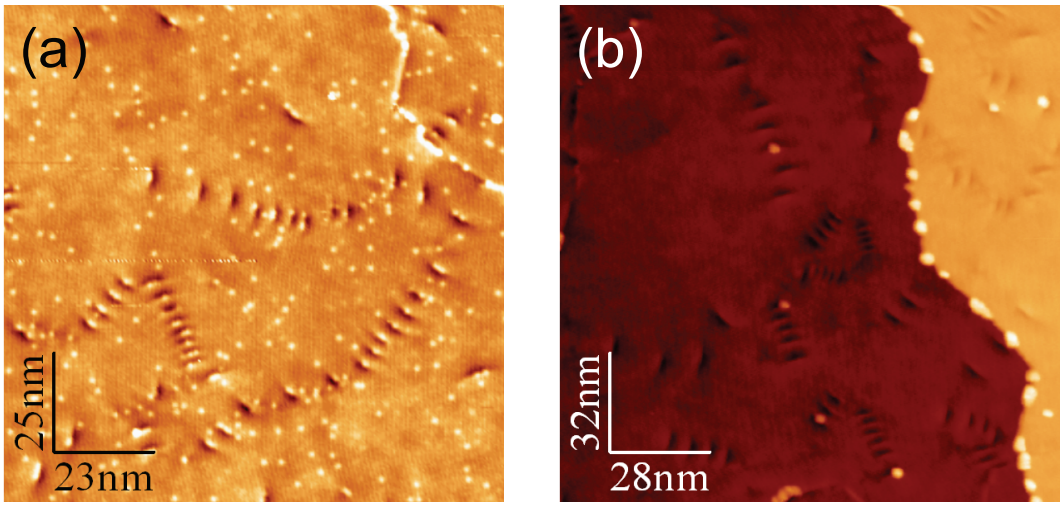

Figure 5.1: (a) (Before CO exposure) Substitutional Cs atoms with 0.0027 ML coverage on 16 ML Pb film grown on a Si(111)-7×7 surface. (b) After initial exposure (1.5 L) of CO onto Pb surface with substitutional Cs atoms.

Interestingly, a significant number of substitutional Cs atoms is removed from the surface during the exposure.

After initial exposure, the same sample is exposed to a higher dose of CO, up to 64 L. All exposure is done with the same procedure: exposure at 155 K and annealing to 260 K. Subsequent CO exposure, however, does not increase the number of clusters nor form larger clusters, as clearly demonstrated in Figs. 5.2(a) – 5.2(d). Note that CO does not react at all with clean Pb surfaces, even at defect sites, which act as nucleation sites for oxidation. Due to the presence of Cs atoms, the nucleation of CO on the Pb surface is greatly enhanced even though substantial numbers of Cs atoms are removed during this reaction. In contrast to oxygen, however, CO does not follow autocatalytic process. CO only reacts with Cs to form clusters during initial CO

exposure: the cluster formation saturates with respect to further exposure.

5.4 CO and O_2 exposure

In order to investigate the reactivity of CO with O_2 on Pb surfaces aided by substitutional Cs atoms, two combinations of sequential exposure are tested: (1) Oxygen exposure on the Pb surface with Cs atoms which is exposed to CO first; (2) CO exposure on the Pb surface with Cs atoms after oxygen exposure.

5.4.1 CO exposure $\rightarrow$ O_2 exposure

Fig. 5.3(a) shows the saturated Pb surface, initially covered with 0.0027 ML Cs, after 64 L of CO exposure. Onto this sample, 1L of O_2 is exposed and the resultant surface is shown in Fig. 5.3(b). At this scale, these two surfaces seem to be almost identical. In the magnified image, Fig. 5.3(d), several tiny clusters (marked with blue circles) appear after additional oxygen exposure. Compared to the clusters formed by CO-Cs binding in Fig. 5.3(c), these clusters are smaller in size and can be found at defect-free sites. Similar clusters (marked with blue circles in Fig. 5.3(e)) are found in the case of 1 L O_2 exposure on clean Pb surfaces without Cs atoms, which suggests that these are oxygen clusters nucleated on the Pb surface after O_2 exposure. However, this oxygen cluster formation takes place independently, regardless of Cs-CO binding clusters, and there is no further inter-reaction between these two cluster types.

5.4.2 O_2 exposure → CO exposure

A new sample with 1 L O_2 exposure is prepared on Pb surfaces with substitutional Cs atoms (Fig. 5.4(a)). The initial Pb surface with Cs atoms is shown in the inset of Fig. 5.4(a). The same sample is exposed to CO gas from 1 L to 50 L according to the same procedure – low temperature exposure followed by annealing to higher temperature. The resultant surfaces are shown in Figs. 5.4(b) – 5.4(d). With further CO exposure the surface remains almost the same even up to 50 L CO exposure. There is a slight change in the cluster size but the chemical nature of this growth cannot be determined by STM alone, since STM is not a technique that is sensitive to a material's composition. Regardless, the result shown in Fig. 5.4 indicates that the functionality of the Cs atom as an effective nucleation site is suppressed after binding to oxygen gas during the initial O_2 exposure; thus, subsequent CO binding hardly occurs.

5.5 Conclusions

The Pb surface with substitutional Cs atoms is exposed to CO gas and O_2 gas in order to investigate the reactivity of CO on the surface and to look for possible CO oxidation. During CO exposure of the Pb surface with substitutional Cs atoms, significant numbers of Cs atoms are removed from their sites and the reaction with CO is saturated after initial CO exposure. However, Cs atoms still act as efficient nucleation sites, resulting in Cs-CO binding clusters preferentially at step edges and defect sites. These are sites

at which CO can hardly nucleate at all in the case of the clean Cs-free Pb surface. Thus, the nucleation rate of CO on Pb surfaces is greatly enhanced by substitutional Cs atoms. Additional O_2 exposure on a CO-exposed sample exhibits oxygen cluster formation which is independent of Cs-CO clusters. When the Pb surface with substitutional Cs atoms is exposed to O_2 first and then to CO, the functionality of Cs atoms as nucleation sites is suppressed, due to the initial reaction with oxygen that forms oxygen clusters. Therefore, additional CO exposure up to 50 L only slightly changes the size of oxygen clusters and further binding of CO to the surface rarely occurs.

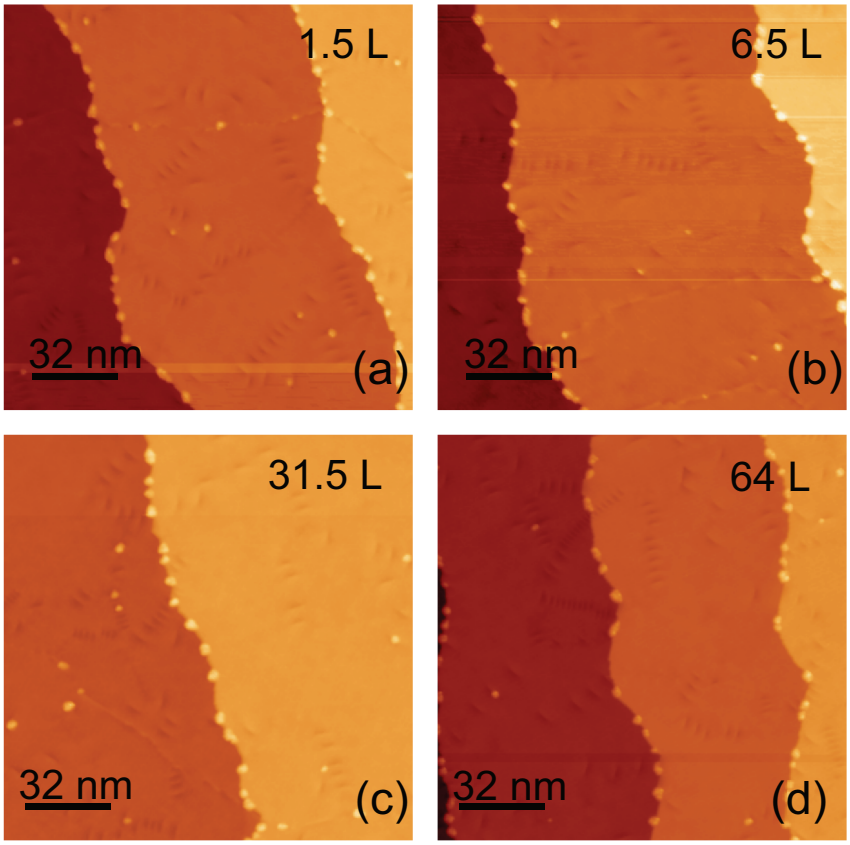

Figure 5.2: CO exposure on Pb surfaces with substitutional Cs atoms. All CO exposure was done at a sample temperature of 155 K and all the samples were subsequently annealed to 260 K. (a) 1.5 L of CO exposure; (b) 6.5 L; (c) 31.5 L ; (d) 64 L. All images taken at $V_{sample} = +1$ V.

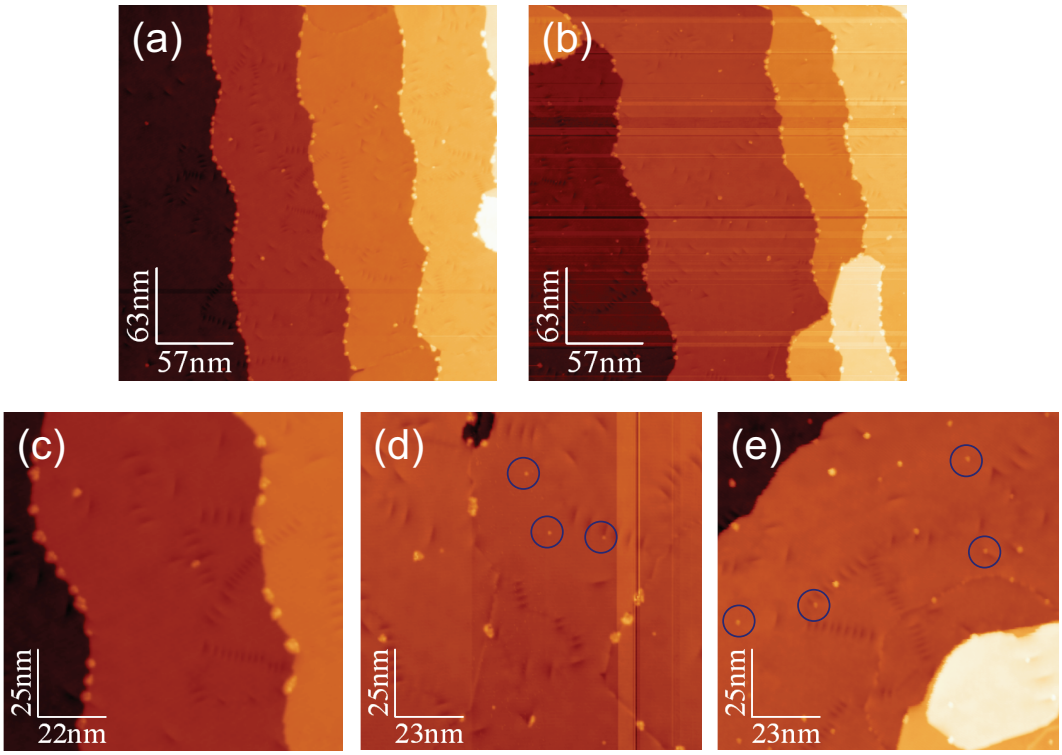

Figure 5.3: (a) Saturated Pb surfaces with initial Cs coverage of 0.0027 ML after 64 L CO exposure. (b) Same sample is exposed to 1 L O_2 at sample temperature of 155 K and annealed to 260 K. (c) Magnified image of (a). (d) Magnified image of (b) showing additional oxygen cluster formation. (e) 1 L oxygen-exposed clean Pb surfaces (no Cs atoms).

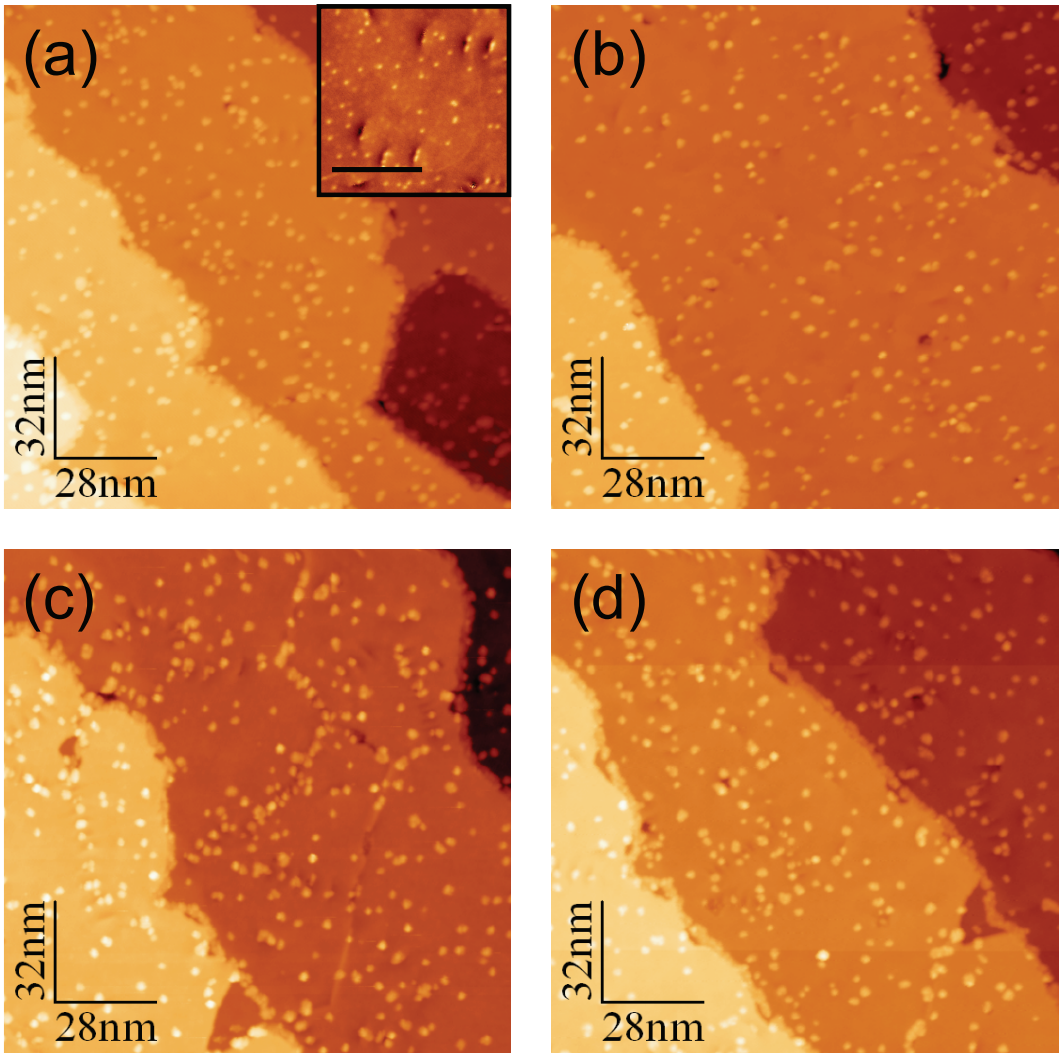

Figure 5.4: (Inset): Initial Pb surface with Cs atoms. (a) After 1 L of O_2 exposure. (b-d) Subsequent CO exposure from 1 L to 50 L. (b) 1 L, (c) 10 L, (d) 50 L. All exposure is done at a sample temperature of 155 K and the sample is annealed to 260 K.

Chapter 6

Electron Coherence in Pb/Ag Thin Metal Heterostructures Epitaxially Grown on Si(111)

Along with other metals, Pb and Ag can form globally flat ultra-thin films on the Si(111) surface. Due to electron confinement along the growth direction, such films exhibit distinctive quantum well states (QWS). Confinement occurs between the vacuum-solid and the solid-solid interfaces. It was reported by Brinkley *et al.*, using angle-resolved photoemission, that quantum confined states existing in Ag thin films can coherently propagate through a Pb overlayer with thickness much thicker than the typical electron mean free path. Here we use scanning tunneling microscopy and spectroscopy (STM/STS) to investigate the quantum well states formed in double quantum wells (Pb quantum well and Ag quantum well) in Pb/Ag/Si(111) double-heterostructures. Both the growth mechanism and the coherent coupling between the Pb and Ag quantum wells will be reported.

6.1 Introduction

As discussed in Chapter 2, the growth and physical properties of metal films deposited on semiconductor substrates can be affected by quantum size

effects (QSE). It has also been shown that metal films grown on metal substrates can exhibit quantum well states (QWS) due to electron confinement by the vacuum barrier and the k-dependent gap of a metal substrate [73–79]. These QWS formed in either metal-semiconductor and metal-metal systems can be clearly detected by scanning tunneling microscopy/spectroscopy (STM/STS).

It is very interesting to investigate a collective electronic behavior of metal-metal-semiconductor heterostructure systems. When double-heterostructures (metal(a)-metal(b)-semiconductor) are fabricated, QWS features on the top metal layer should contain electronic contributions from two individual metal thin films, equivalent to two quantum wells. This collective electronic behavior has, as mentioned above, been investigated using angle-resolved photoemision [80], but has not been studied by STM, which can probe electronic behaviors from a buried interface [28].

Among the various metals, Ag and Pb are desirable choices for the double-heterostructures. Both Ag and Pb can be grown epitaxially on a Si(111) substrate with atomic precision, which allows fine-tuning of each layer′s thickness. Moreover, due to the large anisotropy in the electron′s effective mass for Pb films ($m_{\perp}/m_{\parallel} \ll 1$, see Chapter 2.2.2), electrons can propagate through several monolayers Pb with hardly any scattering. Thus, Pb/Ag/Si(111) double-heterostructures can serve as a template to investigate combined electronic behaviors.

6.2 Sample preparation

All STM images were taken at 78 K with PtIr tips using a home-built low-temperature UHV-STM at a base pressure $<1.0\times10^{-10}$ torr. N-doped Si(111) samples with a low miscut ($\sim 0.1^{\circ}$) were utilized in order to grow globally flat metal films (Ag, Pb) with a large terrace size. Both Pb and Ag were deposited on Si(111)-7×7 from separate thermal evaporators with a typical growth rate of 0.4 ML/min. The Si(111) substrate was kept at $\sim$ 90K during the deposition and annealed to room temperature; in some cases, it was held at room temperature for certain amount of time before being scanned, as specified below. WSxM software was used for image preparation [34].

6.3 Ag thin films on Si(111)

6.3.1 Growth

In the case of Ag growth, there are known challenges: (a) Ag does not wet on semiconducting substrates, and this leads to a rough surface in the first few monolayers of growth; (b) Even if the initial growth layer could be made smooth, the existence of the Schwoebel barrier would cause subsequent deposition to produce rough surfaces [81]. However, these barriers are overcome by a two step method: low temperature growth followed by annealing to room temperature. Using this method, Ag films with various thicknesses can be grown epitaxially. When a small amount Ag is deposited, very thin Ag films of 2-6 monolayers follow the underlying Si(111) steps, and the resultant surface is shown in Fig. 6.1(a). This film is atomically flat over a large

area and has two kinds of holes: one type is 1 ML deep, while the other goes down to the wetting layer [82]. From the line profile (the corresponding line is marked in Fig. 6.1(b)) shown in Fig. 6.1(c), the depth of the hole to the wetting layer can be determined – 3 ML. The growth rate is monitored by a quartz thickness monitor and the thickness of Ag is assigned according to the reading from the thickness monitor. Taking advantage of the STM data for the holes going down to the wetting layer, the calibration by a quartz crystal can be confirmed by checking the depth to the wetting layer and re-adjusted accordingly.

When thicker Ag films ($\geq$ 10) ML are grown, the surface no longer shows holes exposing wetting layers. Flat 10 ML films (Fig. 6.2(a)) exhibit 1 ML high islands and 1 ML deep holes, resulting in a $\pm$1 ML surface roughness. Compared to the surface of 3 ML films (Fig. 6.1(b)), where no defects are observed, that of 10 ML films has a high defect density. These defects are very similar to the ones observed in the Pb/Si(111) system, where they are explained as multiple dislocations with subsurface components producing an off-axis stacking fault along a close-packed plane [72].

In order to fine-tune the thickness of Ag films with precision, a multiple growth mechanism is studied. Initial 10 ML Ag films with a $\pm$1 ML surface roughness are shown in Figs. 6.3(a) and 6.3(b). On these samples an additional 10 ML of Ag is deposited by the same two step method and the resultant images are Figs. 6.3(c) and 6.3(d). The films still maintain the original flat morphology with mostly a $\pm$1 ML roughness, but the overall size of islands

is increased, and 2-3 ML islands and holes start to appear: one of the 3 ML islands is marked with a blue circle in Fig. 6.3(d). When one more growth cycle is applied to the same sample, the now 30 ML Ag films show even bigger islands (holes) ranging from 1 – 4 ML in height (depth): a 4 ML island is marked with a blue circle as an example in Fig. 6.3(f). This result suggests that every additional growth cycle will increase the surface roughness, and that the flat morphology will be ruined after several cycles. We find that this highly undesirable result can be avoided by additional annealing at room temperature. 30 ML Ag films after 3 growth cycles (Fig. 6.3(e)) are re-annealed to room temperature and kept at RT for 4.5 hours and then the surface is examined again (Figs. 6.4(a) – 6.4(b)). There are still several 2 ML islands on the surface, but no 3-4 ML ones observed. When the same sample is annealed even longer, 12 hours, the surface almost recovers its initial ± 1 ML roughness; only a few 1 ML islands with the second layer are observed, as shown in 6.4(c) – 6.4(d). Therefore, atomically flat Ag films can be prepared, ranging from 2 ML to any desirable thickness, by applying a two step growth cycle repeatedly.

6.3.2 Electronic structure

The electronic structure of Ag thin films grown on a Si(111)-7×7 surface can be probed by STS. Figs. 6.5(b) – 6.5(c) show the dI/dV spectra taken on 25 ML Ag films at the marked position, away from any defect site (Fig. 6.5(a)). These spectra clearly exhibit the surface state and 3 quantum well states. The

surface state observed on Ag(111) is a Shockley-type surface state, found in the band gap of surface-projected bulk band structures of noble metals with (111) faces, as discovered in Cu(111) by Gartland and Slagsvod [83]. Note that the surface state observed here is located right above the Fermi level, in contrast to the ideal Ag(111) surface where the surface state is right below the Fermi level [84]. This has been explained as being due to the shift of the lower band edge $L_2^{'}$ induced by tensile strains in Ag film grown on lattice-mismatched Si(111) substrate [85]. In addition, it should be observed that QWS of Ag films can only be detected in the filled states (negative sample bias) since the L band gap of Ag(111) extends up to 3.9 eV above E_F and the lower band edge $L_2^{'}$ is at 0.3 eV below E_F. This is the reason that in the empty states (positive sample bias) in Fig. 6.5(b) no features are observed besides the dominant surface state while 3 QWS are found in the filled states in Fig. 6.5(c).

Due to the surface state in Ag films, the quantum interference of surface state electrons can be observed [86]. Fig. 6.6 shows difference conductance images taken at various biases near the surface state position and the corresponding topographic image of a 25 ML Ag film. In these conductance images, interference patterns of electron standing waves appear around steps and defects on the surface. Since the energy of surface state electrons changes as the sample bias changes, the spacing between these fringes decreases as the energy increases. From this information E vs. k can be mapped for the surface state.

A few additional observations deserve to be made regarding the elec-

tronic structure of Ag films. Fig. 6.7 shows 25 ML Ag film morphology and its conductance image taken at 2 V. Interestingly, the edge of every island and hole has clear contrast in the conductance image. This clear edge contrast was not observed for Pb films grown on Si(111) substrates, but for Ag it can be found at almost all sample biases, with the contrast clearer in positive biases than negative biases. Even in the interference data (Figs. 6.6(b – f)) the bright edges of steps are noticeable: indeed, at biases at which quantum interference effects are less significant, bright contrast of edges is the dominant feature of the conductance images (Fig. 6.7). This sharp edge contrast suggests the existence of edge states.

The influence of defects is also worth noting, since Ag films have a high defect density. Four spectra, shown in Fig. 6.8(c), are taken at the defect site and further away from it as marked in Fig. 6.8(b) from 1 to 4. Overall, all spectra shows the surface state and 3 QWS with similar peak positions but there are an intensity modulation near the surface state: the intensity modulation is strong right at the defect site, becomes weaker, and finally recovers Ag surface′s original unperturbed spectra as moves further away from the defect.

6.4 Multi-layer growth of a heterostructure – $(Pb/Ag)_2$ on Si(111)

After Ag films are successfully grown and investigated, Pb films are grown with the same method – low temperature deposition and annealing to

room temperature. Fig. 6.9(a) shows initial 20 ML Ag film and Fig. 6.9(b) shows the surface morphology after additional 20 ML Pb deposition. The resultant surface gets much smoother: deposited Pb atoms fill up 1 ML deep holes in the Ag films and make flat films. Extra Pb atoms form larger 1 ML islands by combining adjacent islands in the underlying Ag. Thus, the additional Pb deposition forms epitaxially flat films, and by doing so it improves the surface roughness, which makes a better template for a next growth of a Ag overlayer.

The Pb films grown on Ag/Si(111) also form QWS which can be detected by STS. Due to the smoothening process, the thickness of Pb films can differ by 1 ML even on the same terrace. Thus, if one looks only at the topographic image it is hard to distinguish where Pb thicknesses are different. Aided by differential conductance images taken at two different biases, however, this problem can be solved, since every other layer shows opposite contrast due to the half integer matching (Chapter 2.2). Fig. 6.10(a) is the topographic image of Pb films grown on Ag/Si(111), which looks like a simple structure. However, the conductance images taken at the sample biases of 2 V and 1 V reveal that it is rather a complicated structure and spectra should be taken for a correct thickness assignment of the system. Spectra taken on areas showing different contrast in the conductance images – A, B and C – indeed show different QWS features (Fig. 6.10(b)). Note that even though the top Pb surface has fewer defects, underlying Ag defects can be imaged in the conductance images. From theses spectra, the thickness of Pb can be deter-

mined. In the study done by Becker and Berndt on Pb films grown on *single crystal* Ag(111), both calculated and measured QWS locations are reported [79]. Essentially, Ag thin films grown on Si(111) are the same as single crystal Ag(111) in terms of the effect to a Pb overlayer′s QWS if only positive biases are considered: due to the L gap located from 0.3 eV below E_F to 3.9 eV above E_F in Ag, electrons in Pb thin films only see this L gap in both systems, with no additional electronic contribution from Ag films in positive biases. Therefore, the Pb film thickness can be determined by comparing measured QWS in Fig. 6.10(b) to reported values in ref. [79] and assigned accordingly: A = 17 ML, B = 18 ML, and C = 19 ML. Here the thickness is counted including a wetting layer.

The multi-layer heterostructure $(Pb/Ag)_2$ on Si(111) is completed with a sequential growth of 20 ML Ag and 20 ML Pb on Pb/Ag/Si(111), and the resultant surfaces are shown in Fig. 6.11. The surfaces still retain their global flatness (no evidence of huge 3D island formation) but the topmost layer looks more like a network of islands than one smooth surface. Even though the surface gets complicated after multiple growth cycles, Pb deposition still fills the gaps in the Ag films and smoothens the surface (Fig. 6.11(d)), which suggests the possibility of successful muti-layer growth beyond $(Pb/Ag)_2$.

After the growth and characterization of multi-layer $(Pb/Ag)_2$, the sample is transferred to a separate growth chamber using the transfer system described in Chapter 1.2.3. During transfer, the sample is kept under UHV with a base pressure on the order of $\sim 10^{-9}$ torr and then capped with

2 nm thick amorphous Ge at low temperature ($\sim$ 100 K), which is evaporated from a Knudsen cell. Ge capping is done in order to protect epitaxial films for ex-situ fabrication and characterization. As a first step toward further analysis, STEM and TEM images are taken by our collaborators and an interesting super-structure formation is suggested. However, the origin of the super-structure and its formation mechanism can not be discussed at the moment and more detailed studies are required.

6.5 Electron coherence in Pb/Ag thin films grown on Si(111)

For the investigation of collective electronic behavior in Pb/Ag/Si(111) heterostructures, 25 ML of Ag is deposited on Si(111)-7×7 and nice flat films are formed (the same sample shown in Fig. 6.5). In order to observe the electronic influence of underlying Ag films, Pb films can not be too thick. Therefore, a small amount of Pb is deposited to prepare thin Pb overlayers. The resultant surface, shown in Fig. 6.12(a), consists of layers of different islands with a flat-top. Even though the resultant surface is not flat but a mixture of different islands, dI/dV spectra aided by differential conductance images can distinguish each layer′s thickness. Note that only QWS peaks in empty states (positive sample biases) are compared to the values from ref. [79] for the thickness assignment, since QWS features in empty states are not affected by the Ag quantum well due to the L gap (Chapter 6.3.2). In Figs. 6.12(b – c), areas showing 3-6 ML are marked accordingly.

In filled states (negative sample biases), the Pb overlayer's QWS features can be influenced by underlying Ag films′ QWS. Figs. 6.13(d – e) show the Pb overlayer's dI/dV spectra taken on 5 and 6 ML. For comparison, the initial Ag on Si(111) spectra are shown in Figs. 6.13(a – b). Figs. 6.13(g – h) show the reference spectra of Pb thin films grown on the SIC phase prepared on Si(111)-7×7 (Chapter 2.2.1.1). When the QWS peaks observed in ref. [79] are compared to the QWS of Pb thin films grown on Si(111)-7×7 (Fig. 3.3(e)), and if 1 ML is added to the Pb films′ thickness, the QWS locations in both cases are almost the same. The 1 ML addition is necessary for correct comparison because, historically, the thickness of Pb grown on Si(111) has been counted *excluding* a wetting layer (1 ML), while here the thickness on Ag(111) is counted *including* a wetting layer. Therefore, 4 ML Pb/SIC-Si(111) can be considered as a reference spectrum for 5 ML Pb/Ag/Si(111), and 5 ML Pb/SIC-Si(111) is a reference spectrum for 6 ML Pb/SIC-Si(111). Figs. 6.13(c,f,i) show schematics of the system.

The first noticeable difference in the Pb overlayer′s spectra is a disappearance of the Ag films′ surface state. In the case of 5 ML (Fig. 6.13(d)), there is a main peak around 0.4 eV where the pure Pb film′s QWS is located (marked with a green arrow), but it is slightly shifted toward a lower bias. Compared to Ag film′s QWS (Fig. 6.13(a)), the contribution from Q1 seems overshadowed by the Pb film′s QWS; there is a small peak where Q2 is located, but this is also shifted. The same tendency is seen in the 6 ML Pb overlayer case (Fig. 6.13(e)): the main peak originates from the Pb film′s QWS with

a small shift, combined with a contribution from the Q2 peak. Also a small bump appears at the Q1 peak position, with a small shift. Thus, the Pb overlayer shows spectra consisting of combined features from Ag film′s QWS and Pb film′s QWS, with a small shift.

The spectra taken on a 3 ML Pb overlayer can be interpreted with the same argument (Fig. 6.14). The reference spectrum (Fig. 6.14(c)) for the Pb overlayer is taken from ref. [16]. Here, 2 ML Pb films are grown on a mixture of $\sqrt{3} \times \sqrt{3}$ and $\sqrt{3} \times \sqrt{7}$, and are equivalent to the 3 ML Pb overlayer on Ag/Si(111). In this case, the Pb film′s QWS sits right in between Ag film′s QWS (Q1 and Q2), resulting in one broad feature in the spectra as shown in Fig. 6.14(b). Moreover, a shifted Q3 is visible. Thus, the coherent coupling of electrons in this heterostructure, Pb/Ag/Si(111), is qualitatively confirmed by STS measurements.

6.6 Conclusions

In this chapter, the growth mechanism of Ag thin films on Si(111)-7×7 and multi-layer heterostructures, $(Pb/Ag)_2$/Si(111)-7×7 are discussed, as well as the coherent coupling in double-heterosturctures, Pb/Ag/Si(111)-7×7. It is demonstrated that atomically flat Ag films with any desirable thickness can be grown by applying a two step growth cycle repeatedly. In addition, such Ag films have electronic structures identical to single crystal Ag(111) in the empty states due to the presence of the L gap, but show distinctive surface states right above E_F and also show QWS in the filled states. Intensity modulations

near defect sites are observed and a possibility of edge states is suggested. In $(Pb/Ag)_2/Si(111)$-7×7 growth, the resultant surface retains its global flatness without any evidence of huge 3D island formation; this flatness is aided by the smoothening process during the Pb layer growth. Finally, dI/dV spectra measurement reveals the electron coherence in the Pb/Ag/Si(111) system. Collective electronic features are observed due to the contributions from both the Pb overlayer and the buried Ag film: the resultant spectrum of the top Pb layer shows peaks originating from both Pb and Ag films′ QWS, with a small shift.

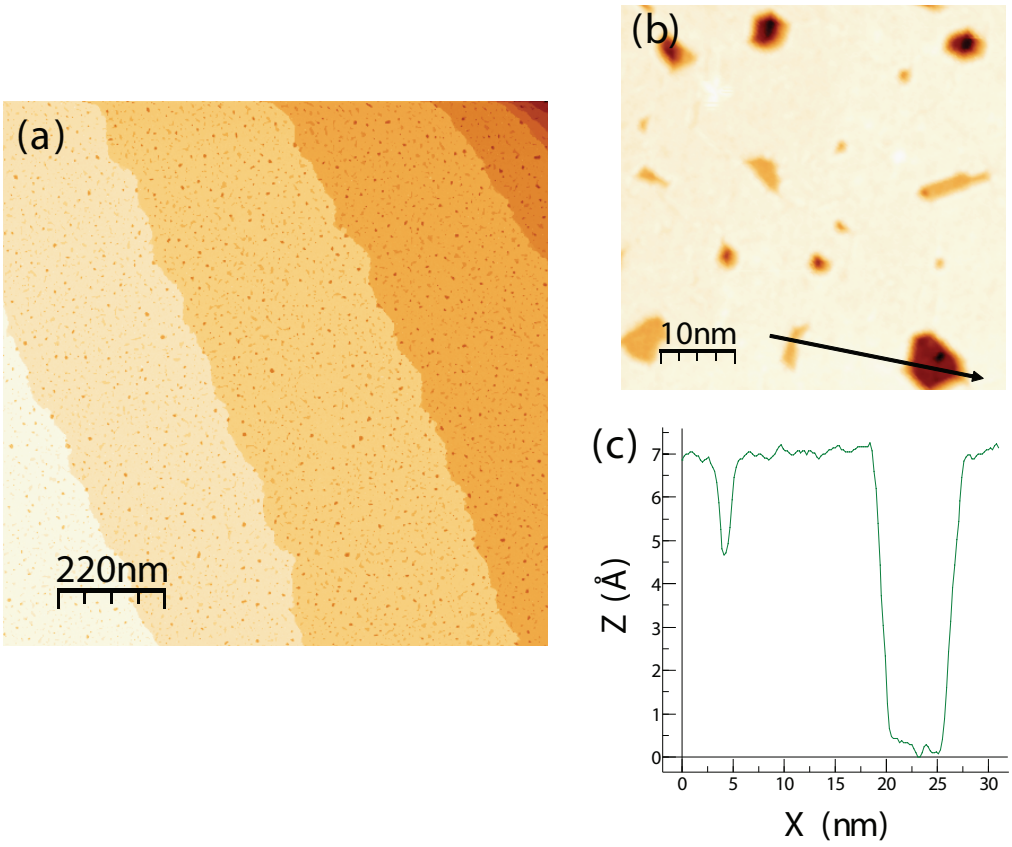

Figure 6.1: (a) Atomically flat 3 ML Ag thin films grown on Si(111)-7×7 surface. (b) Magnified image showing holes with two different depth: 1 ML deep, and 3 ML deep (exposing the wetting layer). (c) Line profile across the 2 types of holes shown in (b).

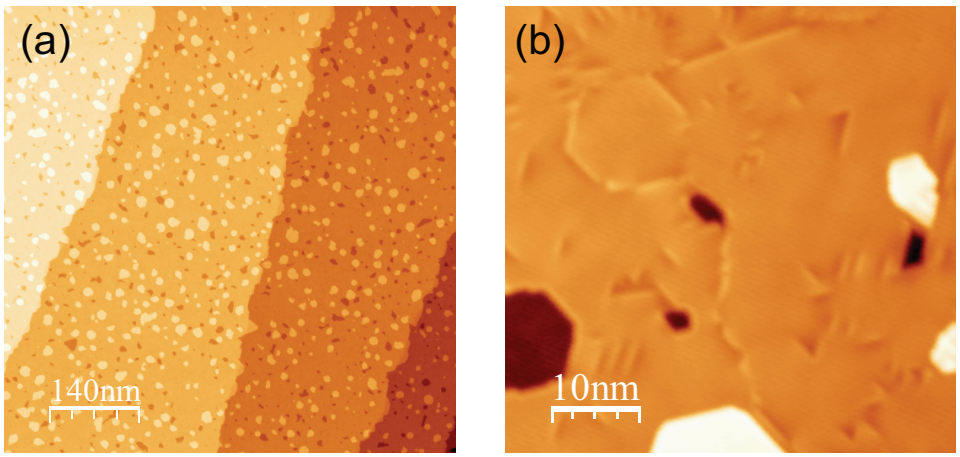

Figure 6.2: (a) Atomically flat 10 ML Ag thin films grown on Si(111)-7×7 surface with a ±1 ML surface roughness. (b) Magnified image shows a high density of defects caused by stacking faults.

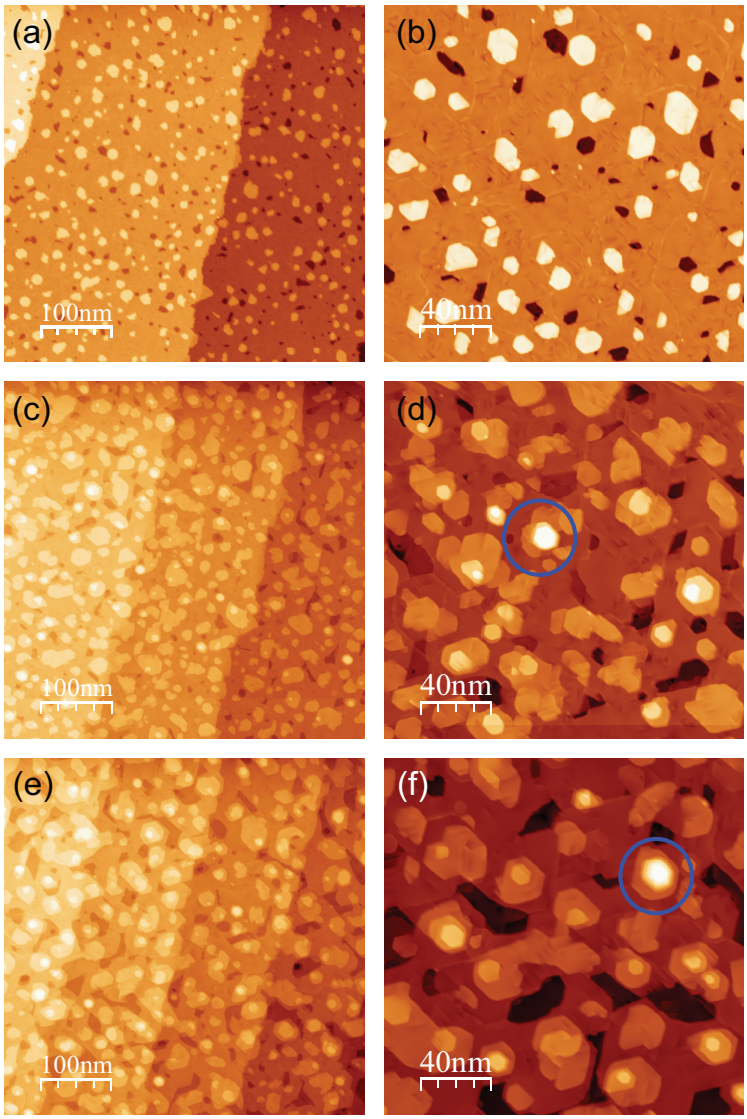

Figure 6.3: (a – b) After first growth cycle: initial 10 ML Ag films. (c – d) After second growth cycle: additional 10 ML deposition with a same two step method used in (a). (e – f) After third growth cycle, resulting in 30 ML Ag films. Blue circle marks one 3 ML and 4 ML islands on the surfaces of (d) and (f), respectively.

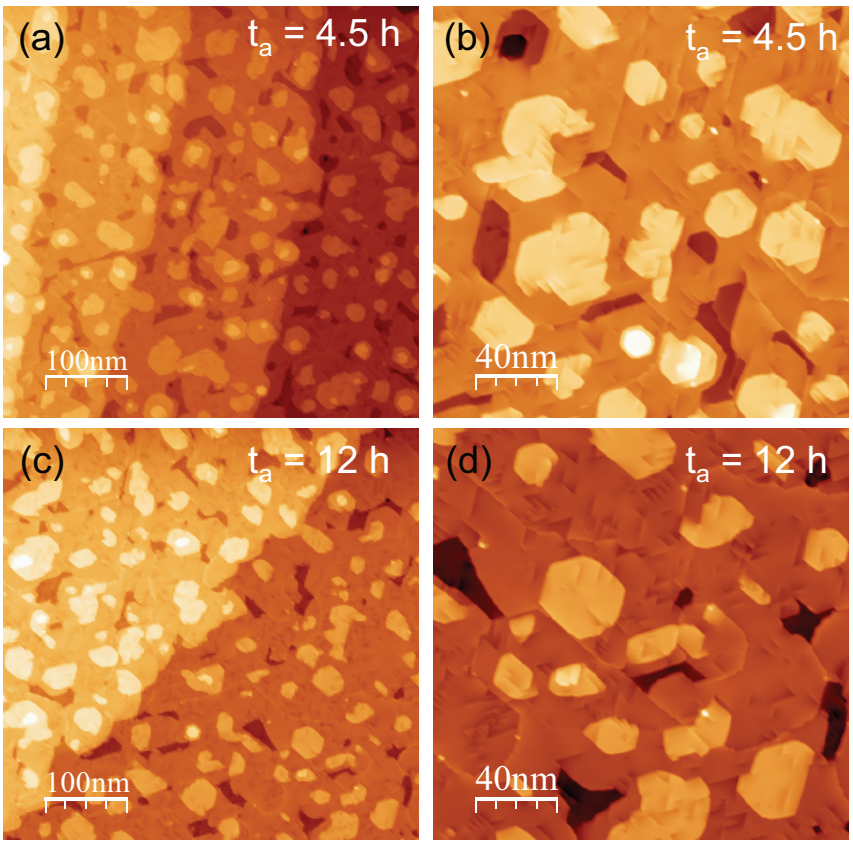

Figure 6.4: (a – b) 30 ML Ag films grown by 3 growth cycles are annealed to RT and kept for 4.5 hours. The surface gets smoother during the annealing process, eliminating 3-4 ML islands. (c – d) Additional 12 hour annealing at RT of the same samples almost recovers original ±1 ML roughness.

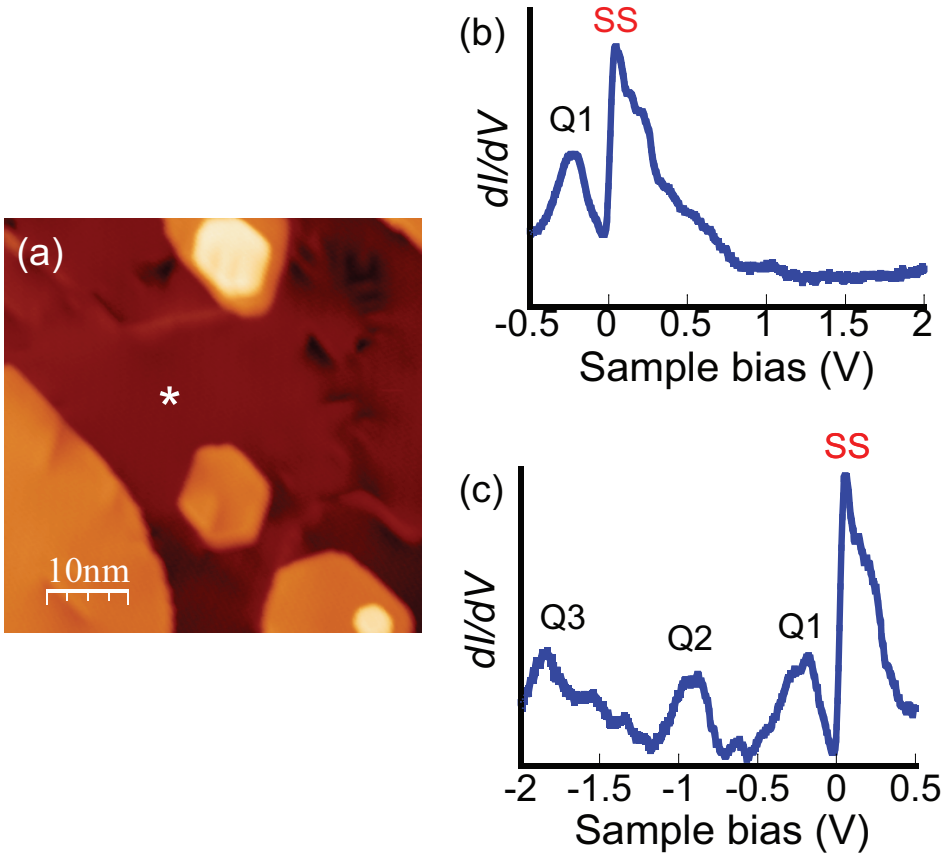

Figure 6.5: (a) 25 ML Ag films grown on Si(111)-7×7. (b – c) Spectra taken at the position marked in (a). A surface state and 3 QWS of Ag films are clearly observed.

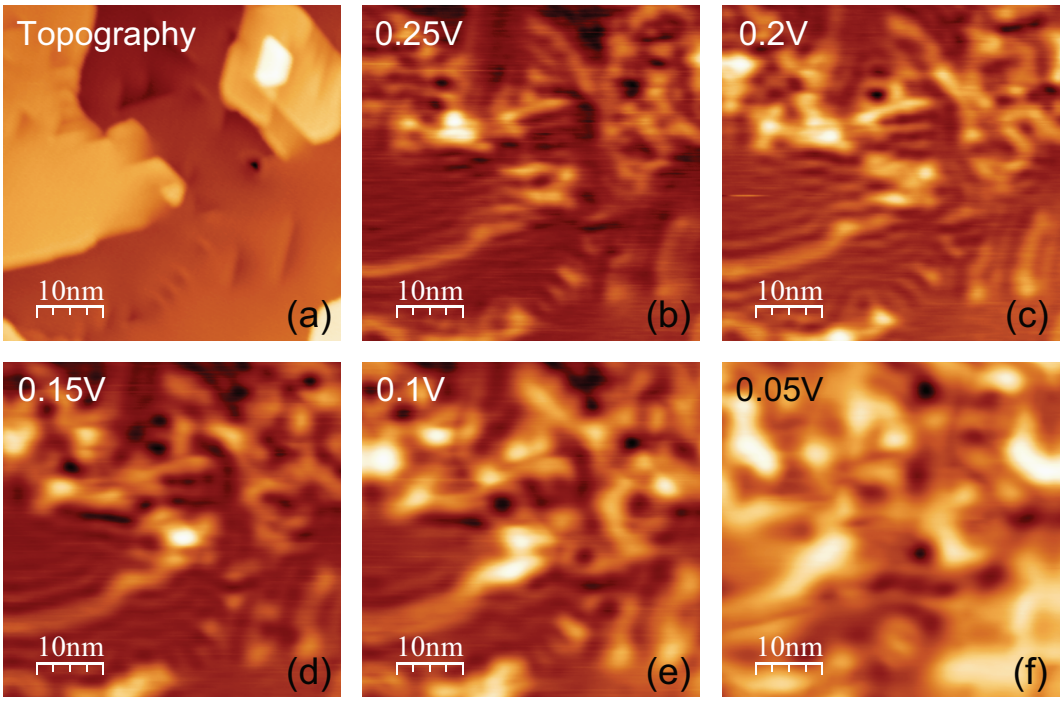

Figure 6.6: (a) Topographic image of 25 ML Ag films. (b-f) Differential conductance images taken at sample biases near the surface state position. Standing wave formation and interference around step edges and defects are visible.

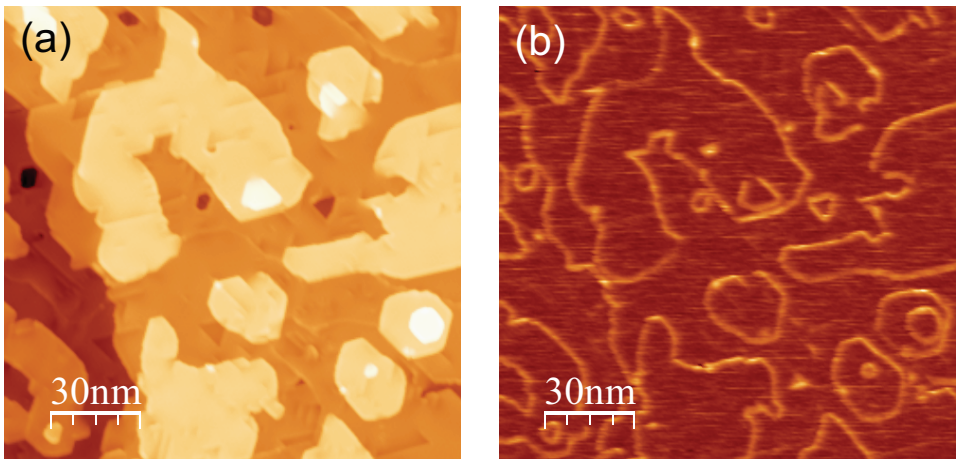

Figure 6.7: (a) 25 ML Ag film. (b) Differential conductance image taken simultaneously with (a) at the sample bias, $V_{sample} = 2$V. All edges of steps and holes show clear contrast.

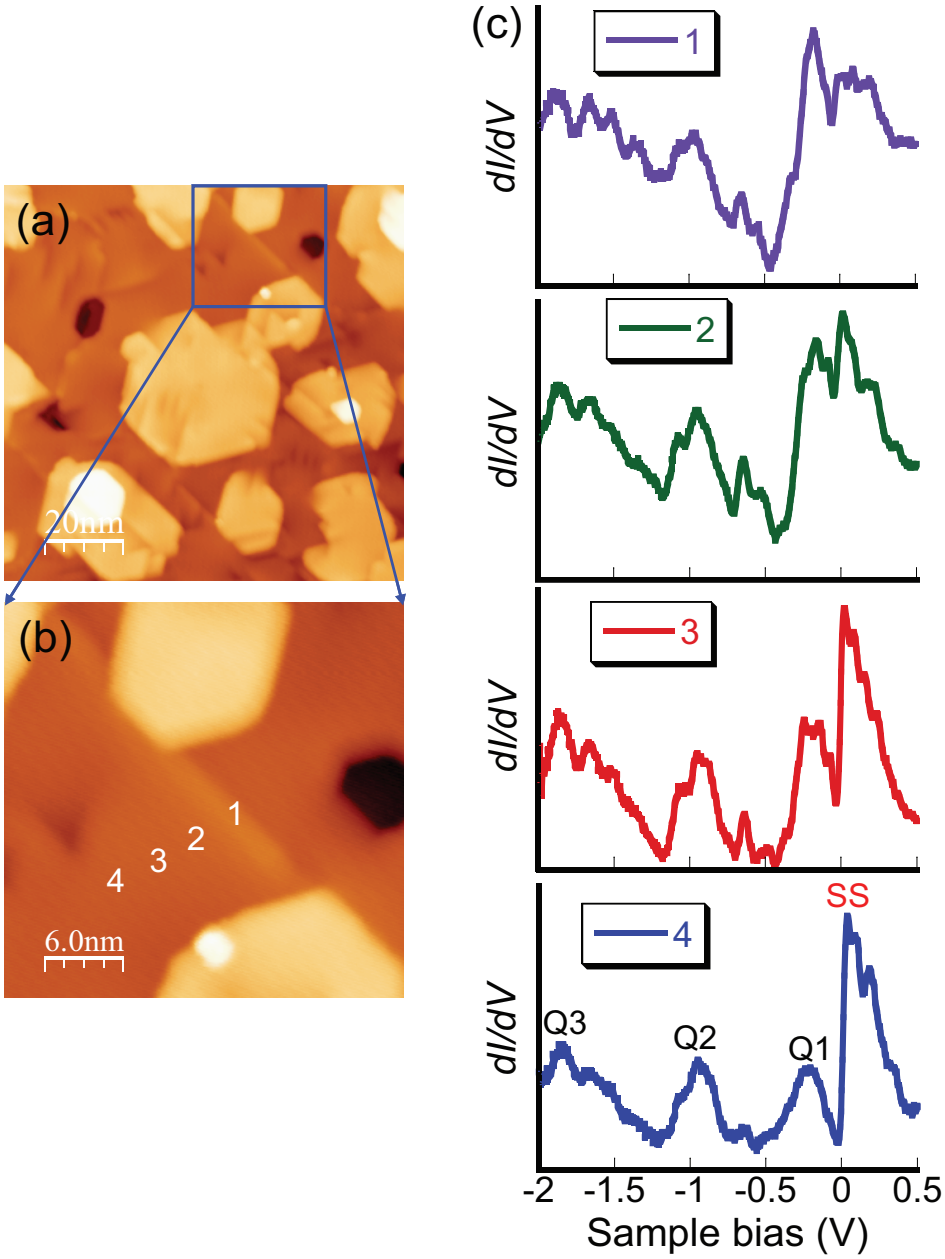

Figure 6.8: (a – b) 25 ML Ag film. (b) Spectra taken at the positions marked in (b) from 1 to 4. Intensity modulation is observed near the surface state when spectra are taken near the defect site.

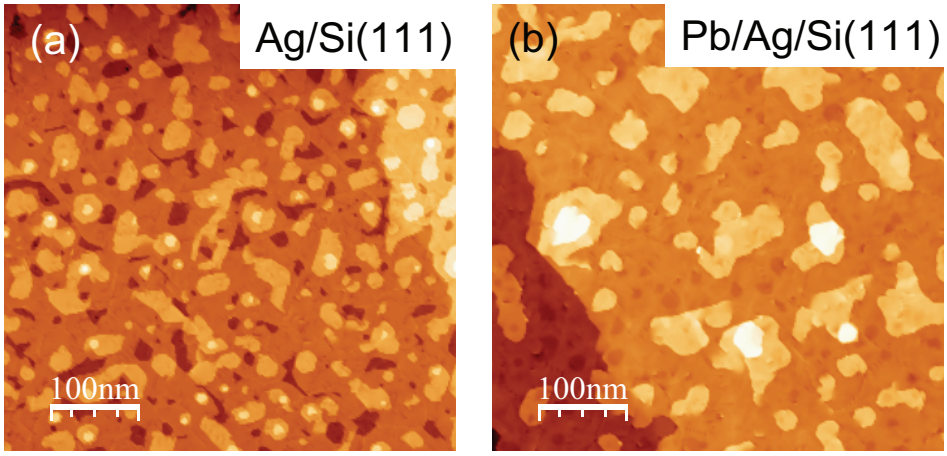

Figure 6.9: (a) Initial 20 ML Ag film grown on Si(111)-7×7. (b) After additional 20 ML Pb deposition on (a). The surface gets smoother by filling the holes in the initial Ag film and forming larger islands.

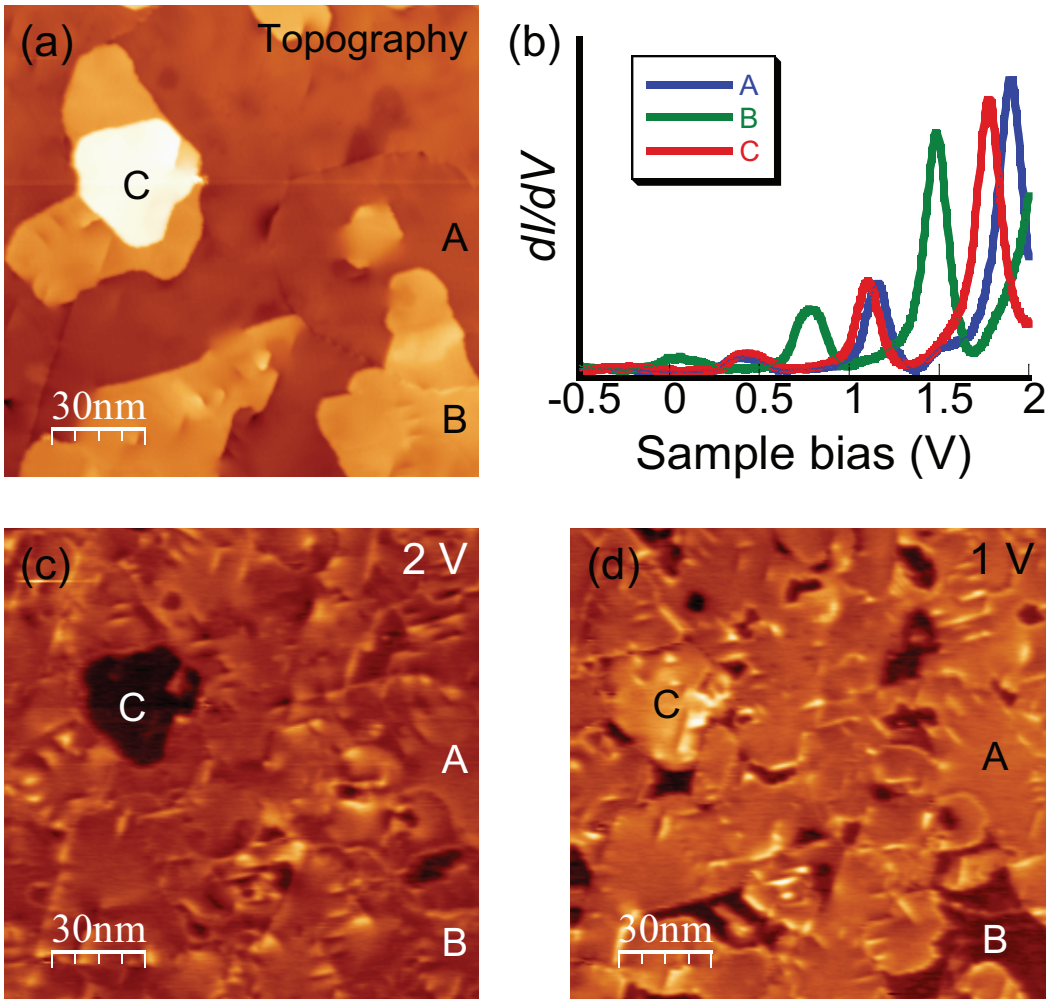

Figure 6.10: (a) The topographic image of Pb films grown on Ag/Si(111). (b)dI/dV spectra taken on three locations marked A through C in (c). (c – d) Differential conductance images taken at the sample bias of 2 V and 1 V, exhibiting a different contrast originated from different Pb thicknesses.

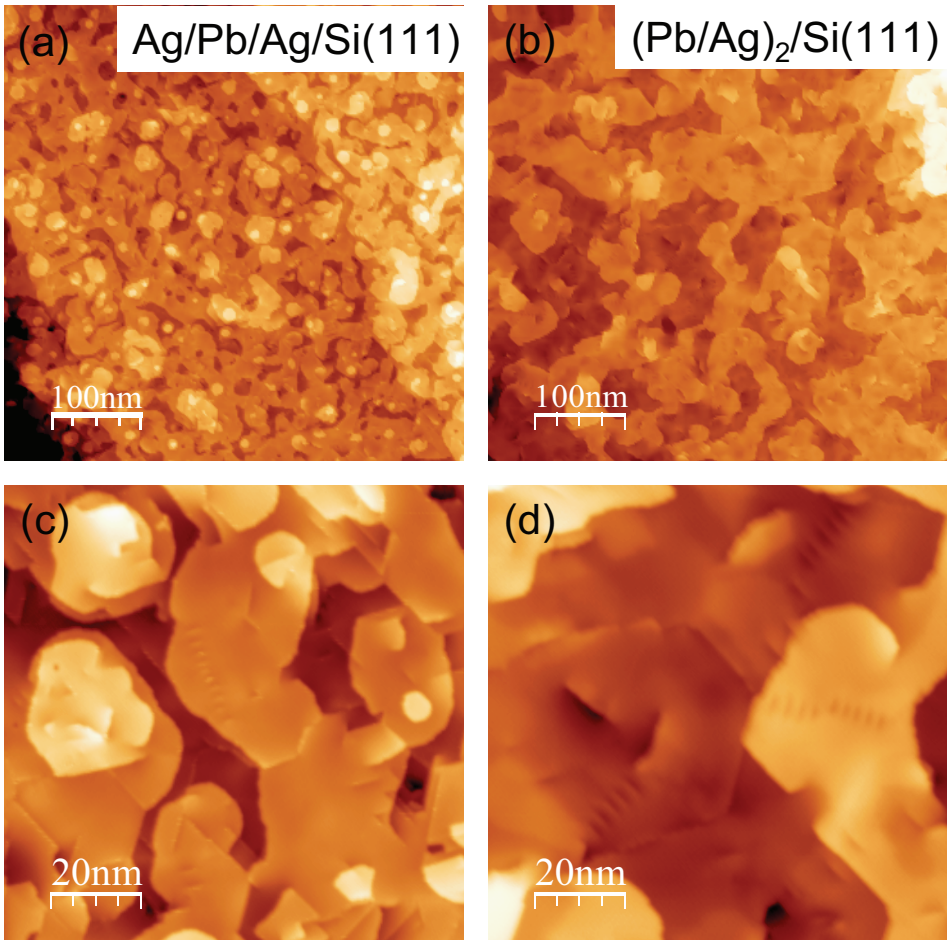

Figure 6.11: (a) The topographic image of Ag films grown on Pb/Ag/Si(111). (b) The resultant surface after the completion of $(Pb/Ag)_2$ multi-layer. (c – d) Magnified images of (a) and (b) respectively.

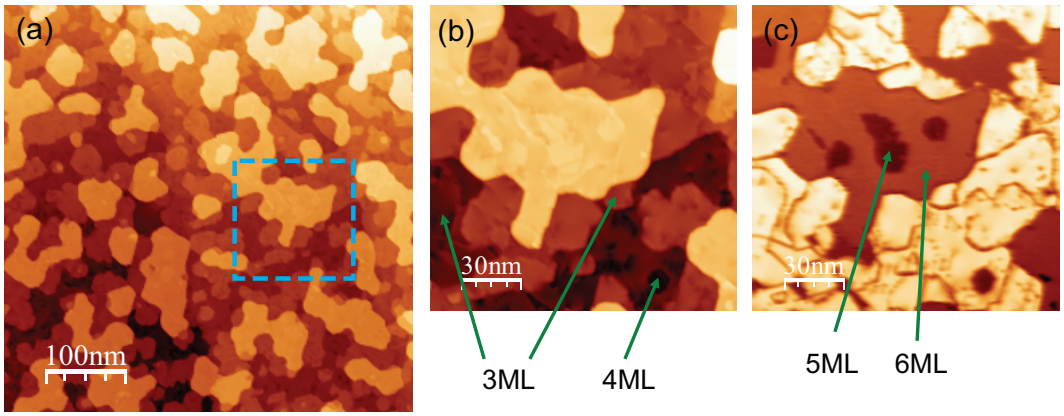

Figure 6.12: (a) Small amount ($\sim$ 5 ML) Pb is deposited and formed layers of islands. (b) Magnified image of the area makred in (a). (c) Differential conductance image taken at the same time with (b). Assigned Pb thicknesses are marked.

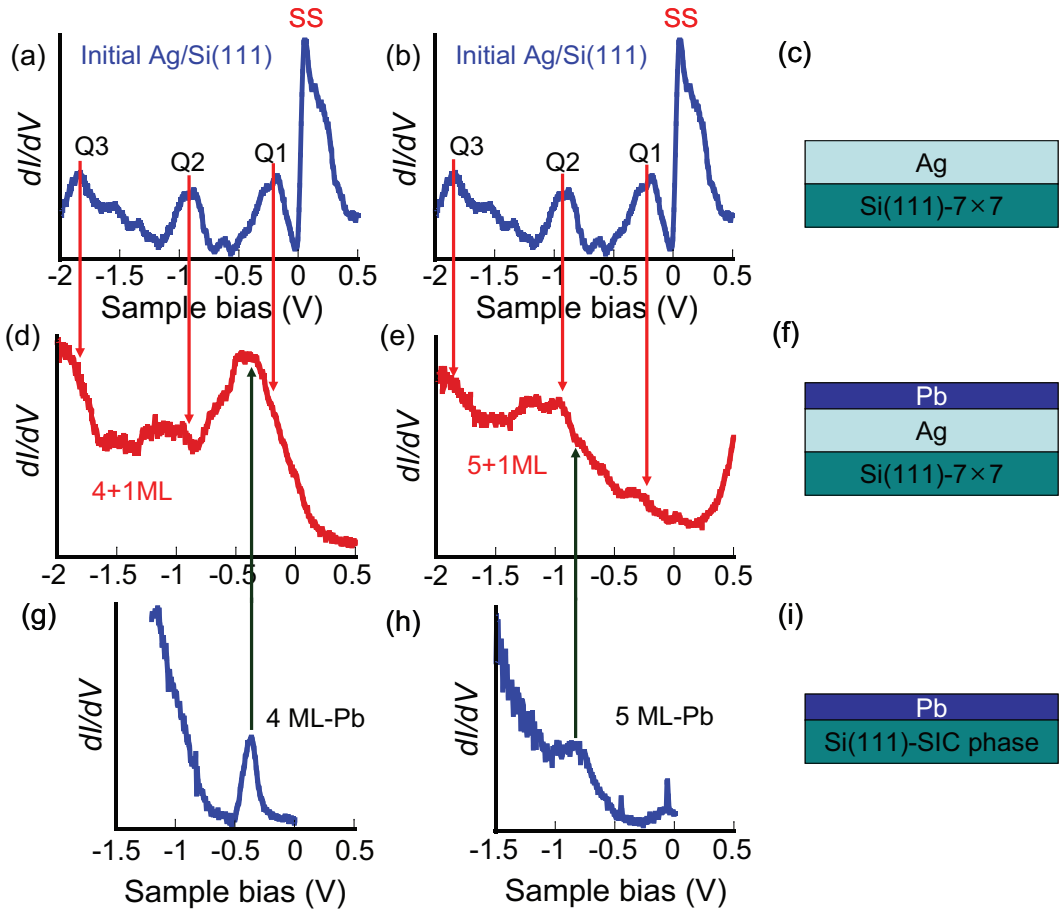

Figure 6.13: (a – b) Initial Ag film′s spectrum showing the surface state and 3 QWS. (d – e) Spectra taken on Pb overlayer grown on Ag/Si(111): (d) 5 ML Pb overlayer and (e) 6 ML Pb overlayer. (g – h) Reference spectra taken on 4 ML and 5 ML Pb films grown on SIC phase prepared on Si(111). For the correct comparison, 1 ML (wetting layer) addition to these Pb thicknesses is required. (c,f,i) Schematics corresponding to each system.

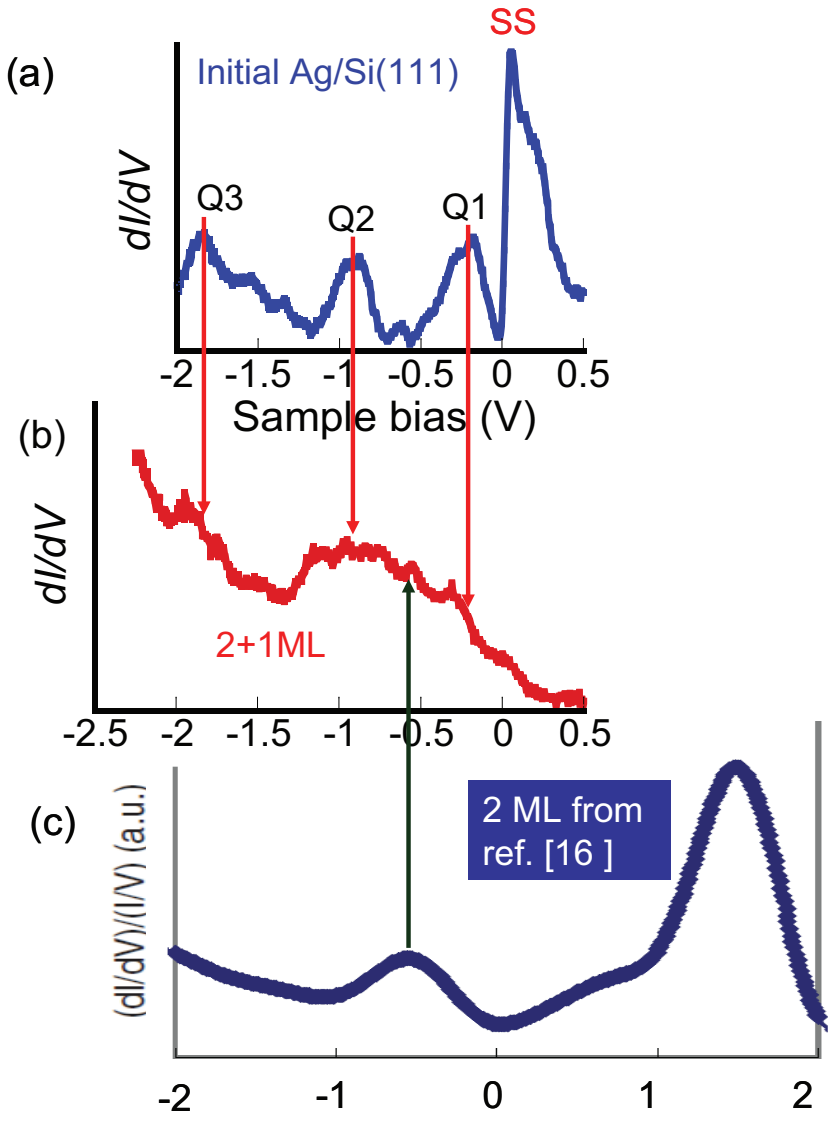

Figure 6.14: (a) Initial Ag film's spectrum showing the surface state and 3 QWS. (b) Spectrum taken on Pb overlayer (3 ML) grown on Ag/Si(111). (c) Reference spectrum for 2 ML Pb films grown on a mixture of $\sqrt{3} \times \sqrt{3}$ and $\sqrt{7} \times \sqrt{3}$ phases prepared on Si(111) [16].

Bibliography

[1] G. Binnig and H. Rohrer. Scanning tunneling microscopy. *Helvetica Physica Acta*, 55(6):726–735, 1982.

[2] G. Binnig, H. Rohrer, C. Gerber, and E. Weibel. Tunneling through a controllable vacuum gap. *Applied Physics Letters*, 40(2):178–180, 1982.

[3] G. Binnig, H. Rohrer, C. Gerber, and E. Weibel. Surface studies by scanning tunneling microscopy. *Physical Review Letters*, 49(1):57–61, 1982.

[4] J. Bardeen. Tunnelling from a many-particle point of view. *Physical Review Letters*, 6(2):57–59, 1961.

[5] L. D. Landau and E. M. Lifshitz. *Quantum Mechanics*. Pergamon Press, Oxford, third edition edition, 1977.

[6] Shuheng Pan. Piezoelectric motor (patent number: Wo 93/19494, international bureau, world intellectual property organization), September 1993.

[7] SH Pan, EW Hudson, and JC Davis. He-3 refrigerator based very low temperature scanning tunneling microscope. *Review of Scientific Instruments*, 70(2):1459–1463, 1999.

[8] A. R. Smith, K. J. Chao, Q. Niu, and C. K. Shih. Formation of atomically flat silver films on gaas with a "silver mean" quasi periodicity. *Science*, 273(5272):226–228, 1996.

[9] Z. Y. Zhang, Q. Niu, and C. K. Shih. "electronic growth" of metallic overlayers on semiconductor substrates. *Physical Review Letters*, 80(24):5381–5384, 1998.

[10] Peter J. Feibelman. Static quantum-size effects in thin crystalline, simple-metal films. *Physical Review B*, 27(4):1991–1996, 1983.

[11] C. M. Wei and M. Y. Chou. Theory of quantum size effects in thin pb(111) films. *Physical Review B*, 66(23):233408, 2002.

[12] W. B. Su, S. H. Chang, W. B. Jian, C. S. Chang, L. J. Chen, and T. T. Tsong. Correlation between quantized electronic states and oscillatory thickness relaxations of 2d pb islands on si(111)-(7 x 7) surfaces. *Physical Review Letters*, 86(22):5116–5119, 2001.

[13] X. C. Ma, P. Jiang, Y. Qi, J. F. Jia, Y. Yang, W. H. Duan, W. X. Li, X. Bao, S. B. Zhang, and Q. K. Xue. Experimental observation of quantum oscillation of surface chemical reactivities. *Proceedings of the National Academy of Sciences of the United States of America*, 104(22):9204–9208, 2007.

[14] Y Guo, YF Zhang, XY Bao, TZ Han, Z Tang, LX Zhang, WG Zhu, EG Wang, Q Niu, ZQ Qiu, JF Jia, ZX Zhao, and QK Xue. Superconduc-

tivity modulated by quantum size effects. *Science*, 306(5703):1915–1917, 2004.

[15] Daejin Eom, S. Qin, M.-Y. Chou, and C. K. Shih. Persistent superconductivity in ultrathin pb films: A scanning tunneling spectroscopy study. *Physical Review Letters*, 96(2):027005, 2006.

[16] S. Y. Qin, J. Kim, Q. Niu, and C. K. Shih. Superconductivity at the two-dimensional limit. *Science*, 324(5932):1314–1317, 2009.

[17] P. Czoschke, H. W. Hong, L. Basile, and T. C. Chiang. Quantum beating patterns observed in the energetics of pb film nanostructures. *Physical Review Letters*, 93(3):036103, 2004.

[18] P. S. Kirchmann, M. Wolf, J. H. Dil, K. Horn, and U. Bovensiepen. Quantum size effects in pb/si(111) investigated by laser-induced photoemission. *Physical Review B*, 76(7):075406, 2007.

[19] J. Kim, S. Y. Qin, W. Yao, Q. Niu, M. Y. Chou, and C. K. Shih. Quantum size effects on the work function of metallic thin film nanostructures. *Proceedings of the National Academy of Sciences of the United States of America*, 107(29):12761–12765, 2010.

[20] CS Jiang, HB Yu, CK Shih, and P Ebert. Effect of the si substrate structure on the growth of two-dimensional thin ag films. *Surface Science*, 518(1-2):63–71, 2002.

[21] H Liu, YF Zhang, DY Wang, MH Pan, JF Jia, and QK Xue. Two-dimensional growth of al films on si(111)-7 x 7 at low-temperature. *Surface Science*, 571(1-3):5–11, 2004.

[22] M. M. Ozer, Y. Jia, B. Wu, Z. Y. Zhang, and H. H. Weitering. Quantum stability and reentrant bilayer-by-bilayer growth of atomically smooth pb films on semiconductor substrates. *Physical Review B*, 72(11):113409, 2005.

[23] Takashi Uchihashi, Tomonobu Nakayama, and Masakazu Aono. Substrate dependent low-temperature growth of thin ag films: Study on si(111) - in surfaces. *Japanese Journal of Applied Physics Part 1-Regular Papers Brief Communications & Review Papers*, 46(9A):5975–5980, 2007.

[24] L. Seehofer, G. Falkenberg, D. Daboul, and R. L. Johnson. Structural study of the close-packed two-dimensional phases of pb on ge(111) and si(111). *Physical Review B*, 51(19):13503–13515, 1995.

[25] Kotaro Horikoshi, Xiao Tong, Tadaaki Nagao, and Shuji Hasegawa. Structural phase transitions of pb-adsorbed si(111) surfaces at low temperatures. *Physical Review B*, 60(19):13287–13290, 1999.

[26] M. Hupalo, J. Schmalian, and M. C. Tringides. "devil's staircase" in pb/si(111) ordered phases. *Physical Review Letters*, 90(21):216106, 2003.

[27] C. S. Jiang, S. C. Li, H. B. Yu, D. Eom, X. D. Wang, P. Ebert, J. F. Jia, Q. K. Xue, and C. K. Shih. Building pb nanomesas with atomic-layer

precision. *Physical Review Letters*, 92(10):106104, 2004.

[28] I. B. Altfeder, D. M. Chen, and K. A. Matveev. Imaging buried interfacial lattices with quantized electrons. *Physical Review Letters*, 80(22):4895–4898, 1998.

[29] Y. Jia, B. Wu, H. H. Weitering, and Z. Y. Zhang. Quantum size effects in pb films from first principles: The role of the substrate. *Physical Review B*, 74(3):035433, 2006.

[30] T. Miller, M. Y. Chou, and T. C. Chiang. Phase relations associated with one-dimensional shell effects in thin metal films. *Physical Review Letters*, 102(23):236803, 2009.

[31] D. A. Luh, T. Miller, J. J. Paggel, M. Y. Chou, and T. C. Chiang. Quantum electronic stability of atomically uniform films. *Science*, 292(5519):1131–1133, 2001.

[32] J. J. Paggel, C. M. Wei, M. Y. Chou, D. A. Luh, T. Miller, and T. C. Chiang. Atomic-layer-resolved quantum oscillations in the work function: Theory and experiment for ag/fe(100). *Physical Review B*, 66(23):233403, 2002.

[33] C. M. Wei and M. Y. Chou. Effects of the substrate on quantum well states: A first-principles study for ag/fe(100). *Physical Review B*, 68(12):125406, 2003.

[34] I. Horcas, R. Fernandez, J. M. Gomez-Rodriguez, J. Colchero, J. Gomez-Herrero, and A. M. Baro. Wsxm: A software for scanning probe microscopy and a tool for nanotechnology. *Review of Scientific Instruments*, 78(1):013705, 2007.

[35] M. Hupalo, V. Yeh, L. Berbil-Bautista, S. Kremmer, E. Abram, and M. C. Tringides. Uniform-height island growth of pb on si(111)-pb(root 3x root 3) at low temperatures. *Physical Review B*, 6415(15):155307, 2001.

[36] M. Hupalo and M. C. Tringides. Correlation between height selection and electronic structure of the uniform height pb/si(111) islands. *Physical Review B*, 65(11):115406, 2002.

[37] S. H. Chang, W. B. Su, W. B. Jian, C. S. Chang, L. J. Chen, and T. T. Tsong. Electronic growth of pb islands on si(111) at low temperature. *Physical Review B*, 65(24):245401, 2002.

[38] P. Czoschke, H. Hong, L. Basile, and T. C. Chiang. Quantum size effects in the surface energy of pb/si(111) film nanostructures studied by surface x-ray diffraction and model calculations. *Physical Review B*, 72(7):075402, 2005.

[39] T. A. Witten and L. M. Sander. Diffusion-limited aggregation, a kinetic critical phenomenon. *Physical Review Letters*, 47(19):1400–1403, 1981.

[40] S. M. Binz, M. Hupalo, and M. C. Tringides. Height-dependent nucleation and ideal layer by layer growth in pb/pb(111)/si(111). *Physical*

Review B, 78(19):193407, 2008.

[41] Y. Jia, B. A. Wu, C. Li, T. L. Einstein, H. H. Weitering, and Z. Y. Zhang. Strong quantum size effects in pb(111) thin films mediated by anomalous friedel oscillations. *Physical Review Letters*, 105(6):066101, 2010.

[42] M. H. Upton, T. Miller, and T. C. Chiang. Unusual band dispersion in pb films on si(111). *Physical Review B*, 71(3):033403, 2005.

[43] J. H. Dil, J. W. Kim, T. Kampen, K. Horn, and A. R. H. F. Ettema. Electron localization in metallic quantum wells: Pb versus in on si(111). *Physical Review B*, 73(16):161308(R), 2006.

[44] C. T. Campbell, S. C. Parker, and D. E. Starr. The effect of size-dependent nanoparticle energetics on catalyst sintering. *Science*, 298(5594):811–814, 2002.

[45] G. Mills, M. S. Gordon, and H. Metiu. Oxygen adsorption on au clusters and a rough au(111) surface: The role of surface flatness, electron confinement, excess electrons, and band gap. *Journal of Chemical Physics*, 118(9):4198–4205, 2003.

[46] M. Valden, X. Lai, and D. W. Goodman. Onset of catalytic activity of gold clusters on titania with the appearance of nonmetallic properties. *Science*, 281(5383):1647–1650, 1998.

[47] B. Yoon, H. Hakkinen, U. Landman, A. S. Worz, J. M. Antonietti, S. Abbet, K. Judai, and U. Heiz. Charging effects on bonding and catalyzed

oxidation of co on au-8 clusters on mgo. *Science*, 307(5708):403–407, 2005.

[48] H. J. Freund. Model systems in heterogeneous catalysis: Selectivity studies at the atomic level. *Topics in Catalysis*, 48(1-4):137–144, 2008.

[49] M. S. Chen and D. W. Goodman. The structure of catalytically active gold on titania. *Science*, 306(5694):252–255, 2004.

[50] M. S. Chen, D. Kumar, C. W. Yi, and D. W. Goodman. The promotional effect of gold in catalysis by palladium-gold. *Science*, 310(5746):291–293, 2005.

[51] J. Greeley, T. F. Jaramillo, J. Bonde, I. B. Chorkendorff, and J. K. Norskov. Computational high-throughput screening of electrocatalytic materials for hydrogen evolution. *Nature Materials*, 5(11):909–913, 2006.

[52] F. Studt, F. Abild-Pedersen, T. Bligaard, R. Z. Sorensen, C. H. Christensen, and J. K. Norskov. Identification of non-precious metal alloy catalysts for selective hydrogenation of acetylene. *Science*, 320(5881):1320–1322, 2008.

[53] F. Besenbacher, I. Chorkendorff, B. S. Clausen, B. Hammer, A. M. Molenbroek, J. K. Norskov, and I. Stensgaard. Design of a surface alloy catalyst for steam reforming. *Science*, 279(5358):1913–1915, 1998.

[54] L. P. Nielsen, F. Besenbacher, I. Stensgaard, E. Laegsgaard, C. Engdahl, P. Stoltze, K. W. Jacobsen, and J. K. Norskov. Initial growth of au on

ni(110) - surface alloying of immiscible metals. *Physical Review Letters*, 71(5):754–757, 1993.

[55] U. Bardi. The atomic-structure of alloy surfaces and surface alloys. *Reports on Progress in Physics*, 57(10):939–987, 1994.

[56] C. T. Campbell. Bimetallic surface-chemistry. *Annual Review of Physical Chemistry*, 41:775–837, 1990.

[57] J. A. Rodriguez. Physical and chemical properties of bimetallic surfaces. *Surface Science Reports*, 24(7-8):225–287, 1996.

[58] V. Ponec. Catalysis by alloys in hydrocarbon reactions. *Advances in Catalysis*, 32:149–214, 1983.

[59] John H. Sinfelt. *Bimetallic Catalysts : Discoveries, Concepts, and Applications*. Wiley, New York, 1983.

[60] A. A. Khajetoorians, W. G. Zhu, J. Kim, S. Y. Qin, H. Eisele, Z. Y. Zhang, and C. K. Shih. Adsorbate-induced restructuring of pb mesas grown on vicinal si(111) in the quantum regime. *Physical Review B*, 80(24):245426, 2009.

[61] G. Kresse and J. Furthmuller. Efficient iterative schemes for ab initio total-energy calculations using a plane-wave basis set. *Physical Review B*, 54(16):11169–11186, 1996.

[62] P. E. Blochl. Projector augmented-wave method. *Physical Review B*, 50(24):17953–17979, 1994.

[63] G. Kresse and D. Joubert. From ultrasoft pseudopotentials to the projector augmented-wave method. *Physical Review B*, 59(3):1758–1775, 1999.

[64] B. Hammer, L. B. Hansen, and J. K. Norskov. Improved adsorption energetics within density-functional theory using revised perdew-burke-ernzerhof functionals. *Physical Review B*, 59(11):7413–7421, 1999.

[65] R. W. G. Wyckoff. *Crystal Structures*. Wiley-Interscience, New York, 1965.

[66] M. Methfessel and A. T. Paxton. High-precision sampling for brillouin-zone integration in metals. *Physical Review B*, 40(6):3616–3621, 1989.

[67] G. Henkelman, B. P. Uberuaga, and H. Jonsson. A climbing image nudged elastic band method for finding saddle points and minimum energy paths. *Journal of Chemical Physics*, 113(22):9901–9904, 2000.

[68] Y. F. Zhang, J. F. Jia, T. Z. Han, Z. Tang, Q. T. Shen, Y. Guo, Z. Q. Qiu, and Q. K. Xue. Band structure and oscillatory electron-phonon coupling of pb thin films determined by atomic-layer-resolved quantum-well states. *Physical Review Letters*, 95(9):096802, 2005.

[69] Y. Yang, J. Li, Z. R. Liu, G. Zhou, J. Wu, W. H. Duan, P. Jiang, J. F. Jia, Q. K. Xue, B. L. Gu, and S. B. Zhang. Activated dissociation of o-2

on pb(111) surfaces by pb adatoms. *Physical Review B*, 80(7):073406, 2009.

[70] K. Reuter and M. Scheffler. Composition, structure, and stability of ruo2(110) as a function of oxygen pressure. *Physical Review B*, 65(3):035406, 2002.

[71] K. Thurmer, E. Williams, and J. Reutt-Robey. Autocatalytic oxidation of lead crystallite surfaces. *Science*, 297(5589):2033–2035, 2002.

[72] A. A. Khajetoorians, G. A. Fiete, and C. K. Shih. Visualizing quantum well state perturbations of metallic thin films near stacking fault defects. *Physical Review B*, 81(4):041413, 2010.

[73] S. Å. Lindgren and L. Walldén. Discrete valence-electron states in thin metal overlayers on a metal. *Physical Review Letters*, 59(26):3003–3006, 1987.

[74] J. J. Paggel, T. Miller, and T.-C. Chiang. Quasiparticle lifetime in macroscopically uniform ag/fe(100) quantum wells. *Physcal Rivew Letters*, 81(25):5632–5635, 1998.

[75] RK Kawakami, E Rotenberg, HJ Choi, EJ Escorcia-Aparicio, MO Bowen, JH Wolfe, E Arenholz, ZD Zhang, NV Smith, and ZQ Qiu. Quantum-well states in copper thin films. *Nature*, 398(6723):132–134, 1999.

[76] Roberto Otero, Amadeo L. Vázquez de Parga, and Rodolfo Miranda. Observation of preferred heights in pb nanoislands: A quantum size effect. *Physical Review B*, 66(11):115401, 2002.

[77] D. Wegner, A. Bauer, and G. Kaindl. Electronic structure and dynamics of quantum-well states in thin yb metal films. *Physical Review Letters*, 94(12):126804, 2005.

[78] M. C. Yang, C. L. Lin, W. B. Su, S. P. Lin, S. M. Lu, H. Y. Lin, C. S. Chang, W. K. Hsu, and Tien T. Tsong. Phase contribution of image potential on empty quantum well states in pb islands on the cu(111) surface. *Physical Review Letters*, 102(19):196102, 2009.

[79] M. Becker and R. Berndt. Scattering and lifetime broadening of quantum well states in pb films on ag(111). *Physical Review B*, 81(20):205438, 2010.

[80] M. K. Brinkley, Y. Liu, N. J. Speer, T. Miller, and T. C. Chiang. Using electronic coherence to probe a deeply embedded quantum well in bimetallic pb/ag films on si(111). *Physical Review Letters*, 103(24):246801, 2009.

[81] Z. Y. Zhang and M. G. Lagally. Atomistic processes in the early stages of thin-film growth. *Science*, 276(5311):377–383, 1997.

[82] L. Huang, S. J. Chey, and J. H. Weaver. Metastable structures and critical thicknesses: Ag on si(111)-7x7. *Surface Science*, 416(1-2):L1101–L1106, 1998.

[83] P. O. Gartland and B. J. Slagsvold. Transitions conserving parallel momentum in photoemission from the (111) face of copper. *Physical Review B*, 12(10):4047–4058, 1975.

[84] F. Reinert, G. Nicolay, S. Schmidt, D. Ehm, and S. Hufner. Direct measurements of the l-gap surface states on the (111) face of noble metals by photoelectron spectroscopy. *Physical Review B*, 63(11):115415, 2001.

[85] G. Neuhold and K. Horn. Depopulation of the ag(111) surface state assigned to strain in epitaxial films. *Physical Review Letters*, 78(7):1327–1330, 1997.

[86] M. F. Crommie, C. P. Lutz, and D. M. Eigler. Imaging standing waves in a two-dimensional electron gas. *Nature*, 363:524–527, 1993.